EXOMOON HABITABILITY AND TIDAL EVOLUTION IN LOW-MASS STAR SYSTEMS

by

Rhett R. Zollinger

A dissertation submitted to the faculty of
The University of Utah
in partial fulfillment of the requirements for the degree of

Doctor of Philosophy

in

Physics

Department of Physics and Astronomy

The University of Utah

December 2014

The University of Utah Graduate School

STATEMENT OF DISSERTATION APPROVAL

The dissertation of **Rhett R. Zollinger**

has been approved by the following supervisory committee members:

Benjamin C. Bromley	, Chair	**07/08/2014** Date Approved
John C. Armstrong	, Member	**07/08/2014** Date Approved
Bonnie K. Baxter	, Member	**07/08/2014** Date Approved
Jordan M. Gerton	, Member	**07/08/2014** Date Approved
Anil C. Seth	, Member	**07/08/2014** Date Approved

and by **Carleton DeTar**, Chair/Dean of

the Department/College/School of **Physics and Astronomy**

and by David B. Kieda, Dean of The Graduate School.

ABSTRACT

Current technology and theoretical methods are allowing for the detection of sub-Earth sized extrasolar planets. In addition, the detection of massive moons orbiting extrasolar planets ("exomoons") has become feasible and searches are currently underway. Several extrasolar planets have now been discovered in the habitable zone (HZ) of their parent star. This naturally leads to questions about the habitability of moons around planets in the HZ.

Red dwarf stars present interesting targets for habitable planet detection. Compared to the Sun, red dwarfs are smaller, fainter, lower mass, and much more numerous. Due to their low luminosities, the HZ is much closer to the star than for Sun-like stars. For a planet-moon binary in the HZ, the close proximity of the star presents dynamical restrictions on the stability of the moon, forcing it to orbit close to the planet to remain gravitationally bound. Under these conditions the effects of tidal heating, distortion torques, and stellar perturbations become important considerations to the habitability of an exomoon.

Utilizing an evolution model that considers both dynamical and tidal interactions, I performed a computational investigation into long-term evolution of exomoon systems. My study focused on satellite systems in the HZ of red dwarf stars and the dependence of exomoon habitability on the mass of the central star. Results show that dwarf stars with masses $\lesssim 0.2\ M_{\odot}$ cannot host habitable exomoons within the stellar HZ due to extreme tidal heating in the moon. These results suggest that a host planet could be located outside the stellar HZ to where higher tidal heating rates could act to promote habitability for an otherwise uninhabitable moon. Perturbations from a central star may continue to have deleterious effects in the HZ up to $\approx 0.5\ M_{Sun}$, depending on the host planet's mass and its location in the HZ. In cases with lower intensity tidal heating, stellar perturbations may have a positive influence on exomoon habitability by promoting long-term heating rates above a minimum for habitable terrestrial environments. In addition to heating concerns, torques due to tidal and spin distortion can lead to the relatively rapid inward spiraling of a moon. The effects of torque and stability constraints also make it unlikely that long-term resonances between two massive moons will develop in the HZs around red dwarf stars.

My study showed that moons in the circumstellar HZ are not necessarily habitable

by definition. In addition, the HZ for an exomoon may extend beyond the HZ for an exoplanet. Therefore, an extended model is required when considering exomoon habitability in comparison to exoplanet habitability.

To Stefanie, Missy, Bella, and Conner — if I've learned one thing from this experience it's that your support is worth more than any success.

CONTENTS

LIST OF FIGURES

LIST OF TABLES

ACKNOWLEDGMENTS

I would first like to thank John Armstrong for nearly a decade of encouragement and support. I originally met John as an undeclared undergraduate student taking my first-ever physics course (PHYS 1010). If at that time I had not randomly picked his class to fulfill a general requirement, I would simply not be writing this dissertation today. His guidance has been invaluable and I immensely appreciate the many hours he has volunteered to the completion of this particular project.

I express my sincere appreciation to Ben Bromley for agreeing to sponsor me in this work. Ben helped me find my way as a graduate student and his direction made this study a success. I also thank the faculty and staff in the Department of Physics and Astronomy at the University of Utah, as well as the Telescope Array group. While my dissertation work did not directly involve cosmic rays, my experiences with their group are irreplaceable.

I offer special thanks to René Heller for his contribution to this study, specifically, for our many conversations and for his incredibly valuable suggestions. His impressive work concerning exomoons has in many ways inspired this dissertation.

I want to thank the Utah Space Grant Consortium and recognize their support, which gave me the time needed to explore this research. I am also indebted to the Department of Physics at Weber State University for multiple reasons: first, for providing the best undergraduate experience in physics that I can imagine; second, for providing me the opportunity to explore my passion for teaching during my graduate studies; finally, for the generous and unlimited access to their high-performance computing cluster. I cannot imagine doing this research without it. This research has also made use of the Exoplanet Orbit Database and the Exoplanet Data Explorer at exoplanets.org.

I need to thank my mother and father, and not just for the obvious reasons. My father, Ronald Zollinger, volunteered many hours to the editing and proofreading of this document. Beyond that, I am who I am today because of my parent's love and immeasurable support.

In the last, most important place, I thank my wife, Stefanie. There were dark times as a graduate student, but she never let me give up. Words can simply not express my gratitude for her.

CHAPTER 1

INTRODUCTION

Long ago, watchers of the night sky noticed that certain stars did not appear in the same part of the sky each night. The ancients called them the *asteres planetai*, or the "wandering stars." It was the irregular *motions* of the wandering stars that eventually distinguished them as planets. Today, as we also turn our gaze toward the vast ocean of space and time, we continue to wonder as to the existence of other worlds similar to our own. Extrasolar planets, or "exoplanets," are planets that orbit stars other than our sun. It is no exaggeration to say that a significant amount of motivation in the search for extrasolar planets is embodied in the age-old question: "Are we alone?."

Earth is currently the only environment where life is known to reside. Searches for extrasolar life would naturally begin with environments similar to this sole example. Planets are considered to offer the best locations for life to begin. With this in mind, this study will start with an overview of the work currently being performed in the field of extrasolar planetary science. In our Solar System, the exploration of the moons of Jupiter and Saturn has also reaped immense understanding of otherworldly environments. For this reason, the primary motivation for this dissertation is an investigation into objects other than planets which may also provide environments suitable for life to begin. By this I refer to the moon's of large exoplanets, or "exomoons."

1.1 Exoplanet Detection Methods

The first definitive exoplanet detection is credited to Wolszczan and Frail (1992),[1] which involved a pulsar as the parent star. As planetary hosts, pulsars undoubtedly provide hellish environments due to their intense radiation. So it can be assumed that orbiting planets would not harbor life. Nevertheless, the first confirmed exoplanet detection was a major accomplishment that spurred on the exoplanet hunt towards the real prize of finding a planet

[1]Previous claims for detection had been made, but none were satisfactorily confirmed until after the announcement by Wolszczan and Frail (1992).

around a Sun-like star. Since this discovery, exoplanet searches have enjoyed significant success thanks to continual advancements in detection instrumentation and theory. In this section, only a brief introduction to modern detection techniques will be provided.

1.1.1 Historical Perspective

It was not until 1609 that the first incontrovertible evidence was provided for celestial bodies orbiting something other than Earth. This achievement was made by Galileo Galilei when he used his newly designed telescope to observe the four largest moons of Jupiter. It was Galileo's telescope design that paved the way for the first significant planetary discovery in centuries, the discovery of Uranus in 1781 (Herschel). In this detection and in all prior detections, the method utilized was the classical method of directly observing the reflected starlight from planets and moons.

The transition between the classical method and methods later used to detected extrasolar planets in many ways began with the discovery of Neptune. Bouvard (1821) was the first to hypothesize Neptune's existence when he noticed substantial deviations from predictions in the tabulated observations of the orbit of Uranus. The explanation he provided was that Uranus was being perturbed by an unknown outer planet. His idea was further advanced by Le Verrier (1845) and Adams (1846) when they calculated what the orbit of the perturbing body must be. Following their predictions, the detection was made soon after by Galle (1846). Neptune, then, represented a transitional stage between the classic technique to an indirect technique for detecting bodies based on the predictions of celestial mechanics. The practice of using an advanced understanding of celestial mechanics for detecting planets would later play a vital role in extrasolar planetary searches.

The planetary picture of our Solar System became apparently complete with the detection of Pluto[2] in 1930 by Clyde Tombaugh. After that, many astronomers set their sights on more distant planets - those orbiting stars other than our Sun. One complication to this new challenge was that the light reflected from extrasolar planets is typically one million to one billion times fainter than the reflected starlight of solar system planets. To make matters worse, the light is extremely challenging to spatially resolve from the host star. Needless to say, when astronomers began the ambitious goal of detecting exoplanets, they understood that it would not be achievable through conventional techniques and that new indirect methods would need to be developed.

---

[2]Pluto has since been reclassified as a "dwarf planet."

1.1.2 Radial Velocity

Taking a lesson from basic classical mechanics, the motion of a single planet in orbit around a star causes the star to undergo a reflex motion about the star-planet barycenter (see Figure 1.1). This motion leads to variations in the line-of-sight (radial) component of the star's velocity in which the star moves towards and away from an external observer. Utilizing this motion, the radial velocity (RV) detection method measures the line-of-sight velocity of a star in order to indirectly test for the presence of a planet. Measuring the radial component of a star's velocity can be achieved by measuring Doppler shifts in the star's spectral lines. This requires a very stable spectrograph with highly sensitive calibration and a rich forest of lines to measure.

For a two-body star/planet system in an inertial frame, the planetary motion must balance with the stellar motion about the system's center of mass. Because there is typically a large difference in mass between any star and planet, the star's orbit is much smaller than the planet's (i.e. the star's velocity will also be much slower). However, the more massive a planet is and the closer it orbits the star, the faster the resulting stellar motion will be. For this reason, the RV method is more sensitive to higher mass, shorter period planets. Consequently, the method presents a detection bias for these conditions. This bias has decreased in recent years as the result of modern technological advancements and refinements in procedures used for data analysis. For example, early RV surveys had sensitivities no less than 10 m/s. By the mid-1990s, this had increased to some 3-5 m/s (Butler et al. 1996). Today, RV surveys can detect velocity variations down to around 0.3-0.5 m/s (Pepe and Lovis 2008).

The fact that the RV method is sensitive to the shape and orientation of a planet's orbit serves as both advantage and disadvantage. The advantage is that the eccentricity, the period, and the argument of periastron of the orbit can be measured directly. The disadvantage is that highly inclined orbits to the line of sight from Earth produce smaller steller "wobbles" and are thus more difficult to detect. In addition, this method can only estimate a planet's minimum mass (M_{true} x sin$i$), where i is the inclination of the orbit. Hence, a planet's true mass cannot be determined unless the inclination of the planet's orbit is also found. Fortunately, there are ways around this obstacle. RV measurements can be used in combination with the transit method (see subsection 1.1.3) to determine the true mass of the planet.

The first detection of an extrasolar planet using the RV method was also the first for a planet orbiting a Sun-like star (Mayor and Queloz 1995). At that time, a Swiss group based

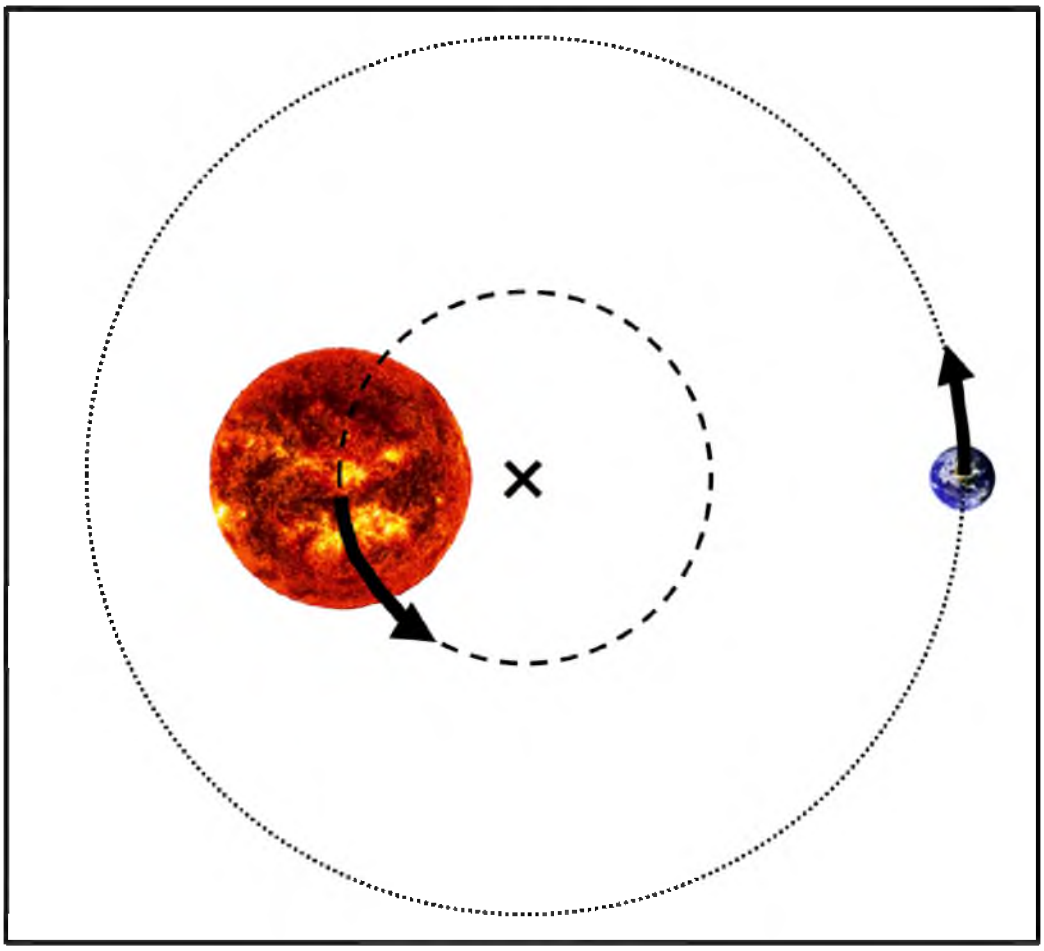

Figure 1.1. Cartoon illustrating the (exaggerated) reflex motion of a star in the inertial frame of the barycenter. The presence of the planet causes variations in the position (used for astrometry and pulsar timing) and the velocity (used for radial velocity) of the host star, which can be used to detect an exoplanet.

in Geneva was looking at 142 bright K and G dwarfs for radial velocity variations with a sensitivity of ~13m/s. Their discovery centered around "51 Peg," a bright G2- to G4-type star relatively close at 15.6pc in the Pegasus constellation. The planet 51 Peg b was found at 0.05 AU from the star with a period of 4.2 days and a minimum mass of 0.5 $M_{Jupiter}$. With this mass, the planet is most likely a gas giant.

1.1.3 Transiting Planets

While the RV method provides important information about a planet's orbit, it also provides frustratingly little information about their actual bodies. If the ultimate goal of exoplanet detection is to find signs of life, then the RV method fails to provide the necessary information. Fortunately, there are other promising options. If a planet detected by the RV method also happens to transit in front of its host star, relative to Earth, then additional information can be inferred about the planet's size, composition, atmosphere, temperature, and albedo.

The basic principle of the transit method is that the nominal flux (F) from a host star is temporarily attenuated due to a planet blocking out a fraction of the projected stellar surface. This occurs as the planet passes across its disk with the effect repeating at the orbital period of the planet. Light curves from transiting planets are of particular interest because they allow for estimates of their radius and orbital inclination. If this information can be combined with mass measurements from RV surveys, then the bulk density can be determined, leading to first estimates of their composition. Further probing of the planet's structure and atmospheric properties are accessible from photometry and spectroscopy during the transit and during the secondary eclipse when the planet passes behind the star[3] (Perryman 2011).

The geometric depth of the transit (ΔF) for a circular orbit is given by the ratio of the sky-projected area of the planet and the sky-projected area of the star:

$$\Delta F = \frac{\pi R_P^2}{\pi R_*^2} \tag{1.1}$$

For a planet with $R_P \sim R_{Jupiter}$ transiting a Sun-like star ($1R_\odot$), the drop in solar flux is $(\Delta F/F) \simeq 1.1\text{x}10^{-2}$, or about 1%. For an Earth-size planet transiting a Sun-like star, the change in brightness is only 84 parts per million, which is less than 1/100th of 1%. These examples illustrates the small effect being sought in this method. Ground-based surveys

[3]An eclipse is the (partial) obscuration of one celestial body by another. When of very different angular size, the term transit refers to the smaller (here the planet) moving in front of the larger (the star); an occultation, or secondary eclipse, refers to the planet passing behind the star.

will be limited by atmospheric seeing and scintillation, yet even modest current telescopes are capable of measuring transit depths up to about $(\Delta F/F) \simeq 1\%$, in large part due to the development of CCDs. Photometric precision in this range is sufficient to reveal the presence of gas-giants. Spaced-based surveys, however, avoid atmospheric effects and are currently discovering planets with transit depths of a few times 10^{-4}, thereby extending detectable exoplanet radii down to sub-Earth sizes. Given the obvious need for a fortuitous geometric alignment, the key question becomes, how likely is it that a transit will occur?

Assuming a nearly circular orbit, the probability for a randomly-oriented planet to be favorably aligned to transit, or secondary eclipse, is (Kane, Horner, and von Braun 2012)

$$P_t = \frac{R_P + R_*}{a} \ , \tag{1.2}$$

where a is the semimajor axis of the planet's orbit. Note that the transit probability is independent of the star's distance; however, increasing distance does cause a decrease in photometric accuracy. Equation (1.2) indicates that the probability of detection is greater for larger planets that orbit close to their host stars. If a transit is observed, the frequency of transit is also proportional to the orbital distance as $a^{-3/2}$. Thus, there is a natural bias for short orbits and large planets. Evaluation of inclination (i) and probability for realistic cases demonstrates that transits occur only for $i \simeq 90°$ and that the probability is small. To increase the probability of detection, modern projects utilize a wide-field survey in which they can monitor a large number of stars at any given time.

Charbonneau et al. (2000) and Henry et al. (2000) were the first to detect an exoplanet transit. The planet, HD 209458 b, is a Jupiter-mass planet orbiting close to its parent star. Charbonneau et al. (2000) observed two transits with a duration of 2.5 hrs and a transit depth of 1.5%. Their achievement is even more impressive knowing that it was done with the 4-inch STARE telescope, demonstrating the potential for inexpensive transit observations.

1.1.4 Direct Imaging

Direct imaging seeks to either spatially or spectrally resolve the light of the planet from that of the star. The light from the planet may be either reflected starlight (in the visible) or through its own thermal emission (in the infrared). Consequently, this method favors hot planets at wide separations.

One obvious challenge to this method is the overwhelming comparative brightness of the host star. For most systems, the planet/star flux ratio for reflected light will be very low. The challenge of actually resolving the light will exacerbate matters further. The star and

planet have an angular separation of a_P/d, where a_P is the planet's semimajor axis about the star and d is the distance to the star from the observer. Telescopes typically have their angular resolution constrained by the diffraction limit, given by $1.22\lambda/D$, where λ is the wavelength of the light and D is the diameter of the telescope. Therefore, direct imaging requires the use of large telescopes with short wavelengths to look around nearby stars with planets at wide separation. For ground-based telescopes, atmospheric effects provide additional complications. However, recent advancements in adaptive optics can be used to significantly lessen their impact.

The first image of an extrasolar planet is 2M1207b by Chauvin et al. (2004). The primary of this system is actually a brown dwarf, so the contrast ratio between the planet and "star" is quite favorable. Also, the planet orbits at ~50 AU and is hot, being in the range 1000-2000 K. Since that time, several additional planets have been directly imaged. Marois et al. (2010) were the first to directly image a system of planets. Their image is in the infrared and shows four hot planets orbiting at 14, 27, 42, and 67 AU. Such an image is possible because of the wide orbits and youth (<100Myr) of the planets which are still hot and bright as they radiate away gravitational energy acquired during their formation. The star, named HR 8799, is an A-type star. Such a high luminosity star would normally be less than favorable due to the low planet-to-star contrast. However, in this case, its higher mass allowed it to retain a more extended disk which is believed to have formed the widely separated massive planets.

1.1.5 Additional Detection Methods

In addition to the RV, transit, and direct imaging methods, other techniques have been proposed and have had success detecting exoplanets. However, their combined contribution to the total number of detected exoplanets is very low and they hold little interest to the study of exomoons. A few statements concerning the remaining detection methods will be provided in the interest of completeness.

1.1.5.1 Gravitational Microlensing

Gravitational microlensing draws upon the theory of general relativity in which matter (energy density) distorts spacetime and the path of electromagnetic radiation is deflected as a result. Put more simply, massive bodies bend the apparent path of light, which in essence, acts as a lens. Under the right conditions, if a star passes in front of a more distant and luminous background object (the source), the star (the lens) will cause the brightness of the background object to dramatically increase for a few days or weeks, depending on the

configuration. The same is true if the lensing star hosts a planet except that an observer will see two (or more) increases in brightness; one large increase due to the massive star and one smaller increase due to the planet. This method would naturally be more sensitive to massive planets with wide separations. One major downside is that microlensing events are inherently transient and after the event is over, there is no additional opportunity for follow-up.

1.1.5.2 Astrometry

Astrometry is complimentary to the theory behind the RV method in that it concerns the reflex motion of the host star as it orbits the system's center-of-mass (refer to Figure 1.1) . In this case, it is variations in the star's *position* that can betray the presence of an extrasolar planet (whereas the RV method measures variations in the star's velocity). In particular, this method aims to determine the transverse component of the displacement relative to the line-of-sight. The accuracy required to detect planets astrometrically is typically sub-mas (milli-arc-seconds) with most modern instrumentation only reaching accuracies around 1 mas. However, the recently launched "Gaia" spacecraft is expected to achieve accuracies of $\sim$20 - 25 μas (Perryman 2011).

1.1.5.3 Pulsar Timing

Similar to the discussion of RV and astrometry theory, if a pulsar has an orbiting planet, its reflex motion about the center-of-mass will cause periodic deviations in the times of arrival of the pulsar signal. Measurements of such timing deviations can provide an alternative route to the dynamical detection of orbiting planets. Interestingly, it is the pulsar timing method that is credited with the first unambiguous detection of an extrasolar planet (Wolszczan and Frail 1992).

1.2 Extrasolar Systems Overview

As mentioned in subsection 1.1.2, 51 Peg b was the first extrasolar planet detected around a Sun-like star, which is a roughly Jupiter mass planet with an orbital period of only a few days. The detection of such a large body that close to its host star was previously unanticipated. Planetary formation models of the Solar System (Pollack et al. 1996) suggest that gas giants formed beyond the frost-line. This line is the distance from a star where it is cold enough for hydrogen compounds to condense into solid ice grains, typically estimated to be about 150 K. For the 51 Peg system, this distance should be at least a few AU. While inward migration had been considered before the detection of 51 Peg b, inspections of the

Solar System gas giants alluded that this mechanism was not very effective. Consequently, this discovery presented a serious challenge to planet formation theories of the time and spurred new investigations into formation theory. Planets such as 51 Peg b have since been described as "hot-Jupiters" where hot-Jupiters are defined as planets with an orbital period less than 10 days and a minimum mass equal to about 0.5 $M_{Jupiter}$.

1.2.1 An Explosion of Discoveries

Just six days after the 51 Peg b discovery, Geoff Marcy and Paul Butler of San Francisco State University independently confirmed the signal, then shortly after achieved two new discoveries (Marcy and Butler 1996; Butler and Marcy 1996). So began the age of exoplanetary science with new discoveries being reported on an increasingly regular basis (see Figure 1.2).

Today, over a thousand exoplanets are known to exist[4] (Wright et al. 2011) and hundreds

[4]According to the exoplanet database at "exoplanets.org." I make use of this database throughout this document.

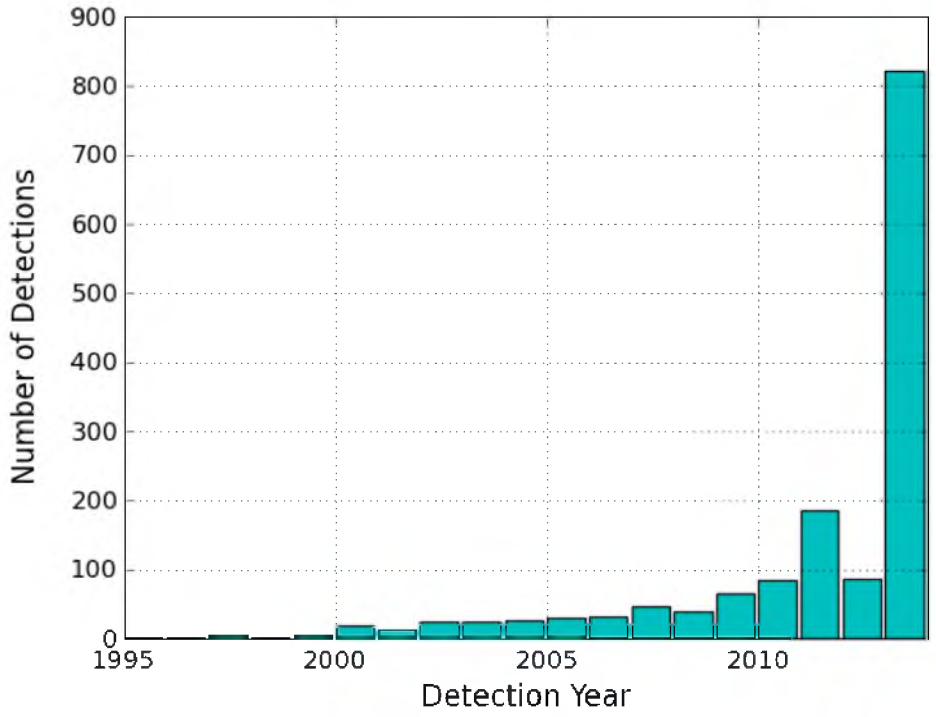

Figure 1.2. Exoplanet detections per year after 1995. The very recent spike is primarily due to a large release of Kepler candidate confirmations.

of these are found in multiplanet systems (two or more planets around a star). A detailed summary of the current number of confirmed detections is given in Table 1.1. Until the last couple of years, the large majority of detections resulted from RV surveys. However, that changed with the launch of NASA's Kepler space telescope in 2009 which utilized the transit method for planet detection. The Kepler spacecraft is essentially a photometer designed to continually monitor the brightness of over 145,000 main sequence stars in a fixed field of view (Borucki et al. 2008). Today, the combined efforts of RV and transit surveys have resulting in about 95% of all confirmed detections. In addition to the confirmed planets, there is another 3000+ unconfirmed Kepler "candidates" that await confirmation from additional observations or alternative detection techniques (other than transits).

1.2.2 Apparent Detection Bias

Extrasolar planets span a wide range of physical and orbital properties. Due to the bias of RV surveys to high mass, short-period planets, many initial detections included the previously unanticipated hot-Jupiters (Period $\lesssim$ 10 days, Mass $\gtrsim$ 0.5 $M_{Jupiter}$). However, with increasingly longer observational baselines and improvements to instrument precision, detections began to emerge for lower mass planets and for multiyear orbital period planets. More recent RV surveys have found that planet counts increase toward smaller masses, at least within the range of 1000 $M_\oplus$ down to $\sim 5 M_\oplus$ (Howard et al. 2010; Mayor et al. 2011), where $M_\oplus$ is the mass of the Earth. Also, technique improvements have lead to discoveries down to minimum masses $\simeq$ 1.1 $M_\oplus$ (Dumusque et al. 2012). An illustration of the relationship between mass and orbital distance for the detected exoplanets is shown in Figure 1.3, which shows that the majority of lowest-mass planets were detected only recently.

Table 1.1. Summary of confirmed exoplanet detections as of 06/22/2014. Source: exoplanets.org.

Total number of detections	**1518**
Planets *in* multiplanet systems	989
Systems with 2 planets	266
Systems with 3 planets	85
Systems with 4 planets	32
Systems with 5 planets	11
Systems with 6 planets	2
Systems with 7 planets	1

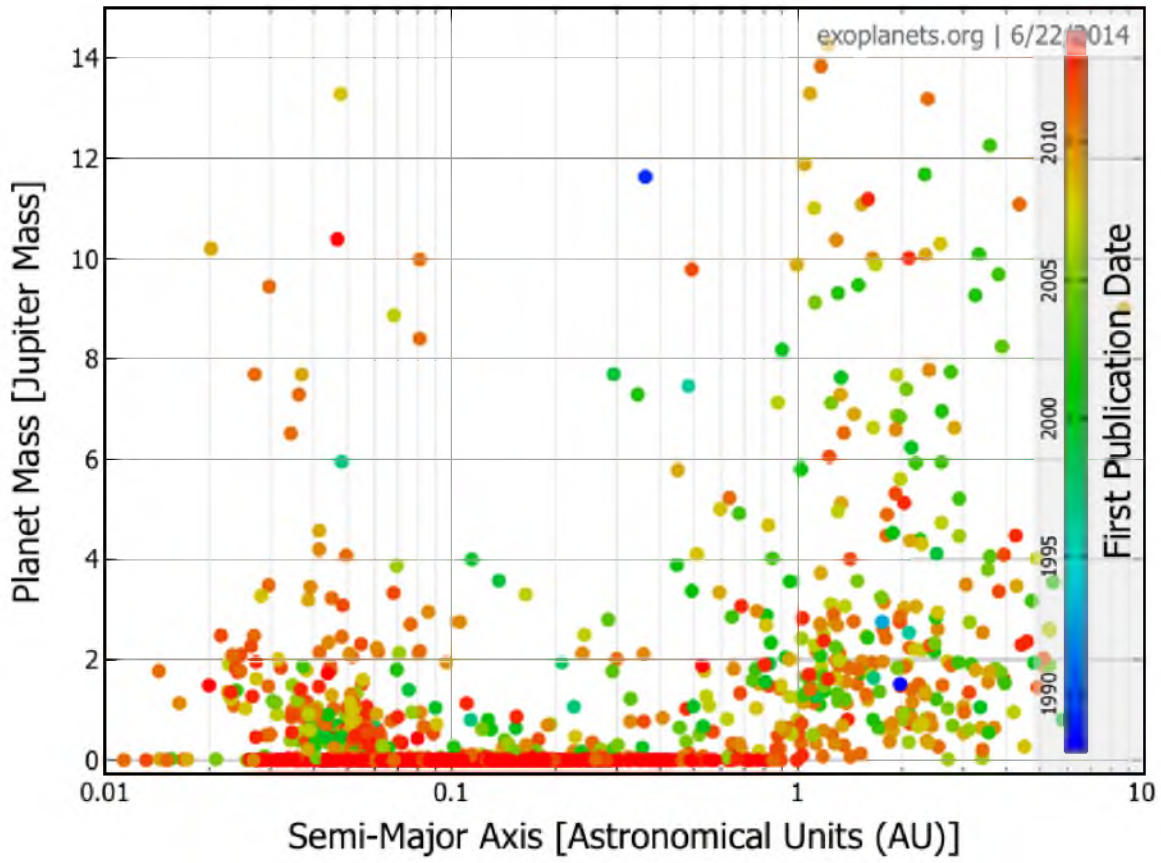

Figure 1.3. Relationship between mass and orbital distance (semimajor axis) for detected exoplanets. The colorscale indicates the detection date of the planet. Bluish-green colors represent the years when RV surveys dominated. Results from Kepler are included in the orange-red colors. The chosen axial limits result in the exclusion of a few higher mass or longer period planets. For comparison, 1 Earth mass = 0.0031 Jupiter masses. [Source: exoplanets.org]

Measurements of planetary radii received a major boost with the recent success of the Kepler program, in particular, measurements for Earth-sized planets. Kepler was specifically designed to search for Earth-like planets in or near the so called "habitable zone" (see subsection 1.3.1) of Sun-like stars. Today, Earth-like planet detections (in terms of size and mass) are becoming more common. The Kepler program independently found that 85% of its transiting planet "candidates" have radii less than 4 $R_{\oplus}$ (Batalha et al. 2013), and it is believed that more than 80% of these small candidates are actually planets (Morton and Johnson 2011; Fressin et al. 2013). For comparison, the radius of Neptune is 3.9 $R_{\oplus}$. Therefore, it seems that planets between the size of Earth and Neptune are common in our galaxy. It is worth pointing out that since the transit method favors close-in orbits, many of these detections are for short-period planets (<50 days). Consequently, a true

Earth analog has yet to be discovered. Still, these discoveries are impressive with the current record holder for smallest detection belongs to a Mercury-sized planet ($\sim$0.3 $R_\oplus$) (Batalha et al. 2013).

1.2.3 Exoplanet Composition

The first detection of a transiting planet was that of a now fairly typical hot-Jupiter (Charbonneau et al. 2000; Henry et al. 2000). However, that detection provided the first confirmation that Jupiter-mass planets in close orbits about their host stars have radii and densities comparable to the gas-giants of our own Solar System.

Interest in low-mass planets naturally stems from the separation between gas planets (higher mass) and rocky, terrestrial planets (lower mass). Traditionally, the accepted standard for the critical mass that separates rocky planets from gas planets was approximately 10 $M_\oplus$ (Valencia et al. 2006). However, this estimate was made during a time when very few radii were known for planets less than the mass of Jupiter (see Figure 1.4). Now that the sample size for planetary radii has significantly increased, the critical mass estimate is being reevaluated (see explanation below).

With so many new examples of planets in the range 1-4 $R_\oplus$, it is interesting to consider that we have no Solar System analogs for planets with 2-3 $R_\oplus$. This makes it difficult to understand their chemical compositions, interior structures, and formation processes; although, much discussion can be found in the literature (Fortney et al. 2007; Seager et al. 2007; Zeng and Seager 2008; Rogers et al. 2011; Lissauer et al. 2012; Fabrycky et al. 2012; Zeng and Sasselov 2013). Determining the chemical composition is one step toward a deeper understanding, but at this planet-size scale, the relative amounts of rock, water, and H and He gas remain poorly known. Most likely, the mixture of those three ingredients changes as a function of planet mass, but differs among planets at a given mass as well (Marcy et al. 2014).

One way to constrain the internal chemical composition for 1-4 $R_\oplus$ planets is to measure the masses (which can be done with RV or TTV measurements), and thus, determine a bulk density. However, the gravitational acceleration that these planets induce on their host star is small and therefore challenging to detect with current telescopes and instruments. As a result, only a comparative handful of small planets have mass measurements. Weiss and Marcy (2014) studied the masses and radii of 65 exoplanets smaller than 4 $R_\oplus$ with orbital periods shorter than 100 days.[5] They showed that on average, planets with radii up to

[5]Of the 65 exoplanets considered, only 19 have vetted mass values listed on exoplanets.org. The rest have

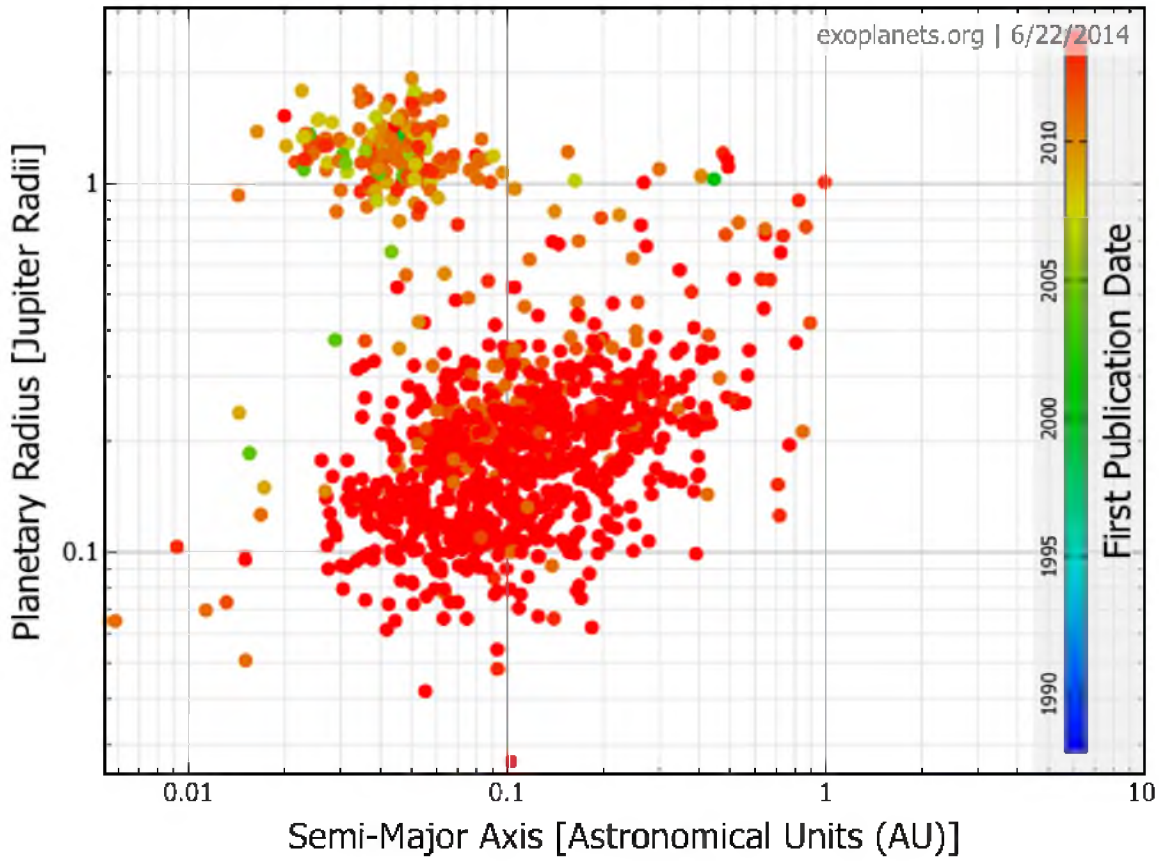

Figure 1.4. Relationship between planet radius and orbital distance (semimajor axis) for detected exoplanets. The colorscale indicates the detection date of the planet. Green colors represent a time when RV surveys dominated. Results from Kepler are included in the orange-red colors. From the coloring, it is obvious that the most radius measurements were made only recently. For comparison, 1 Earth radius = 0.089 Jupiter radii. [Source: exoplanets.org]

$R_P = 1.5R_\oplus$ increase in density with increasing radius. The densities in this range are consistent with rocky-type bodies with a maximum at 7.6 g cm^{-3} (Earth's density is 5.5 g cm^{-3}). However, above 1.5 $R_\oplus$, the average planet density rapidly decreases with increasing radius, indicating that these planets have a large fraction of volatiles by volume overlying a rocky core. Weiss and Marcy (2014) also derived an empirical density-radius relation and mass-radius relation for the range $R_P < 4R_\oplus$. Their results are summarized in Table 1.2. Other studies have suggested that planets with a radius between 1.4 and 2.0 $R_\oplus$ will have either homogeneous composition of water ice, silicates, and iron, or some differential composition of these compounds (Seager et al. 2007; Rogers et al. 2011; Lopez et al. 2012).

---

mass values that have not yet been added to the online database.

Table 1.2. Empirical Mass-Radius and Density-Radius Relations calculated by Marcy et al. (2014)

Planet Size	Equation
$R_P < 1.5 R_\oplus$	$\rho_P = 2.43 + 3.39 \left(\frac{R_P}{R_\oplus}\right) gcm^{-3}$
$1.5 \leq R_P/R_\oplus < 4$	$\frac{M_P}{M_\oplus} = 2.69 \left(\frac{R_P}{R_\oplus}\right)^{0.93}$

In addition to the study by Weiss and Marcy (2014), the authors took part in other similar empirical analyses (Weiss et al. 2013; Marcy et al. 2014). These studies suggest that a transition from planets containing significant light material to rocky planets occurs at $\sim$2 $R_\oplus$, which would correspond to a mass of $\sim$5 $M_\oplus$ according to the mass-radius relation in Table 1.2. The authors acknowledge that these estimates are based on a small statistical sample and that the results may change for planets with larger orbital distances (longer periods). These values show a significant change from the classical estimate of 10 $M_\oplus$ for the critical mass. There are currently 425 confirmed planets with a radius below 2 $R_\oplus$ *or* mass less than 5 $M_\oplus$. However, of those potentially rocky planets, only 27 have vetted values for both mass and radius.[6] Exceptions to the proposed transition radius of $\sim$2 $R_\oplus$ have already been found. Dumusque et al. (2014) recently reported the discovery of Kepler-10c, which is a 17 ± 1.9 $M_\oplus$ planet with a radius of $2.35^{+0.09}_{-0.04}$ $R_\oplus$. With a density of 7.1 ± 1.0 g cm^{-3} Kepler-10c suggests that medium-sized planets can stay rocky rather than always becoming gaseous and bloated. Needless to say, continued effort to obtain mass measurements for roughly Earth-sized planets is important.

1.2.4 Additional Orbital Properties

Another interesting difference between detected exoplanets and our Solar System is the shape of the orbits (not to be confused with the "size," which is represented by the semimajor axis). Most exoplanets have substantial orbital eccentricities with an average around 0.16. This is in contrast to the Solar System which has an average for the planets of about 0.07. Combining this observation with the much broader range of orbital distances seen in exoplanets suggests a violent and vigorous formation history. For example, studies of gravitational scattering have been successful in reproducing the broad distribution of orbital eccentricities (Chatterjee et al. 2008) while studies of interactions between a planet

[6]Several more masses are known, but are still awaiting final confirmation before their values will be added to the exoplanet.org database.

and a protoplanetary gas disk may explain the presence of planets with orbital semimajor axes of only a few hundredths of an AU (Lin et al. 1996).

1.2.5 Some Interesting Examples

Before the first exoplanet detections, any speculation as to the existence and architecture of extrasolar systems had to be based solely on the example of our solar environment. With that limitation, it was only natural to assume the Solar System offered a typical example for other systems. Now that hundreds of extrasolar systems are known, it is safe to say that so far, our system appears to be anything but typical. The following are a few specific examples of interesting systems that are very different than our own.

The Kepler-11 system provides a very unique and unexpected example of a multiplanet system, containing six planets around a K-type star. Of those planets, three have masses of $\sim 2M_{\oplus}$, two have $\sim 8M_{\oplus}$, and the last is a massive giant planet. To find a system with such low mass is interesting. However, the picture becomes even more intriguing with the knowledge that all six of these planets are packed tightly together with the largest orbit at 0.5 AU. For reference, this is much less than the orbit of Venus around the Sun (at 0.7 Au). In addition, these planets have low densities, none of which are dense enough to be composed entirely of rock. In fact, the Kepler-11 planets are less massive for a given radius than most other planets with both mass and radius measurements (Lissauer et al. 2013). Consequently, this system has been a major source of interest for both dynamical considerations and formation models.

Other interesting examples are less about multiple planets than about multiple suns. It is estimated that binary stars are quite common in the galaxy. Yet, during the first decade and a half of planet detections, no planets were found in multiple star systems. Planets with two suns have long existed in the realm of science fiction. In 2011, that fantasy became one step closer to reality with the first unambiguous detection of a circumbinary planet (Doyle et al. 2011). Unlike the planets of our imagination, this planet (known as Kepler-16b) is cold, gaseous, and not thought to harbor life. Nevertheless, its discovery demonstrates the diversity of planets in our galaxy. Since that time, several more circumbinary planets have been detected and there has even been the discovery a circumbinary multiplanet system (Orosz et al. 2012). The system, Kepler-47, has two confirmed planets. Both planets are gas giants and one is believed to orbit in the habitable zone of the stars (see subsection 1.3.1). There is also recent evidence for the existence of a third planet; however, its detection has yet to be verified (Welsh et al. 2013).

1.3 Habitability

An attempt to define 'life' could require a completely independent study (Benner 2010) and one may expect to obtain different results depending on the context and motivation for the study. For this study, a definition of life used within the field of Biology is appropriate. This dissertation focuses environmental conditions (i.e. habitability) that are suitable for life, or at least, life as is understand on planet Earth. The sustained presence of liquid water on the surface of the Earth has played a crucial role in the development of life. Therefore, my working definition for planet habitability will be the requirement that physical conditions allow for the continued presence of liquid water on the surface of a terrestrial planet.

1.3.1 The Habitable Zone

Assuming that a planet has water on its surface, the primary consideration for habitability is the surface temperature. The major energy contribution is the radiation the planet receives from its parent star. Considerations of stellar radiation and climate have led to the definition of a "habitable zone" (hereafter referred to as "HZ") as the region around a star in which a terrestrial-mass planet with a CO_2-H_2O-N_2 atmosphere and a sufficiently large water content can sustain liquid water on its surface (Kopparapu et al. 2013b). If a planet is too close to a star, the surface temperature will be too hot for liquid water; whereas too far from the star will be too cold. The zone between the two extremes is a range of orbits where surface liquid water should be stable (Kasting et al. 1993).

The position of HZs around stars depends on the stellar type, luminosity class, and details of the planetary atmosphere. The concept of the HZ was proposed for the first time by Huang (1959). Since that time, it has been calculated by several other authors (Hart 1978; Kasting et al. 1993; Underwood et al. 2003; von Bloh et al. 2007; Selsis et al. 2007; Kaltenegger and Sasselov 2011). The main differences are in the climatic constraints imposed on the limits of the HZ by these studies. For the research presented in this dissertation, I have chosen to utilize an updated model proposed by Kopparapu et al. (2013b) which provides generalized expressions to calculate HZ boundaries around F, G, K, and M stellar spectral types. They used a one-dimensional, radiative-convective, cloud-free climate model, and assumed an Earth-mass planet with an H_2O (inner edge) or CO_2 (outer edge)-dominated atmosphere as their base model. Their calculations of the HZ boundaries relied on the so-called inverse climate modeling, where they specify a surface temperature and then use the model to calculate the corresponding stellar flux needed to sustain that temperature.

The work by Kopparapu et al. (2013b) produced a variety of limits for the inner and

outer edges of the HZ. This study utilizes their most conservative boundary estimates. These estimates are based on derived relationships between HZ stellar fluxes (S_{eff}) reaching the top of the atmosphere of an Earth-like planet and stellar effective temperatures (T_{eff}) in the range 2600 K $\leq$ Teff $\leq$ 7200 K:

$$S_{eff} = S_{eff\odot} + aT_\star + bT_\star^2 + cT_\star^3 + dT_\star^4, \tag{1.3}$$

where $T_\star$ = T_{eff} - 5780 K. The values of the coefficients are provided in Table 1.3. For these boundaries, the inner edge is based on the "moist-greenhouse" (or water-loss) limit. At this limit, the proximity to the star causes the water vapor content in the atmosphere to increase dramatically and become saturated. Once the stratosphere becomes wet, water molecules break down via photolysis and hydrogen is released. The hydrogen can then escape to space by the diffusion-limited escape rate, resulting in the eventual desiccation of the planet. With the HZ stellar flux, the corresponding HZ distances can be calculated using the relation

$$d = \left(\frac{L/L_\odot}{S_{eff}}\right)^{0.5} AU, \tag{1.4}$$

where $L/L_\odot$ is the luminosity of the star compared to the Sun.

Moving away from the star, the stellar flux received by the planet will decrease and the planet's temperature will drop. The outer edge of the HZ is based on the working hypothesis that as a planet cools, its atmospheric CO_2 will accumulate due to the negative feedback provided by the carbonate-silicate cycle. The additional CO_2 compensates for the decreased stellar flux through a greenhouse effect which backscatters infrared emissions from the surface. Below a certain temperature and pressure, the CO_2 will begin to condense out of the atmosphere and the greenhouse effect will no longer compensate for the low solar flux. For that reason, the outer orbital boundary is referred to as the "maximum greenhouse" limit.

Table 1.3. Coefficients to calculate habitable stellar fluxes, and corresponding habitable zones, for stars with 2600 K $\leq$ Teff $\leq$ 7200 K (Kopparapu et al. 2013a).

Constants	Moist Greenhouse (Inner Limit)	Maximum Greenhouse (Outer Limit)
$S_{eff\odot}$	1.0146	0.3507
a	8.1884 x 10^{-5}	5.9578 x 10^{-5}
b	1.9394 x 10^{-9}	1.6707 x 10^{-9}
c	-4.3618 x 10^{-12}	-3.0058 x 10^{-12}
d	-6.8260 x 10^{-16}	-5.1925 x 10^{-16}

Using the conservative limits represented by Equation (1.3), Equation (1.4), and Table 1.3, one can estimate the HZ for our Sun. The somewhat surprising result is an inner HZ boundary at 0.99 AU and an outer boundary at 1.67 AU. According to this estimate, the Earth (at 1 AU) is very near the hot edge of the Sun's habitable space, with Mars (at 1.52 AU) also located well within the estimate.

1.3.2 Additional Considerations for the Habitable Zone

A star's luminosity increases with age which causes the stellar HZ to migrate outward with time. As such, planets in the HZ at the current epoch may not have been habitable in the past. The idea of a continuously habitable zone has been introduced to deal with the luminosity evolution of the star and related studies have been performed (Underwood et al. 2003). As the name suggests, a continuously habitable zone is the region around a star in which a terrestrial planet can sustain liquid water on its surface for a specified period of time. With this extra condition, the requirement could be added that a circumstellar region receive sufficient flux for a planet to remain habitable long enough for life to emerge. Because my current study focuses only on the presence of liquid water, I do not introduce this extra condition. As such, my working definition of a HZ could be considered as the instantaneous habitable zone.

The definition of the habitable zone can be further complemented by the dynamical requirement that other planets in the system do not gravitationally perturb the terrestrial planets outside the zone. In such a case, a planet's orbital eccentricity about the star can cause it to spend a fraction of its year outside the HZ, which could result in large variations in temperature and atmospheric pressure. Previous studies have considered this effect (Williams and Pollard 2002; Menou and Tabachnik 2003; Pilat-Lohinger et al. 2008; Dvorak et al. 2010; Dressing et al. 2010). In addition to eccentricity considerations, Armstrong et al. (2014) explored the impact of obliquity variations on planetary habitability and found that such oscillations further expand habitable orbits. The result is that terrestrial planets near the outer edge of the HZ may be more likely to support life in systems that induce rapid obliquity oscillations as opposed to fixed-spin planets. For reasons explained in Chapter 5, the planetary systems considered in this dissertation do not necessitate either of these additional dynamical consideration.

1.3.3 Detected Planets in the Habitable Zone

Out of the many confirmed exoplanets, several HZ candidates have already been identified (Udry et al. 2007; Pepe et al. 2011; Borucki et al. 2011, 2012; Vogt et al. 2012; Tuomi

et al. 2013) and the number of HZ planet detections is expected to significantly increase with time (Batalha et al. 2013). I performed my own analysis of potential HZ planets using the conservative limits provided with Equations (1.3) and (1.4), and Table 1.3. In order to make a HZ estimation, measurements must be known for the radius (R_*) and effective temperature of the host star. From these, the stellar luminosity can be calculated using the well-known relationship:

$$L = 4\pi\sigma R_*^2 \, T_{eff}^4, \tag{1.5}$$

where σ is the Stefan-Boltzmann constant.

For extrasolar systems that lack necessary measurements, I can estimate the star's radius using an empirical relation derived from observations of eclipsing binaries (Gorda and Svechnikov 1999):

$$\log_{10}\frac{R_*}{R_\odot} = 1.03 \, \log_{10}\frac{M_*}{M_\odot} + 0.1, \tag{1.6}$$

where $R_\odot$ and $M_\odot$ are the radius and mass of the Sun, respectively. However, Equation (1.6) is valid only when $M_* \lesssim M_\odot$. If a star's effective temperature is unknown, but the stellar mass has been measured, the luminosity can be determined by,

$$\lambda = 4.101\mu^3 + 8.162\mu^2 + 7.108\mu + 0.065, \tag{1.7}$$

where $\lambda = \log_{10}(L/L_\odot)$ and $\mu = \log_{10}(M_*/M_\odot)$ (Scalo et al. 2007). From the stellar luminosity and radius, the effective temperature can be found using Equation (1.5). To compare orbital distances with Equation (1.4), I use the planet's semimajor axis as the average distance between the planet and host star. While this definition is not entirely accurate due to effects of orbital eccentricity, its use is sufficient for this simple analysis.

From my estimations, the number of HZ planet candidates represents just 4.5% of the total number of confirmed exoplanets (68 out of 1518). Of these candidates, 93% have masses similar to or greater than Neptune (17 $M_\oplus$), and are therefore most likely gas planets. Only 3 meet the latest estimates for a potentially terrestrial planet (radius $\lesssim 2$ $R_\oplus$ or mass $\lesssim 5$ $M_\oplus$, see subsection 1.2.3). A complete list of the HZ candidates and their properties is included in Table 1.4.

1.4 From Exoplanets to Exomoons

It has been almost 20 years since the first exoplanet orbiting a Sun-like star was detected. Since that time, the rate of planet detections each year has continued to increase and with it, the overall interest of the scientific community. The impressive achievements in exoplanet detection have revolutionized our understanding of the formation and evolution

Table 1.4: Properties of HZ planet candidates.
Parameter Source: exoplanets.org

Name	Mass ($M_\oplus$)	Radius $R_\oplus$	Semimajor Axis (AU)	Star Mass (M_{Sun})	T_{Eff} (K)
Kepler-186 f	-	1.1	0.4	0.5	3788
Kepler-62 f	-	1.4	0.7	0.7	4925
Kepler-283 c	-	1.8	0.4	-	4351
Kepler-174 d	-	2.2	0.8	-	4880
GJ 581 d	6.1	-	0.2	0.3	3498
HD 10180 g	21.4	-	1.4	1.1	5911
HD 192310 c	23.4	-	1.2	0.8	5166
HD 218566 b	67.6	-	0.7	0.8	4820
HD 137388 b	72.4	-	0.9	0.9	5240
HD 7199 b	93.7	-	1.4	0.9	5386
HIP 57050 b	94.6	-	0.2	0.3	3190
HD 215497 c	104.1	-	1.3	0.9	5113
HD 181720 b	118.2	-	1.8	0.9	5781
HD 99109 b	160.2	-	1.1	0.9	5272
HIP 14810 d	184.5	-	1.9	1.0	5485
GJ 876 c	194.5	-	0.1	0.3	-
HD 63765 b	204.6	-	0.9	0.9	5432
HD 34445 b	251.2	-	2.1	1.1	5836
HD 187085 b	255.4	-	2.0	1.1	6075
Kepler-68 d	257.3	-	1.4	1.1	5793
HD 10647 b	293.9	-	2.0	1.1	6105
HD 114729 b	300.2	-	2.1	1.0	5821
HD 73534 b	339.4	-	3.0	1.2	4884
HD 114783 b	351.1	-	1.2	0.9	5135
HD 28254 b	369.0	-	2.1	1.1	5664
HD 100777 b	370.2	-	1.0	1.0	5582
HD 147513 b	374.8	-	1.3	1.1	5930
tau Gru b	386.0	-	2.5	1.2	5999
HD 65216 b	386.5	-	1.4	0.9	5666
HD 210277 b	404.4	-	1.1	1.0	5555
HD 30562 b	423.4	-	2.3	1.3	5936
HD 23127 b	446.4	-	2.3	1.1	5752
HIP 5158 b	453.2	-	0.9	0.8	4962
HD 188015 b	467.0	-	1.2	1.1	5746
BD +14 4559 b	482.8	-	0.8	0.9	4814
16 Cyg B b	521.1	-	1.7	1.0	5674
HD 4113 b	523.7	-	1.3	1.0	5688
HD 82943 b	535.5	-	1.2	1.1	5997
mu Ara b	554.6	-	1.5	1.1	5784
HD 20782 b	603.7	-	1.4	1.0	5758
HD 190647 b	604.7	-	2.1	1.1	5628
GJ 876 b	618.6	-	0.2	0.3	-

Table 1.4 – *Continued*

Name	**Mass** ($M_\oplus$)	**Radius** $R_\oplus$	**Semimajor Axis** (AU)	**Star Mass** (M_{Sun})	$\mathbf{T}_{Eff}$ (K)
HD 5388 b	624.4	-	1.8	1.2	6297
HD 20868 b	638.4	-	0.9	0.8	4795
HD 4203 b	661.6	-	1.2	1.1	5702
HIP 79431 b	671.4	-	0.4	0.5	3191
HD 159868 b	699.1	-	2.3	1.2	5558
HD 163607 c	728.4	-	2.4	1.1	5543
HD 4732 c	751.5	-	4.6	1.7	4959
7 CMa b	772.9	-	1.8	1.3	4761
HD 23079 b	776.4	-	1.6	1.0	5927
HD 153950 b	871.3	-	1.3	1.1	6076
HD 125612 b	974.9	-	1.4	1.1	5897
HD 92788 b	1132.4	-	1.0	1.1	5836
HD 183263 b	1135.8	-	1.5	1.1	5936
upsilon And d	1307.8	-	2.5	1.3	6213
HD 16175 b	1391.6	-	2.1	1.3	6080
HD 213240 b	1440.2	-	1.9	1.1	5968
HD 13908 c	1630.1	-	2.0	1.3	6255
HD 28185 b	1842.1	-	1.0	1.0	5656
HD 190228 b	1888.1	-	2.6	1.8	5348
HD 10697 b	1981.2	-	2.1	1.1	5680
HD 86264 b	2105.9	-	2.8	1.4	6326
HD 222582 b	2424.5	-	1.3	1.0	5727
HD 23596 b	2460.3	-	2.8	1.2	5904
HD 141937 b	3010.8	-	1.5	1.0	5847
HD 136118 b	3711.6	-	2.3	1.2	6097
HD 16760 b	4223.6	-	1.1	0.8	5620

of planetary systems. With over a thousand confirmed detections and several thousand additional candidates, the focus of exoplanet research has begun to shift from detection to characterization.

Through the characterization of extrasolar systems, scientists take the first step towards detecting habitats outside the Solar System. An examination of life on Earth suggests that ecosystems require at a minimum: liquid water, a stable energy source, and a supply of nutrients. At present, no other planet in our Solar System shows an environment that combines all three basic requirements.[7] Yet, Earth is not the only object in our Solar System to contain liquids, heat, and nutrients. We know of at least three moons that possess those properties. They are the Jovian companion Europa, and the Saturnian satellites - Enceladus and Titan.

From the study of our local habitat, it also appears that plate tectonics are essential for maintaining habitability on Earth. Only three bodies in the Solar System, other than Earth, are known to show tectonic activity. Remarkably, these three objects are not planets, but moons: Jupiter's Io, Saturn's Enceladus, and Neptune's Triton. From these local examples, it would seem that satellite systems represent mini-solar systems with a richness and diversity all their own. As extrasolar planets are explored with increasing detail, a new class of objects may soon become accessible to observation by which I refer to extrasolar moons (or "exomoons"). These moons are the naturally occurring satellites of extrasolar planets and based on the structure of our Solar System, they may be even more abundant than planets.

1.5 Dissertation Outline

In this dissertation, I undertake a computational exploration into specific characteristics of theoretical exomoon systems. The habitability of the moons will be considered and the study will serve as an early attempt at exomoon characterization. Chapter 2 will provide additional interest in exomoon systems. This chapter will also include an overview of exomoon theory and current predictions for their detectability. The information presented will be used in Chapter 5 as a basis for constructing a hypothetical exomoon model.

In Chapter 3, I explain why M spectral type stars are receiving new interest as targets for extrasolar planets. Stars of this spectral type are often referred to as 'low-mass' or 'red dwarf' stars and they present certain advantages for detecting exoplanets in the HZ. The chapter ends with an explanation of how moons around giant planets in the HZ of

[7]However, there is evidence that Mars did have liquid water on its surface billions of years ago.

red dwarf stars do not face the same challenges to habitability as do the planets in these systems. However, potentially habitable exomoons around giant planets in the HZ of red dwarf stars do face challenges of long-term gravitational stability and tidal heating. These particular challenges represent the primary focus of this dissertation.

A brief introduction to tidal theory and the impact of tidal heating on habitability is provided in Chapter 4. As part of this introduction, I explain the limitations of popular tidal models for evaluating long-term tidal evolution in strongly interacting, many-bodied systems. For systems such as these, a unique method for calculating self-consistently the tidal, spin, and dynamical evolution is described. At the end of Chapter 4, I explain how this method is utilized to create a computational program for simulating the long-term tidal and dynamical evolution of hypothetical exomoons in red dwarf star systems. The parameters used to model low-mass stars, exoplanets, and exomoons are described in Chapter 5.

My primary investigation into exomoon habitability involved 3-body systems comprised of a giant planet, a Mars-like massive moon, and a M-dwarf central star. Using this newly created program, repeated simulations were performed to explore the tidal evolution of the moons in these systems. An explanation of the 3-body model and a discussion of the results is contained in Chapter 6. An extension to the 3-body simulations is described in Chapter 7. This extension involves a 4-body model where a second moon was added to the system and the effects of orbital resonance were explored. The implications on exomoon habitability in low-mass star systems is examined in Chapter 8. I then conclude with a look at related future work.

CHAPTER 2

EXTRASOLAR MOONS

2.1 Motivation

With so much attention being given to extrasolar planet detection and theory, it is interesting to note that the exploration of moons in the Solar System actually broadened our understanding of planet formation in our own system. Moons have been proposed as tracers of planet formation (Sasaki et al. 2010). Given the diversity and quantity of Solar System moons, it seems reasonable to envision a likewise abundant population of natural satellites around extrasolar planets. Therefore, an increased population sample through the detection of many extrasolar satellite systems could fundamentally reshape our understanding of formation processes.

At the time of this writing, no moon outside the Solar System has been detected. However, extrasolar moons continue to excite the imagination as to other possible habitats for extrasolar life (Reynolds et al. 1987; Williams et al. 1997; Heller and Barnes 2013). Now that current technology and theoretical methods are allowing for the detection of sub-Earth sized extrasolar planets, the first detection of an extrasolar moon appears to be on the horizon (Kipping et al. 2009; Kipping et al. 2012). With that in mind, it is useful to consider the expected properties and characteristics of exomoons, the results of which can be used to inform those that are currently working to achieve the first detection.

2.2 Formation

Two mechanisms have been proposed for the formation of satellites: (1) Formation from the disk material surrounding a planet. In this scenario, the objects will be "regular satellites" (always prograde) (Canup and Ward 2002). Examples in the Solar System are the Galilean satellites of Jupiter. (2) Formation by gravitational capture, impacts, or exchange interactions. These objects will be "irregular satellites" (either prograde or retrograde) (Jewitt and Haghighipour 2007). Only two examples of large irregular satellites are known, those being the Moon and Triton. While Triton is likely to have been gravitationally

captured by Neptune (Agnor and Hamilton 2006), the Moon's formation is more unique. The Moon is thought to have resulted from the collision between a Mars-sized planet, dubbed "Theia," and the primordial Earth (Taylor 1992).

The two satellite formation mechanisms are based on observations of our Solar System and are quite distinct from planet formation models. Previous studies have applied these mechanism to the formation of satellites in potential extrasolar systems (Canup and Ward 2006; Porter and Grundy 2011; Williams 2013). Their predictions for the maximum possible satellite mass varied depending on the formation model and the planetary system being considered. However, the studies do show the potential for massive satellites around extrasolar gas giants.

In-situ formation in the circumplanetary disk was shown to scale with planet mass, suggesting that the formation of a Mars-like[1] moon would be possible if it was around a super-Jovian mass planet. One the other hand, formation by capture is the mechanism believed to give the best chance for massive terrestrial satellites. In some cases, moons the size of Earth are feasible (Williams 2013). However, Heller et al. (2014) performed a detailed formation analysis and concluded that a more reasonable result is that of moons with roughly the mass of Mars. Captured moons would be classified as irregular satellites, which is beneficial since this does not constrain the expected properties in many ways.

2.3 Predicted Properties of Exomoons

Extrasolar moons are predicted to be abundant; however, as long as no such world is found, the science on extrasolar moons will remain theoretical. Regardless, predictions can be made as to their orbital evolution, physical properties, habitability, and ultimately, their detection.

2.3.1 Stability

After a moon has formed, its lasting survival can still be in question. Small gravitational perturbations from multiple satellites, the star, or from other planets can lead to chaos, ejections, and planet-satellite mergers.

For a system of three bodies consisting of a star, planet, and moon, the region in which the planet dominates the attraction of the moon[2] is known as the Hill sphere.[3] The radius

[1]Mars has a mass of 0.11 $M_{\oplus}$ and a radius of 0.53 $R_{\oplus}$.

[2]In the calculation, the moon is treated as a test particle (i.e. the mass of the moon is not important).

[3]Named after George William Hill who provided the definition.

of the sphere (R_H) is found by solving the restricted circular three-body problem and is equal to the distance of the L1/L2 Lagrange points:

$$R_H = a_P \left(\frac{M_P}{3M_*} \right)^{1/3}, \tag{2.1}$$

where a_P is the semimajor axis of the planet's orbit around the star, M_P and M_* are the masses of the planet and star, respectively.

In realistic scenarios, this simple picture does not accurately represent the complete stable region of an extrasolar moon. The critical semi-axis (a_{ps}) for a satellite to remain bound to its host planet is merely a fraction (f) of the Hill radius, i.e. $a_{ps} < f R_H$ (Holman and Wiegert 1999). A conservative choice for prograde satellites is $f = 1/3$ (Barnes and O'Brien 2002). Domingos et al. (2006) extended this consideration and showed that the actual stability region depends upon the eccentricity and orientation of the orbit. For prograde and retrograde moons, respectively, the stable regions are:

$$a_{sat,max}^{prograde} = 0.4895 R_H (1.0000 - 1.0305 e_P - 0.2738 e_{sat}) \tag{2.2}$$

$$a_{sat,max}^{retrograde} = 0.9309 R_H (1.0000 - 1.0764 e_P - 0.9812 e_{sat} + 0.9446 e_P e_{sat}), \tag{2.3}$$

where e_p and e_{sat} are the orbital eccentricities of the planet and satellite, respectively. These results suggest that retrograde moons can be found at significantly greater distances than their prograde counterparts. It can also be seen that planets on eccentric orbits offer severely reduced regions of stability for potential moons.

More recently, Donnison (2010) showed that moons on inclined orbits also yield contracted regions of orbital stability. As a result, moons are expected to be roughly coplanar with the planetary orbit. This conclusion is supported by the examples of massive satellites in our own Solar System.

Recent investigations on the dynamic stability of exomoon systems have expanded to include the effects of planet-planet scattering. Gong et al. (2013) found that when the architecture of a planetary system is the result of planet-planet scattering and mergers, planets will have most likely lost their initial satellites. This result includes the most massive giant planets if these planets were the product of former planet-planet mergers. In a complimentary study, Payne et al. (2013) considered giant planet systems that were tightly-packed, but initially stable. They found that giant exoplanets in closely-packed systems can very well harbor exomoon systems if the planet architecture avoids planet-planet mergers or ejections.

2.3.2 Evolution

Even for gravitationally stable systems, the moon's orbit will continue to evolve. The inclusion of tidal interaction between the planet and satellite can give rise to phenomena such as spin-orbit resonance and can even challenge a moon's long-term survival. Therefore, it is worthwhile to consider the effects of tides on the orbital evolution of a single planet-moon pair.[4]

Tidal bulges raised in both the planet and satellite will dissipate energy and apply torques between the two bodies. The rate of dissipation strongly depends on the distance between the two objects (see section 4.1 for a more detailed discussion of tidal theory). As a result of the tidal drag from the planet, a massive satellite orbiting a giant planet will have its rotation frequency braked and ultimately synchronized with its orbital motion around the planet (Dole 1964; Gonzalez 2005; Henning et al. 2009; Kaltenegger 2010; Kipping 2010). This effect is commonly known as tidal locking. Any initial obliquity will also be quickly eroded, causing the moon's rotation axis to be perpendicular to its orbit about the planet. In addition, a moon will inevitably orbit in the equatorial plane of the planet due to both the Kozai mechanism and tidal evolution (Porter and Grundy 2011). The combination of all these effects will result in the satellite having the same obliquity as the planet with respect to the circumstellar orbit. As for the host planet, massive planets are more likely to maintain their primordial spin-orbit misalignment than small planets (Heller et al. 2011). Therefore, satellites of giant planets are more likely to maintain an orbital tilt relative to the star than even a single terrestrial planet at the same distance from a star.

Tidal torques can also cause a moon to either spiral in or out, as a consequence of the conservation of angular momentum. The direction of the spiral actually depends on the tidal bulge raised in the planet (caused by the moon). If the planet's rotation period is shorter than the orbital period of the satellite, the bulge will lead (assuming prograde orbits) and the moon will slowly spiral outward. This action could eventually destabilize the moon's orbit, leading to its ejection. On the other hand, if the planet's rotation period is longer, the bulge will lag and the moon will slowly spiral inward. As this happens, the tidal forces on the moon become increasingly greater. If the inward migration continues past the Roche limit, the satellite can be disintegrated.

For planets with short orbital periods, the stability regions in which moons can reside will be tighter. As a consequence, the planet-moon tides will be greater, leading to a more rapid loss. For this reason, hot-Jupiters are generally considered to be unfavorable hosts. In

[4]Multiple moons are more complex due to the dynamical interactions that occur between the moons.

subsection 2.3.1, I indicated that retrograde satellites can be stable at far larger distances than prograde satellites. Therefore, retrograde moons have a larger distance over which to tidally spin-out or spin-in, which would ultimately allow for longer lifetimes.

Barnes and O'Brien (2002) provided analytical approximations for the maximum time an Earth-mass moon can survive when subject to stellar radiation similar to the solar flux received by Earth (i.e. when the moon is located in the HZ at an Earth-equivalent distance). They encouragingly predicted moons to be stable around Jupiter-like planets for habitable-zone periods if the host star's mass is greater than 0.15 $M_{\odot}$, where $M_{\odot}$ is one solar mass. Cassidy et al. (2009) claimed that an Earth-sized moon could maintain a stable orbit around a hot-Jupiter if the planet is rotationally synchronized to its orbit around the star.

Another dominant effect believed to cause the loss of moons is inward, disk-driven planetary migration. This type of migration for the planet occurs on a much faster time scale than tidal dissipation, causing the Hill radius of the planet to shrink very quickly. As a result, an initially stable moon can find itself outside the Hill sphere, and thus, be ejected. Namouni (2010) showed that a moon is unlikely to survive once a migrating gas giant crosses $\sim$0.1 AU. This is another reason why hot-Jupiters are unfavorable as satellite hosts.

2.3.3 Composition

Section 2.2 indicated that gas giant planets have the greatest potential for massive satellites. The composition of regular satellites around gas giants in the Solar System tend to be ice-rich with the rest being silicates and iron (Consolmagno 1983). The accepted explanation is that gas giants formed beyond the snow line where ice does not sublimate. Therefore, moons that form in situ (i.e. regular moons) have plenty of ice to accumulate in their formation (Pollack et al. 1996). One the other hand, the solar system satellites are also relatively low in mass and certainly less than ideal for considerations of habitability. Since formation by capture provides the greatest potential for the most massive satellites, the composition of higher mass irregular moons is more likely to resemble Mercury, Venus, Earth, and Mars.

2.4 Exomoon Detection Methods

The first technique ever proposed for the detection of an exomoon was made by Sartoretti and Schneider (1999). However, exomoon detection did not receive substantial interest until the more recent launch of NASA's Kepler space telescope (Kipping et al. 2009). The most

promising detection method relates to the transit of extrasolar planets. For a transiting planet, there are two categories of observational effects that can betray the presence of an exomoon (Kipping et al. 2012): (1) dynamical variations of the host planet, and (2) eclipse features induced by the moon. Dynamical effects primarily reveal information about the exomoon mass, whereas eclipsing features reveal information about the radius. Therefore, the detection of both effects allows for a measurement of the bulk density which can then be used to distinguish between different compositions (e.g. an icy moon versus a rocky moon). The following subsections provide a short review of these two categories.

2.4.1 Dynamical Effects on Transiting Exoplanets (TTV and TDV)

Dynamical effects are measured as perturbations in the motion of the host planet away from a simple Keplerian orbit. Let us consider a three-body planet-moon-star system. The planet and moon will orbit a common barycenter. In turn, the barycenter of the two bodies will orbit the star on a Keplerian orbit. It follows that the planet itself will not orbit the star on a truly Keplerian orbit. During transit, the planet's perturbed motion will be indicated by variations in the timing of the transit, as well as variations in the duration of the transit. Transit timing variations (TTV) and transit duration variations (TDV) are thought to be the most observable dynamical effects (Sartoretti and Schneider 1999; Szabó et al. 2006; Kipping 2009a, 2009b). TTV is more sensitive to wide-orbit moons (sensitivity scales as $\propto a_{sat}$) and deviations caused by terrestrial moons can range from a few seconds to a few hours. TDV is more sensitive to close-orbit moons (sensitivity scales as $\propto a_{sat}^{-1/2}$) and deviations can vary from a few seconds to tens of minutes in amplitude (Heller et al. 2014).

One disadvantage to the detection of these effects is that similar variations can also be induced by a multitude of other phenomenon. These include: general relativistic procession of the orbit; gravitational influences from other planets in the system or from a binary companion star; torques due to a spin-induced quadrupole moment of the star; tidal deformation in the planet or star;, and parallax effects. By itself, a single variational measurement is not particular useful. However, Kipping (2009a) predicted that TDV will lead TTV by a $\pi/2$ phase shift in amplitude, which offers a unique signature for exomoons. For this reason, both types of transit variations must be measured to have confidence of an actual exomoon detection. Also, with the combination of both measurements, the mass ratio between the planet and moon can be revealed.

2.4.2 Eclipse Features Induced by Exomoons

The second class of observational effect involves the transit of the moon itself. For this we can consider two types of eclipsing events. The first type is when the moon transits the star and causes a familiar transit shape on the stellar light curve. This type is referred to as "auxiliary transits" and is more likely to be detected for moons on wide orbits. The second eclipse effect is when the moon passes behind or in front of the planet during the planet-star transit. This latter type is often known as "mutual events" and is geometrically more probable for moons on close-in orbits. Unlike the dynamical effects, eclipses are sensitive to the size of the exomoon (and not the mass) and reveal information about the radius ratio between the satellite and the star.

When considering the direct eclipsing effects of exomoons, one major source of false-positives are starspot crossings (Rabus et al. 2009) as these will appear to be almost identical. Fortunately, starspots do not follow Keplerian motion, so their overall behavior should be distinguishable.

2.4.3 Direct Detection of Exomoons

As discussed in subsection 1.1.4, the direct imaging of exoplanets is extremely difficult. The difficulty is enhanced for planets in the stellar HZ due to very small angular separation and high contrast ratio between a star and planet. All current exoplanet images have involved well-separated systems that are still hot from formation rather than being heated by stellar irradiation. These young planets have effective temperatures around 1000 K (Heller et al. 2014). Intuition suggests that exomoons would be even more difficult to directly image. However, a moon that is hot from intense tidal heating could provide a sufficient target.

Peters and Turner (2013) recently proposed the direct imaging of tidally heated exomoons (THEMs). From an observational point of view, directly imaging exomoons has several advantages over the direct imaging of exoplanets. Unlike exoplanets, THEMs retain their internal heat and can remain hot and luminous for significantly longer timescales, allowing them to be visible around both young and old stars. Additionally, THEMs do not require substantial amounts of stellar irradiation to remain hot. Therefore, they may be luminous at large separations from the central star. Assuming THEMs exist and are common, Peters and Turner (2013) showed that Spitzer's IRAC could detect an exomoon the size of Earth with a surface temperature of 850 K and at a distance of five parsecs (pc) from Earth. Future instruments such as JWSTs Mid-Infrared Instrument (MIRI) have even more potential for directly imaging exomoons.

2.4.4 Detection Outlook

Some additional constraints to the detection of moons around transiting exoplanets include photometric noise, instrumental noise, and natural stellar variability. Kipping et al. (2009) considered these constraints and performed a detailed analysis of TTV and TDV detection with Kepler-class photometry and obtained a lower detection limit of about 0.2 $M_{\oplus}$ for moons orbiting in the stellar HZ of M, K, and later-G type stars. Lewis (2011) investigated the effects of noise filtering and found that exomoons hidden in the Kepler data will need to have radii $\gtrsim 0.75\ R_{\oplus}$ to be detectable by direct eclipse effects. While exomoon detection is certainly challenging from a theoretical and experimental standpoint, these predictions offer hope that the first detection is on the horizon.

Besides the transit method, other traditional planet detection techniques have been considered for exomoon detection (Lewis et al. 2008; Morais and Correia 2008; Liebig and Wambsganss 2010; Peters and Turner 2013) including direct imaging, microlensing, pulsar timing, astrometry, and radial velocity. Unfortunately, their estimated potential for success appears to be unlikely at best. For this reason, I will forego any further discussion concerning these methods.

2.5 Exomoon Habitability

In section 2.2, I discussed predictions for exomoons the size of Mars orbiting gas giants. I also detailed the expectation for near-future detection of exomoons with roughly that same size in subsection 2.4.4. These statements naturally lead to questions about the habitability of these worlds. In this section, I consider some of the properties that factor into this determination.

2.5.1 Mass Requirements

Lower boundary mass constraints start with the need to sustain a magnetic shield on a billion year timescale, which is necessary to protect life on the surface from high-energy stellar and interstellar radiation. For this, Tachinami et al. (2011) argued that a terrestrial world needs a mass $\gtrsim 0.1\ M_{\oplus}$. Another condition is that a moon must hold a substantial and long-lived atmosphere. Previous studies suggest that this would require satellite masses $M_{sat} \gtrsim 0.12\ M_{\oplus}$ (Williams et al. 1997; Kaltenegger 2000). Finally, sufficient mass is needed to drive tectonic activity over billions of years. Williams et al. (1997) proposed that $M_{sat} \gtrsim 0.23\ M_{\oplus}$ is mandatory to entertain plate tectonics and to promote the carbon-silicate cycle. Combining these constraints for habitability with formation theory and modern

technology points toward a preferred mass regime between 0.1 and 0.2 $M_{\oplus}$ for habitable exomoons that can be detected in the near future.

These mass limits for habitable worlds were all derived by assuming a cooling, terrestrial body such as Mars. However, there is an alternative internal heat source for exomoons that is typically less important for planets located in the HZ. This energy source is tidal heating and its effects can retard the cooling of the moon and thus maintain the aforementioned processes over longer epochs than in planets. Several studies have addressed the importance of tidal heating and its effects on the habitability of exomoons (Reynolds et al. 1987; Scharf 2006; Henning et al. 2009; Heller 2012; Heller and Barnes 2013; Heller and Zuluaga 2013). Reynolds et al. (1987) was the first to suggest the remarkable possibility that tidal heating, rather than stellar illumination, could maintain habitability in water-rich extrasolar moons beyond the stellar HZ. Support for their claim was given by findings of plankton in Antartica lakes which require an amount of solar illumination corresponding to the flux received at the orbit of Neptune. The theory of tidal heating and a personal investigation into its effects on exomoons is presented in Chapter 4.

2.5.2 Global Energy Flux

When considering exoplanet habitability, primary energy concerns involve the average stellar flux received by a parent star. Investigations of exomoon habitability can be distinguished from studies on exoplanet habitability by other various astrophysical effects. For example, a moon's climate can be affected by the planet's stellar reflected light and its thermal emission. Moons also experience eclipses of the star by the planet, and tidal heating can provide an additional energy source that is typically less substantial for planets. Heller and Barnes (2013) considered these effects individually, and then combined them to compute the orbit-averaged global flux F_{glob} received by a satellite. More specifically, this computation summed the averaged stellar, reflected, thermal, and tidal heat flux for a satellite. In their study, they provided a convenient definition for the global flux as

$$F_{glob} = \frac{L_*(1-\alpha_s)}{16\pi a_{*p}^2\sqrt{1-e_{*p}^2}}\left(1+\frac{\pi R_p^2\alpha_p}{2a_{ps}^2}\right)+\frac{R_p^2\sigma_{SB}(T_p^{eq})^4}{a_{ps}^2}\frac{1-\alpha_s}{4}+h_s \quad , \tag{2.4}$$

where L_* is the luminosity of the star, a_{*p} is the semimajor axis of the planet about the star and a_{ps} is the satellite's semimajor axis about the planet, α is the bond albedo, e is eccentricity, σ_{SB} is the Stefan-Boltzmann constant, and h_s is the tidal heat flux in the satellite (refer to section 4.2). The planet's thermal equilibrium temperature T_p^{eq} is defined as

$$T_p^{eq} = \left[\frac{T_{eff,*}^4 (1 - \alpha_p) R_*^2}{4 r_{*p}^2} \right]^{1/4} , \tag{2.5}$$

where $T_{eff,*}$ is the effective temperature of the star, and r_{*p} is the distance between the planet and the star.

As an analogy with the circumstellar HZ for planets, there is a minimum orbital separation between a planet and moon that will allow the satellite to be habitable. Moons inside this minimum distance are in danger of runaway greenhouse effects by stellar and planetary illumination and/or tidal heating. There is not a corresponding maximum separation distance (other than stability limits) because satellites with host planets in the stellar HZ are habitable by definition. The benefit of Equation (2.4) is that it can be used to explore the minimum distance. This is accomplished by comparing the global flux to estimates of the critical flux for a runaway greenhouse (F_{RG}). Pierrehumbert (2010) used a semi-analytical approach to calculate F_{RG} as

$$F_{RG} = o \, \sigma_{SB} \left(\frac{l}{R \, ln \left(P' / \sqrt{\frac{2 P_0 g_s (M, \, R_s)}{k_0}} \right)} \right)^4 \tag{2.6}$$

with

$$P' = P_{\text{ref}} \exp \left\{ \frac{l}{R \, T_{\text{ref}}} \right\} , \tag{2.7}$$

where $P_{\text{ref}} = 610.616$Pa, l is the latent heat capacity of water, R is the universal gas constant, $T_{\text{ref}} = 273.13$K, $o = 0.7344$ is a constant designed to match radiative transfer simulations, P_0 = 104Pa is the pressure at which the absorption line strengths of water vapor are evaluated, $g_s = GM_s/R_s^2$ is the gravitational acceleration at the satellite's surface, and $k_0 = 0.055$ is the grey absorption coefficient at standard temperature and pressure. Applying Equation (2.6) to an Earth-mass exomoon gives a critical flux of 295 W/m^2 for a water-rich world with an Earth-like atmosphere to enter a runaway greenhouse state.

CHAPTER 3

INTEREST IN LOW-MASS STARS

3.1 Red Dwarfs

Compared to the Sun, red dwarf stars are smaller, cooler, fainter, and lower-mass (refer to Figure 3.1). Nonetheless, they are the predominant stellar population of our Galaxy (e.g. Chabrier and Baraffe 2000). Stars in this category are mostly of M spectral type, with typical surface temperatures less than 4,000 K. Red dwarfs range in mass from $\sim$0.075 $M_{\odot}$ to about 0.5 $M_{\odot}$. The lower limit represents the hydrogen burning mass limit (Burrows et al. 1997) which is conversely the upper limit for a brown dwarf. It is estimated that 75% of the stars within 10 pc of Earth are M dwarfs (Henry et al. 2006). These stars are intrinsically fainter than solar-type stars. While they may dominate the stellar mass budget in galaxies, they contribute only a few percent of the total light (Conroy and van Dokkum 2012). This fact is made clear considering there are no M dwarf stars visible to the naked eye.

Due to their large numbers, low-mass stars may be the most abundant planet hosts in our Galaxy and for this reason, they have received added attention in recent years. Also cause for attention, low-mass stars present certain advantages for detection. The radial velocity signal is proportional to $M_{*}^{-2/3}$. Hence, a lower stellar mass will produce a larger RV signal for a given planet mass and orbit. This makes sense considering a higher planet/star mass ratio will move the system's center of mass away from the star, resulting in greater reflex motion. Another detection advantage comes from their smaller radius. The transit depth for a star's light curve is proportional to R_{*}^{-2} (see Equation (1.1)). As such, the transit signal for a given planet radius should be readily distinguishable. For example, an Earth-size planet orbiting a 3800 K dwarf star has a transit signal that is 3.3 times deeper than the signal for an Earth-size planet across a G star. This is due to the dwarf star being only 55% the size of the Sun.

While the advantages are worth pointing out, there is also a down side to the low mass and small size. The geometric probability for transit is directly proportional to the stellar

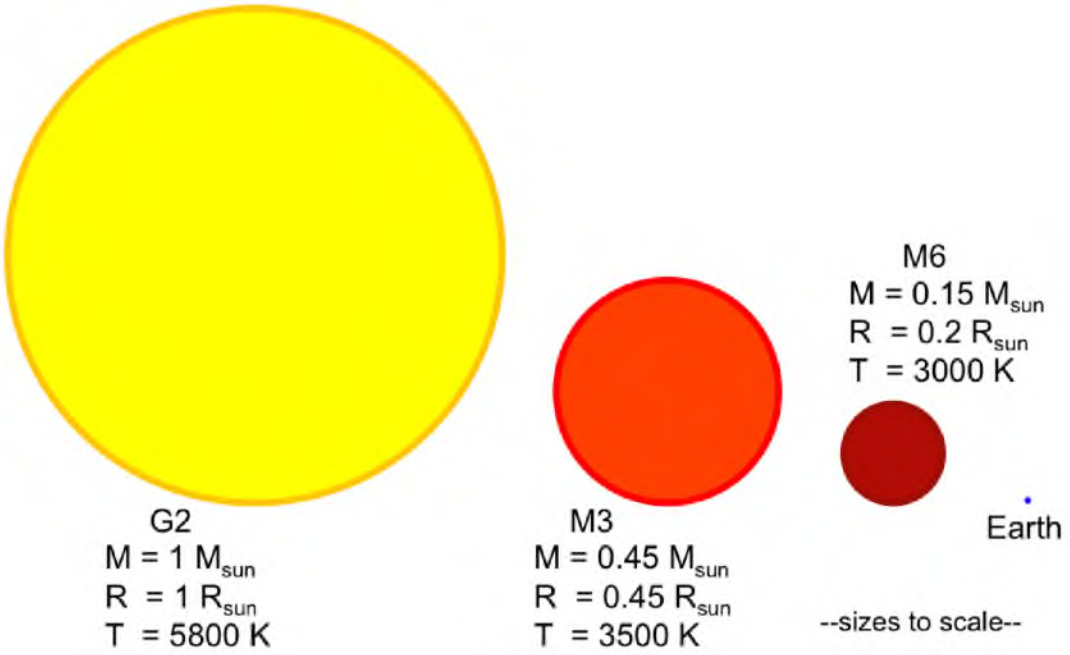

Figure 3.1. Illustrative comparison between low-mass stars and the Sun. Earth is also represented for contrast. The radius of Earth is less than 1% the radius of the Sun.

radius (see Equation (1.2)). Therefore, transits can also be less probable for a given orbital distance. Additionally, M dwarfs are much fainter than massive stars so there can be fewer visible stars in any given field of view. The faintness also leads to smaller signal-to-noise ratios. To overcome these obstacles, large surveys require the use of bigger telescopes and better spectrographs with more sensitive calibration.

3.1.1 Detected Planets

The RV technique was the first to unveil a candidate planet orbiting an M dwarf star (Delfosse et al. 1998; Marcy et al. 1998). The detected planet was a gas-giant with a minimum mass double that of Jupiter and an orbital distance only 20% of Earth's distance from the Sun. At this point in time, the detection of such a planet was not particularly revolutionary. The discovery was significant in that it proved planets could indeed form around low-mass stars.

Of the 1518 total confirmed exoplanet detections, only 79 involve low-mass (red dwarf) star systems. While this number represents a small fraction of the total, the majority of these detections occurred only recently and the number is expected to grow. To a certain extent, the lack of known planets around M dwarfs is due to early observational biases. Until recently, the strong majority of exoplanets detections came from RV surveys

and early surveys did not target these faint stars because of the difficulties in obtaining sufficiently high signal-to-noise observations. Dwarf stars are particularly faint at optical wavelengths where the most high-precision spectrometers operate, with the bulk of their spectral energy emitted at wavelengths in the near infrared. The activity of the stars themselves also complicate detection with the presence of apparent RV and photometric variations by co-rotating features (star spots) and temporal variations of the stellar surface (Reiners et al. 2010).

The fact that the first detected exoplanet around an M dwarf was a giant planet gave the early impression that such planets could be common around late-type stars. Today, 17 of the 79 exoplanets found around low-mass stars have masses equal to or greater than Saturn ($\sim$ 95 $M_{\oplus}$). This suggests that the ratio of giant planets to lower mass planets in these systems is not as high as once thought.

In comparison to other host stars, there is continuing evidence that the occurrence rate for giant planets is lower in red dwarf systems than it is for Sun-like stars (Butler et al. 2004; Endl et al. 2006; Johnson et al. 2007; Cumming et al. 2008). Bonfils et al. (2013) conducted a radial velocity survey of M-dwarfs and concluded that giants planets (m sin$i$ = 100 - 1000 $M_{\oplus}$) have a low frequency whereas super-Earths (m sin$i$ = 1 - 10 $M_{\oplus}$) are likely very abundant. Their results are in agreement with similar studies of small planets around small stars (Dressing and Charbonneau 2013; Morton and Swift 2013; Tuomi et al. 2014). Note that these studies typically only involved planets with short orbital periods (less than 100 days) due to the limited sample of known orbits. Studies also show several high-multiplicity systems around M dwarfs consisting of only super-Earths or Neptune-like planets (Udry et al. 2007; Bonfils et al. 2013; Bonfils et al. 2013). Examples include the highly studied GJ 581 system of four confirmed[1] planets, which include a 6 $M_{\oplus}$ planet located on the outer edge of the estimated habitable zone (HZ) for the system (Forveille et al. 2011).

3.2 Habitable Zones Around Red Dwarf Stars

As a consequence of their low mass, the rate of thermonuclear fusion is significantly less than even Sun-like stars. Red dwarfs therefore develop very slowly and once they reach the main sequence are capable of maintaining a constant luminosity and spectral type for some trillions of years (Laughlin et al. 1997). Because they have negligible brightening

[1]Two additional planet detections have been reported for this system. However, their existence is heavily disputed.

while on the main sequence, the liquid water HZ undergoes no radial expansion during this time. However, the lower core temperatures and decreased energy output result in a HZ that is much closer to the star. An illustration of the change in HZ boundaries with stellar mass is provide in Figure 3.2. The represented limits are the conservative limits defined in subsection 1.3.1.

The proximity of the HZ around low-mass stars has an advantageous effect on the detectability of planets in this region. A radial velocity signal is proportional to $a^{-1/2}$, where a is the semimajor axis of the planet's orbit. This inverse dependency is again (see section 3.1) due to the shift in the center-of-mass away from the star leading to a higher amplitude RV signal for close-in planets. For example, the RV signal induced by a 1 $M_{\oplus}$ planet in the middle of the HZ of a 3800 K, 0.55 $M_{\odot}$ dwarf is 23 cm s^{-1}, while a signal for

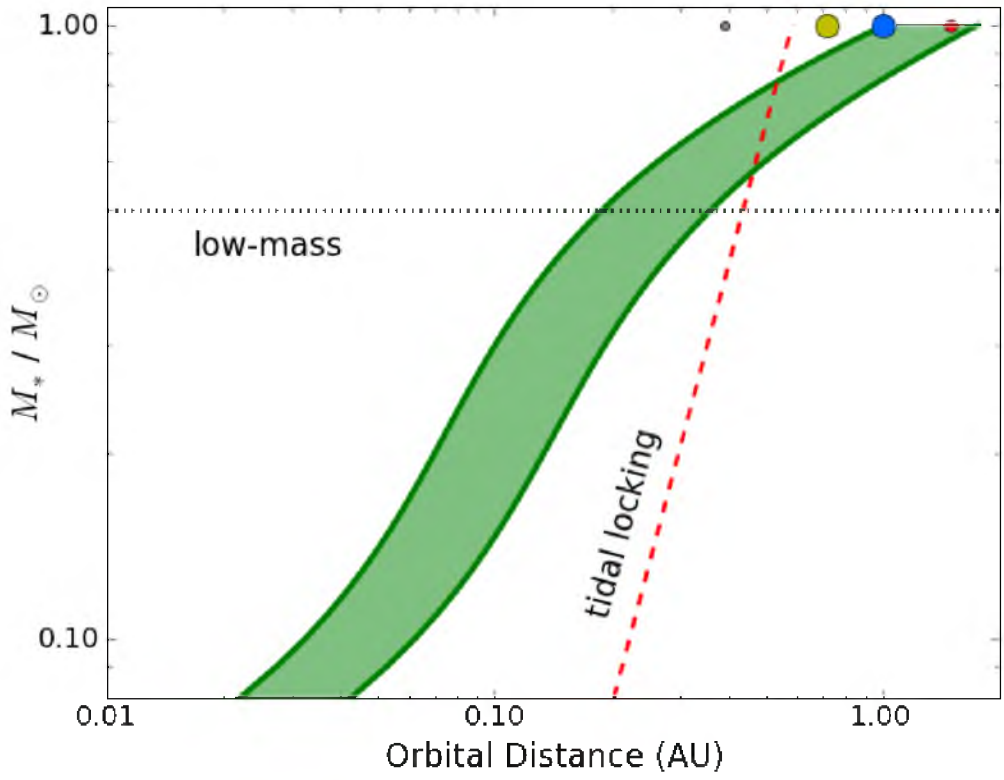

Figure 3.2. Habitable zones with planet mass. The dotted black line represents the upper red dwarf (low-mass) star boundary. The red dashed line represents the tidal locking radius. The colored circles represent the orbital distances of Mercury, Venus, Earth, and Mars. The size of each circle is scaled to the planet's size relative to Earth (but not to scale with the horizontal coordinates).

the same planet in the HZ of a G star is 9 cm s^{-1} (Dressing and Charbonneau 2013). The prospects are even better for planets around mid-to-late M dwarfs where a similar setup around a 3200 K dwarf would produce an RV signal of 1 m s^{-1} which is achievable with the current precision of modern spectrographs (Dumusque et al. 2012).

Transit surveys also benefit from shorter orbital distances in the HZ. The geometric probability of transit is inversely proportional to the semimajor axis and therefore increases with smaller values. This probability increase would more than compensate for the decrease due to the direct dependency on stellar radius (refer to section 3.1). In addition, shorter distances result in shorter orbital periods for planets. This is a benefit to both the RV and transit techniques as it allows for more orbital phases to be sampled in data covering a fixed length of time. As an example of these advantages, the transit of a planet in the HZ of a G star happens only once per year, while a transit occurs five times per year for a planet in the HZ (~0.3 AU) of a 3800 K dwarf star. In addition, the geometric probability that a transit will actually occur relative to our line of site is 1.8 times greater.

Bonfils et al. (2013) used their RV survey to calculate the frequency of habitable planets[2] orbiting M dwarfs and estimated a value of $0.41^{+0.54}_{-0.13}$. Kopparapu (2013) performed an independent study of the occurrence rate of terrestrial planets in the HZ[3] of M-dwarfs using *Kepler* (transit) data and determined a frequency of $0.51^{+0.10}_{-0.20}$ per star as a conservative estimate. Within the uncertainties, the estimates agree for the two studies. Considering that M dwarfs dominate the stellar count, these estimates suggest a significantly high frequency of habitable planets in our galaxy.

Subsection 1.3.3 contains my own analysis of HZ exoplanets using an online database[4] of confirmed exoplanets. Of the 68 candidates, only 6 were found around dwarf stars. Table 3.1 provides a list of these planets and their parameters. It is interesting to note that 4 of the 6 candidates have planet masses near that of Saturn (~95 $M_\oplus$) or greater. While giant planets in the HZ of dwarf stars are predicted to be much less frequent than Earth-like planets, the current *confirmed*[5] detections have not yet caught up with this prediction.

---

[2]They define a habitable planet as one with $m \sin i$ between 1 $M_\oplus$ and 10 $M_\oplus$, which also orbits in the HZ of the star. Their HZ boundaries were defined by Selsis et al. (2007).

[3]He defined a terrestrial planet as having a radius between 0.5 $R_\oplus$ and 2 $R_\oplus$ and used the conservative HZ boundaries defined in Kopparapu et al. (2013a).

[4]exoplanets.org.

[5]However, there are also more than three thousand unconfirmed Kepler candidates, many of which are believed to have radii between 0.5 and 4 $R_\oplus$.

Table 3.1. Properties of HZ planet candidates that orbit low-mass stars. Parameter Source: exoplanets.org

Name	**Mass** ($M_\oplus$)	**Radius** $R_\oplus$	**Semi-Major Axis** (AU)	**Star Mass** (M_{Sun})	$\mathbf{T}_{Eff}$ (K)
Kepler-186 f	-	1.1	0.4	0.5	3788
GJ 581 d	6.1	-	0.2	0.3	3498
HIP 57050 b	94.6	-	0.2	0.3	3190
GJ 876 c	194.5	-	0.1	0.3	-
GJ 876 b	618.6	-	0.2	0.3	-
HIP 79431 b	671.4	-	0.4	0.5	3191

Fortunately, upcoming facilities such as the James Webb Space Telescope and the Giant Magellan Telescope will be capable of detecting Earth-sized planets in the HZs of M dwarfs. It is even expected that they will be able to take spectra of these planets.

As mentioned above, dwarf stars on the main sequence evolve slowly, which can be seen as a benefit for the development of life in the HZ. However, the close proximity to the star also introduces unique concerns for potentially habitable environments.

3.2.1 Concerns for Habitability

The habitability of red dwarf systems is a subject of some debate. One of the main arguments against the potential for habitable planets is the issue of tidal locking. Because the HZ is so close to the star, tidal interactions will most likely cause the rotation of the planet to synchronize with its orbital period around the star. The result being that the same side of the planet will always face the star. The distance at which tidal locking is most likely to occur (in relation to stellar mass) is known as the tidal locking radius. This distance is included in Figure 3.2.

Early studies have suggested that a hypothetical planet in the HZ of an M dwarf star would be inhospitable due to tidal locking (Dole 1964; Kasting et al. 1993) mainly because the atmosphere would freeze out on the dark side of the planet. Later work on the topic was actually more optimistic. Haberle et al. (1996) and Joshi et al. (1997) demonstrated that sufficient quantities of carbon dioxide could sustain circulation between the light and dark side and prevent the atmosphere from freezing. More recent models even allowed for ocean-covered water worlds (Joshi 2003). Tarter et al. (2007) similarly studied the ability of a very dense atmosphere to thermally distribute solar radiation and agreed that tidally locked synchronous rotation in the HZ does not necessarily lead to atmospheric collapse. Moreover, not all planets inside the tidal locking radius will become spin-synchronized.

Another option is to become trapped in a spin-orbit resonance, as is the case for Mercury in our own Solar System. Mercury orbits inside the tidal locking radius, yet maintains a 3:2 resonance rotating three times for every two orbits around the Sun. Tidal locking is also a concern in that it may inhibit the generation of convection in a liquid metal core and dimish magnetic field strength to nonhabitable levels.

Besides the dynamical concern of tidal locking, the low-mass stars themselves cause reason for concern. While M dwarfs on the main sequence are capable of maintaining very stable luminosities for extremely long timescales, the situation is much different for the pre-main sequence phase. The luminosity of M dwarf protostars is much more variable than in later years. The lowest mass M stars take 0.3 - 1 Gyrs to reach the main sequence, during which time the luminosity decreases by roughly two orders of magnitude (Laughlin et al. 1997; Scalo et al. 2007). Considering that planets in the HZ of dwarf stars are expected to form more quickly than around Sun-like stars (Lissauer 2007), this behavior is problematic for future habitability. Planets that formed early and near the HZ are forced to endure a period of high energy flux and high temperatures which would likely deplete any existing atmosphere of useful volatiles. As a result, an early origin for life may be delayed or even permanently disabled. Of course, an alternative to this is if the planet forms further out and then migrates in at a later time.

Another area for concern is that M stars exhibit extreme and intermittent variability due to their strong magnetic activity. However, these events occur on very small timescales of hours up to years. The activity manifests itself as intense flares similar to solar flares, but scaled up in frequency and relative energy output. Even in their quiescent state, low-mass stars have high UV emission compared to Sun-like stars (France et al. 2013). The flares would be most harmful to planets without a strong magnetic field requiring several years to rebuild an ozone layer after experiencing a strong flare, although the presence of a thick atmosphere should effectively screen out most of the UV flux keeping the majority from ever reaching the surface of a planet. For this reason, flares are not considered an insurmountable obstacle to habitability in these systems (Tarter et al. 2007; Segura et al. 2010).

A very different kind of short-term variability for M dwarfs is due to large-amplitude star spots. Most spots reduce the stellar flux by less than a few percent (Messina et al. 2003). However, Joshi et al. (1997) found extreme spot cases that reduce the flux of the star by up to 40% for a few months. Such a decrease would significantly effect the surface temperature of a HZ planet, potentially causing some regions to occasionally suffer a severe freeze. However, Joshi et al. (1997) reported that the atmosphere itself did not freeze out.

Fortunately, most M stars do not experience such extreme spot variations.

3.3 So Why Bother with Exomoons

Heller and Barnes (2012) recently considered the question as to why we should bother with the habitability of exomoons when it is yet so hard to characterize even planets. Their reasons include:

(1) If they exist, then the first detected exomoons will be roughly Earth-sized (i.e. have masses $\gtrsim 0.2\ M_{\oplus}$) (Kipping et al. 2009).

(2) Moons are expected to become tidally locked to their host planet. As a result, exomoons in the HZ have days much shorter than the stellar year. This is an advantage for their habitability compared to terrestrial planets in this zone which become tidally locked to the star.

(3) Massive host planets of satellites are more likely to maintain their primordial spin-orbit misalignment than small planets (Heller et al. 2011). An extrasolar moon in the stellar HZ will likely orbit a massive planet in its equatorial plane (Porter and Grundy 2011). Thus, it is much more likely to experience seasons than a single terrestrial planet at the same distance from the star.

(4) Extrasolar habitable moons could be much more numerous than planets. Subsection 1.3.3 documents that most of the detected HZ candidate planets have masses similar to or greater than Neptune. In addition, subsection 1.2.2 explains that Neptune-like planets appear to be common in our galaxy. Based on the number of moons around gas planets in our Solar System, it seems feasible for extrasolar gas planet to also have an abundance of moons.

Beyond the reasons listed above, there is also the concept of tidal heating as an additional energy source for habitability which can be more prominent in moons than in planets. A discussion of exomoon tidal heating is even more relevant for low-mass star systems due to the close proximity of the HZ and the corresponding increase in gravitational influence from the star. This influence may act to perturb a satellite's orbit in such a way as to increase the tidal heating rate. For this reason, an exploration into the tidal evolution of exomoons in low-mass star systems will be the primary topic for the remainder of this dissertation.

CHAPTER 4

DYNAMICAL AND TIDAL EVOLUTION

Scientific studies of tides extend back to at least the early 1600s with Johannes Kepler's work on celestial motion (Caspar 1962). However, at that time, there were only six planets and five satellites (our Moon and the four Galilean satellites) known to study. The modern day discovery of thousands of extrasolar bodies has motivated more recent interest in the effect of tides as an important orbital and physical property of extrasolar planets.

While red dwarf stars provide attractive candidates for HZ planet detections, tidal influences between a planet and star present concerns for habitability that are somewhat unique to this class of star (see subsection 3.2.1). Chapter 3 presented reason for investigation into the habitability of moons around massive planets in the HZ of low-mass stars. This chapter will develop a model which considers the many-body interactions between low-mass stars and their hypothetical planet-moon binaries. Such a model can then be utilized to find constraints on the potential for massive moons to have liquid surface water.

4.1 Tidal Heating

A quantitative explanation for the creation of tides in a planet-moon system (or any massive binary sytem) is based on two concepts. The first is that the universal force of gravity has a strong dependence on distance ($1/r^2$ dependence). The second is simply that planetary objects are large. As such, the side of the moon closest to the planet experiences a stronger force than the far side (see Figure 4.1(a)). Relative to the gravitational force at the center of the moon, the differential forces inside the moon act to elongate the moon in the direction of the planet while also compressing its body in the perpendicular direction (see Figure 4.1(b)). The overall effect of the differential forces is the production of a tidal bulge in the moon. A similar description can be given for tides created in the planet.

The resulting nonspherical shapes of the planet and moon can lead to torques that will influence their rotation rates. I discussed in subsection 2.3.2 the phenomenon of tidal locking and the potential for inward/outward spiraling of a satellite due to tidal

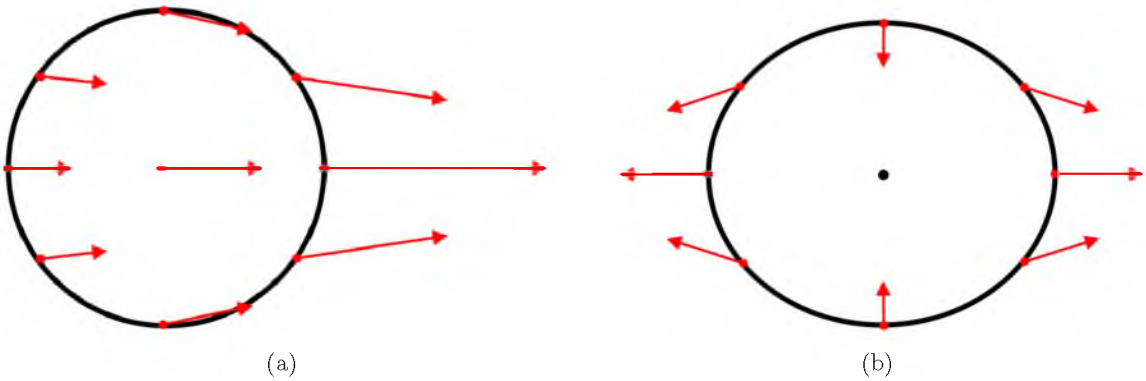

Figure 4.1. An illustration depicting distortion caused by tidal interactions. (a) The gravitational forces on a moon from a planet (assuming the planet was located to the right of the moon). (b) The differential gravitational force on a moon, relative to its center.

interactions. However, it is not always recognized that the same tidal forces responsible for those effects can also act to both heat the satellite and circularize its orbit. This occurs for noncircular orbits when orbital energy is transfered via heat through the process known as tidal heating. The underlining cause for tidal heating is simply that an eccentric orbit signifies continually varying distances between the planet and moon. As the distance varies, so does the gravitational forces between the two objects. This, in turn, leads to varying differential forces inside the moon and planet. As the differential forces change, so do the shapes. This generates heat from internal friction as their bodies are stretched and compressed. A simplified graphical depiction of my description is provide in Figure 4.2.

Several quantitative models for tidal heating have been proposed (e.g. Hut 1981; Efroimsky and Lainey 2007; Ferraz-Mello et al. 2008; Jackson et al. 2008a; Hansen 2010). However, the exact mechanisms of tidal dissipation are still poorly understood (Barnes et al. 2009). A conventional model quantifies the tidal heating (H) of a satellite in an isolated binary system as

$$H = \frac{63}{4} \frac{(GM_P)^{3/2} M_P R_{sat}^5}{Q'_{sat}} a^{-15/2} e^2, \tag{4.1}$$

where G is the gravitational constant, M_P is the mass of the host planet, R_{sat} is the satellite radius, and Q'_{sat} is the tidal dissipation "function," while a and e are the satellite's semimajor axis and eccentricity relative to the planet. It should be noted that this model may break down for large e. Nevertheless, the equation shows the strong dependence on the size and shape of the satellite's orbit. Consequently, tidal heating drops off quickly with increasing distance and altogether ceases for circular orbits ($e = 0$).

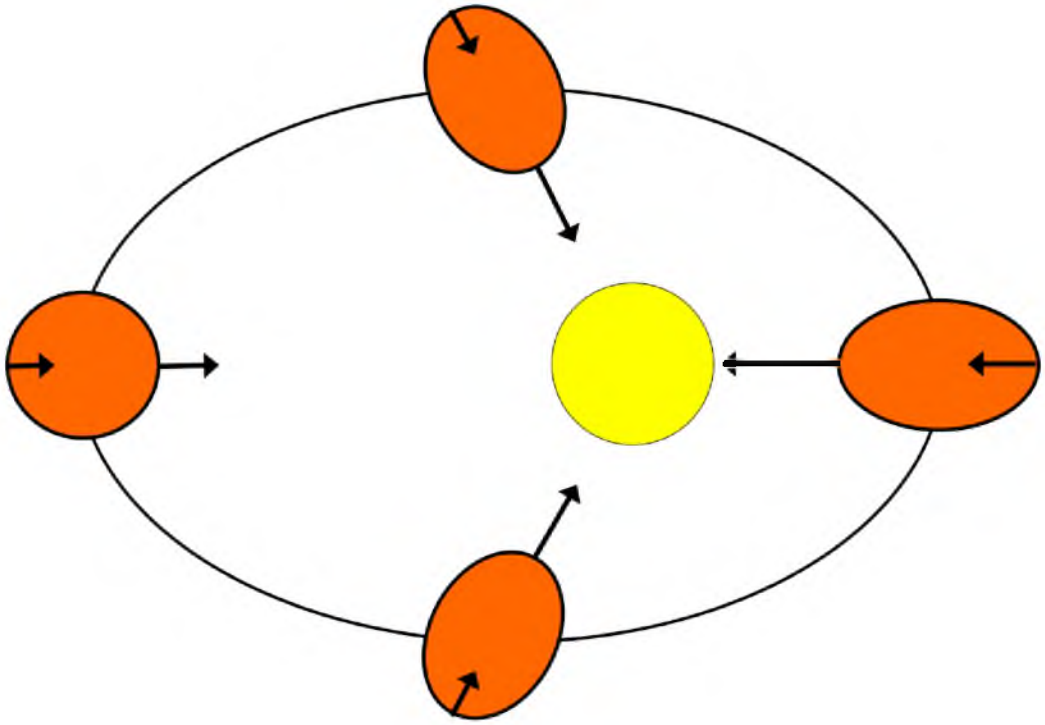

Figure 4.2. A very simple depiction of the orbital effects that produce tidal heating.

Because tidal heating represents a loss of orbital energy, the effects of dissipation act to decrease the moon's semimajor axis, while also decreasing the eccentricity. The latter is a consequence of angular momentum conservation. The timescale for which the eccentricity is damped can be estimated as (see Murray and Dermott (1999), Equation 4.198)

$$\tau_e \approx \frac{4}{63}\frac{M_{sat}}{M_P}\left(\frac{a}{R_{sat}}\right)^5 \frac{Q'_{sat}}{n} \ , \tag{4.2}$$

where n is the mean motion of the mutual orbit.

In Equations (4.1) and (4.2), the tidal dissipation function Q' encapsulates the physical response of a body to tides (Peale et al. 1979). Its specific usefulness is that it buries within it all the uncertainties about the tidal dissipation mechanisms. For solid bodies, this function can be related to the rigidity μ and an alternative Q-value known as the tidal dissipation parameter, $Q' = Q(1 + 19\mu/2g\rho R)$, where g is the gravitational acceleration at the surface of the body and ρ is its mean density. The dissipation function can also be defined in terms of the tidal Love number (k_L) as $Q' = 3Q/2k_L$.

4.1.1 Examples of Tidally Heated Moons

Good examples for the potential impact of tidal heating in a satellite can be found relatively close to home with the Galilean moons of Jupiter. Two such examples are shown

in Figure 4.3. Fueled by extreme tidal heating, Io (which is the innermost moon) is the most volcanically active surface in the Solar System. While Io is generally not considered to provide a habitable environment, Europa (the second innermost moon) is believed by many to possess a vast salt-water ocean underneath several kilometers of surface ice. With extremely low surface temperatures, the energy required to maintain the liquid state of the ocean is theorized to come from tidal friction, albeit at much more modest levels than those experienced by Io.

The tidal heating in Io and Europa works to circularize their orbits relative to Jupiter. Interestingly, estimates for their eccentricity damping timescales are considerably less than the age of the Solar System (see Murray and Dermott 1999, pg. 173). However, their eccentricities are noticeably not zero (0.0043 and 0.0101, respectively). This inconsistency has been explained by the observed Laplace resonance (Peale et al. 1979) between them and the satellite Ganymede. The orbital periods of the three bodies are locked in a ratio of 1:2:4, so their mutual gravitational interactions continually excite the orbits and maintain their non-zero eccentricities. This example demonstrates the need to include external gravitational influences when considering the long-term tidal evolution of nonisolated binary

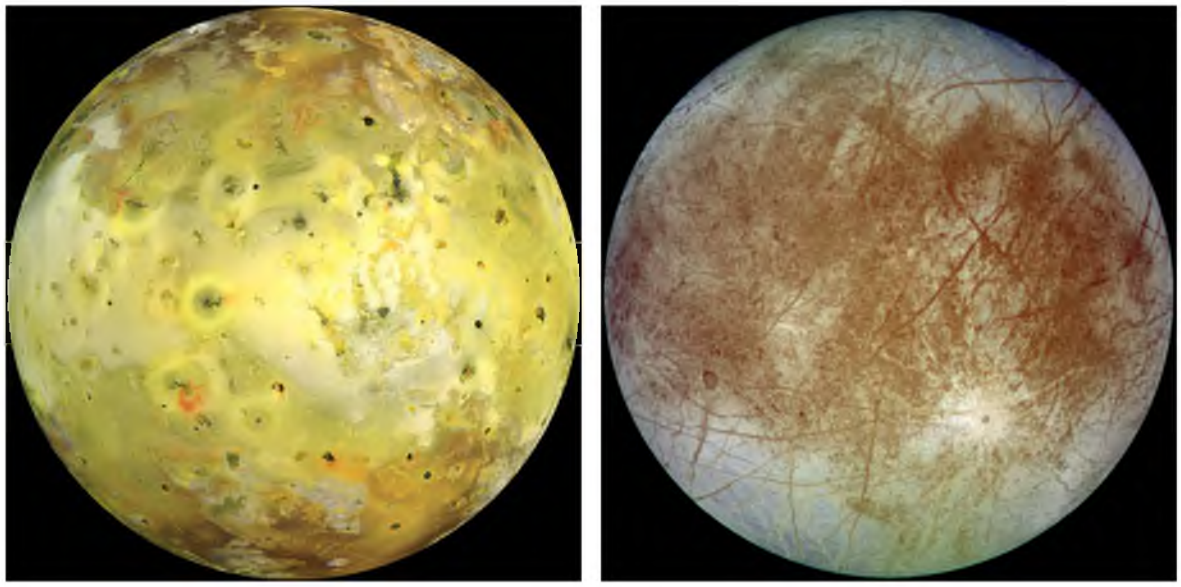

(a) (b)

Figure 4.3. Two moons of Jupiter. (a) Io, the innermost Galilean moon. Tidal heating in Io has made it the most geologically active object in the Solar System. (b) Europa, the second innermost Galilean moon. A vast salt-water ocean is believed to exist underneath the icy surface of Europa as the result of tidal heating.

systems. For planet-moon binaries in the HZ of low-mass star systems, external perturbations from the relatively close star could serve to maintain non-zero satellite eccentricity in much the same way as the orbital resonances in the Galilean moon system.

4.2 Surface Heat Flux

Equation (4.1) represents the energy being tidally dissipated by the whole of a satellite. However, to assess the surface effects of tidal heating on a potential biosphere, it is necessary to consider the heat flux through the satellite's surface. Assuming the energy eventually makes its way to the moon's surface, the surface heat flux (h) due to tides can be represented as

$$h_{conv} = H/4\pi R_{sat}^2 \ , \tag{4.3}$$

where H is the tidal heat defined by Equation (4.1). Note in the definition that a subscript is used to identify Equation (4.3) as the surface heat flux based on the conventional tidal model for H, whereas, later in this chapter, I will define another tidal heat flux based on a different tidal model.

Barnes et al. (2009) considered the effects of tidal heating in planetary bodies and offered suggestions for habitability limits on surface heat flux. Their proposed limits were based on observations of our Solar System. They first point out that the moon Io has $h = 2$ W/m^2 (from tidal heating; Spencer et al. 2000; McEwen et al. 2004), which results in intense global volcanism and a lithosphere recycling timescale on order of 10^5 years (Blaney et al. 1995; McEwen et al. 2004). Such rapid resurfacing most likely precludes the development of a biosphere so they assume that heating rates larger than this will certainly result in uninhabitable environments, and thus set $h_{max} \equiv 2$ W m^{-2}.

Tidal heating is not the only source of surface heat flow in a terrestrial body. Radiogenic heating, which comes from the radioactive decay of U, Th, and K, is an additional source for surface heat flow. Barnes et al. (2009) used this combination to also set a lower limit of $h_{min} \equiv 0.04$ W m^{-2} for the total surface heat flux of a terrestrial body by considering that internal heating can drive plate tectonics. This value was based on theoretical studies of Martian geophysics which suggest that tectonic activity ceased when the radiogenic[1] heat flux dropped below this value (Williams et al. 1997). Even though the processes which drive plate tectonics on Earth are not fully understood (Walker et al. 1981; Regenauer-Lieb et al. 2001), it is accepted that an adequate heat source is essential. The phenomenon of

[1]At the orbital distance of Mars, any contribution from tidal heating would be very low. Therefore, the total internal heating is essential equal to the radiogenic heating in this case.

plate tectonic is considered important for habitability because it drives the carbon-silicate cycle, thereby stabilizing atmospheric temperatures and CO_2 levels on timescales of $\sim 10^8$ years. For reference, the Earth's combined outward heat flow (which includes both tidal and radiogenic heat) is 0.065 W m^{-2} through the continents and 0.1 W m^{-2} through the ocean crust (Zahnle et al. 2007). However, these rates are mostly due to radiogenic heating in the Earth.

Radiogenic heating scales as the ratio of volume to area (Barnes et al. 2009). Consequently, for most cases involving closely orbiting bodies that are significantly smaller than the Earth, it is believed that tidal heating probably dominates (Jackson et al. 2008a, 2008b). As will be describe in Chapter 5, the theoretical moons considered in my study meet these conditions. Therefore, I assume that radiogenic heating is negligible and that the total surface heat flux is equal to the tidal flux described by Equation (4.21). I also adopt the heating flux limits for habitability presented above, mainly $h_{min} < h < h_{max}$.

4.3 Coupling Tidal and Gravitational Effects

Heller (2012) has suggested that low-mass stars cannot possibly host habitable moons in the stellar habitable zones because these moons must orbit their planets in close orbits to ensure Hill stability. In these close orbits, they would be subject to devastating tidal heating which would trigger a runaway greenhouse effect and make any initially water-rich moon uninhabitable. This tidal heating was supposed to be excited, partly, by stellar perturbations. While tidal processes in the planet-moon system would work to circularize the satellite orbit, the stellar gravitational interaction would force the moon's orbital eccentricity around the planet to remain non-zero. However, Heller (2012) acknowledged that his evolution model did not couple the tidal evolution with the gravitational scattering of a hypothetical satellite system. So, the extent of the gravitational influence of the star was surmised, but not actually tested. The need therefore remains to simulate the eccentricity evolution of satellites about low-mass stars with a model that consideres both N-body gravitational acceleration and tidal interactions.

Many popular and well-tested computer codes are available to simulate the gravitational (dynamical) evolution of many-bodied systems (e.g. Chambers and Migliorini 1997; Rauch and Hamilton 2002). Such codes are particularly useful for studying the long-term stability of planetary systems. These codes, however, do not include tidal interactions in their calculations. One reason for this can perhaps be demonstrated by Equation (4.1). That particular model is useful to calculate the orbit-averaged heat being dissipated in a satellite

but it does not provide the instantaneous effects on the motion of a satellite at any given point during its orbit. Such information is necessary to simultaneously consider tidal effects in an N-body gravitational simulation. Fortunately, many additional tidal evolution models exist.

Two of the most prominent tidal theories are the "constant-time-lag" (CTL) and the "constant-phase-lag" (CPL) models. Their pros and cons have been treated extensively in the literature (Ferraz-Mello et al. 2008; Efroimsky and Williams 2009; Hansen 2010; Heller et al. 2010; Heller et al. 2011; Lai 2012). An important result from these models is the calculation of strongly coupled evolution equations for the eccentricity and semimajor axis (de/dt and da/dt, respectively). Unfortunately, these results are not ideal for my particular study since they were derived by utilizing orbit-averaged simplifications. These simplifications are certainly reasonable for relatively isolated binary systems, but introduce inconsistencies for true N-body simulations which calculate accelerations at multiple points in a single orbit. Therefore, it was necessary to find a tide model that provides the accelerations from tidal interactions at any point in a satellites orbit. With this information, I could then create my own customized computer code to simulate both the tidal and dynamical evolution of massive moons in low-mass star systems.

For the purposes of my study, useful derivations were presented by Eggleton et al. (1998), whose work was based on the 'equilibrium tide' model of tidal friction (Hut 1981). Their particular interest was to consider tidal interactions between binary stars. Their model leads to a force and couple[2] on a binary orbit which are similar to those derived classically on the assumption that the tidal bulge lags the line of centers by some small time (the CTL model). They based their work on principles that (a) the rate of dissipation of energy should be a positive definite[3] function of the rate of change of the tide (as viewed in a frame which rotates with the star), and (b) the total angular momentum is conserved.

The formalism of Eggleton et al. (1998) has some advantages over other popular models. For example, its use is still appropriate at large eccentricities. Of particular interest, they derived from first principles equations governing the quadrupole tensor of a star distorted by both rotation and the presence of a companion in a possibly eccentric orbit. The quadrupole distortion produces a nondissipative acceleration $\boldsymbol{f}_{QD}$. They also found a functional form

---

[2]A 'couple' is a system of forces that produce rotation but not translation (no center-of-mass movement). This is not the same as 'torque', which can cause translational movement.

[3]In this case, a **positive definite** function refers to a real-valued, continuously differentiable function f with $f(0) = 0$ and $f(x) > 0$ for every non-zero x.

for the dissipative force of tidal friction which can then be expressed as the acceleration due to tidal fiction $\boldsymbol{f}_{TF}$. These acceleration terms are useful because they can be added directly to the orbital equation of motion for the binary:

$$\ddot{\boldsymbol{r}} = -\frac{GM\boldsymbol{r}}{r^3} + \boldsymbol{f}_{QD} + \boldsymbol{f}_{TF} \quad , \tag{4.4}$$

where r is the distance between the two bodies and M is the combined mass. This enables the evaluation of both the dynamical and tidal evolution of a binary star system.

4.4 A Self-Consistent Evolution Model for Planetary Systems

Mardling and Lin (2002) were the first to recognize that the formulations by Eggleton et al. (1998) provided a powerful method for calculating the complex evolution of not just binary stars, but planetary systems as well. Based on their formulations, Mardling and Lin (2002) presented an efficient method for calculating self-consistently the tidal, spin, and dynamical evolution of a many-bodied system. Their work had a particular emphasis on planets, yet they emphasized that the method did not assume any specific mass ratio and that their schemes were entirely general. As such, they could be applied to any system of bodies. I therefore adopted their method to explore the interaction between low-mass stars and their hypothetical planet-moon binaries in the HZ to evaluate the long-term evolution of massive moons and to find ultimate constraints on their potential for liquid surface water.

4.4.1 Equations of Motion

The method presented by Mardling and Lin (2002) for calculating orbits lends itself best to a hierarchical (Jacobi) coordinate system (see Figure 4.4). Since my primary interest involves the evolution of moons around a large planet, I use the planet's position as the initial origin of a given system. The orbit of the next closest body will be a moon, whose position is referred to the planet. The orbit of a third body is then referred to the center of mass of the planet and innermost moon, while the orbit of a fourth body is referred to the center of mass of the other three bodies. This system has the advantage that the relative orbits are simply perturbed Keplerian orbits so the osculating orbital elements are easy to calculate (see Murray and Dermott 1999).

Results for a 4-body system are shown in Figure 4.4 and in the equations listed below. However, the same setup can apply for fewer bodied systems by simply setting the extra masses to zero. Let the masses of the four objects be m_1, m_2, m_3, and m_4, with m_1 always representing a planet and m_2 always representing an innermost moon. The third mass,

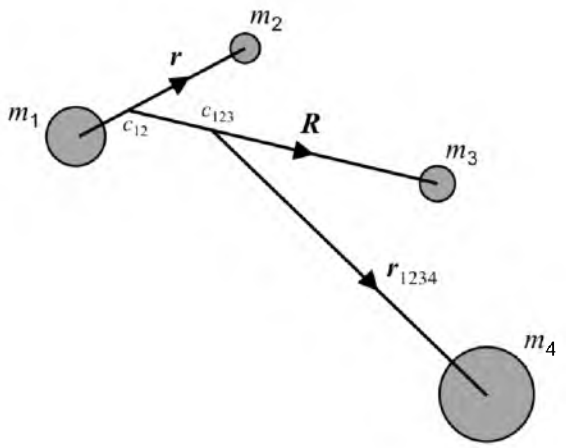

Figure 4.4. Hierarchical (Jacobi) coordinates. The symbol c_{12} denotes the center of mass of m_1 and m_2, with a similar definition for c_{123}.

m_3, will represent a central star for 3-body systems, or an outermost moon for 4-body systems. The fourth mass, m_4, will always represent a central star in a 4-body system. The relative position vectors of the three orbits ($\boldsymbol{r}$, $\boldsymbol{R}$, and $\boldsymbol{r}_{1234}$) are illustrated in Figure 4.4. Furthermore, the planet and innermost moon (being the closest pair of bodies in the system) are endowed with structure that is specified by their radii S_1 and S_2, their moments of inertia I_1 and I_2, their quadrupole apsidal motion constants (or half the appropriate Love numbers for planets with some rigidity) k_1 and k_2, and their Q-values Q_1 and Q_2. Bodies 3 and 4 are assumed to be structureless, meaning they are treated as point masses.

Given N sources of external perturbation $\boldsymbol{f}_1, \boldsymbol{f}_2, ..., \boldsymbol{f}_N$, the equation governing the relative motion of the planet and innermost moon is

$$\ddot{\boldsymbol{r}} = -\frac{G(m_1 + m_2)}{r^3}\boldsymbol{r} + \sum_{i=1}^{N} \boldsymbol{f}_i \ . \tag{4.5}$$

For a planet-moon binary, the accelerations $\boldsymbol{f}_i$ are due to the tidal and spin distortions, the tidal damping of the planet and innermost moon, the presence of a second moon or a central star, as well as the relativistic potential of the planet. Explicitly, the accelerations are as follows:

1. Those due to the third and fourth bodies (the second moon and star):

$$\boldsymbol{f}_3 = Gm_3(\boldsymbol{\beta}_{23} - \boldsymbol{\beta}_{13}) \ , \quad \boldsymbol{f}_4 = Gm_4(\boldsymbol{\beta}_{24} - \boldsymbol{\beta}_{14}) \ , \tag{4.6}$$

where $\boldsymbol{\beta}_{ij} = \boldsymbol{r}_{ij}/r_{ij}^3$, with $\boldsymbol{r}_{ij}$ representing the relative position vector from m_i to m_j.

2. The acceleration due to the quadrupole moment of body 1 (the planet), composed of its spin distortion as well as the tidal distortion produced by the presence of body 2 (the moon):

$$\boldsymbol{f}^1_{QD} = \frac{S_1^5(1+m_2/m_1)k_1}{r^4}\left\{\left[5(\boldsymbol{\Omega}_1\cdot\hat{\boldsymbol{r}})^2 - \Omega_1^2 - \frac{12Gm_2}{r^3}\right]\hat{\boldsymbol{r}} - 2(\boldsymbol{\Omega}_1\cdot\hat{\boldsymbol{r}})\boldsymbol{\Omega}_1\right\} , \tag{4.7}$$

where k_1 is the apsidal motion constant (or half the tidal Love number for bodies with some rigidity) of body 1, $\boldsymbol{\Omega}_1$ is its spin vector, and $\hat{\boldsymbol{r}}$ denotes a unit vector in the direction of $\boldsymbol{r}$. Note that for solid bodies, the Love number (k_L) can be related to the tidal dissipation "function" discussed in section 4.1 as $k_L = 2k = 3Q/2Q'$.

3. A similar expression for body 2 (with tidal distortion due to body 1).

4. The acceleration produced by the tidal damping of body 1:

$$\boldsymbol{f}^1_{TF} = -\left(\frac{6nk_1}{Q_1}\right)\left(\frac{m_2}{m_1}\right)\left(\frac{S_1}{a}\right)^5\left(\frac{a}{r}\right)^8\left[3(\hat{\boldsymbol{r}}\cdot\dot{\boldsymbol{r}})\hat{\boldsymbol{r}} + (\hat{\boldsymbol{r}}\times\dot{\boldsymbol{r}} - r\boldsymbol{\Omega}_1)\times\hat{\boldsymbol{r}}\right] , \tag{4.8}$$

where a and n are, respectively, the semimajor axis and mean motion of the mutual orbit of bodies 1 and 2.

5. A similar expression for body 2 with structure constant k_2.

6. The orbital acceleration due to the post-Newtonian potential of the binary (e.g. Kidder 1995):

$$\boldsymbol{f}_{rel} = -\frac{Gm_{12}}{r^2c^2}\left\{\left[(1+3\eta)\dot{\boldsymbol{r}}\cdot\dot{\boldsymbol{r}} - 2(2+\eta)\frac{Gm_{12}}{r} - \frac{3}{2}\eta\dot{r}^2\right]\hat{\boldsymbol{r}} - 2(2-\eta)\dot{r}\dot{\boldsymbol{r}}\right\} , \tag{4.9}$$

where $\eta = m_1m_2/m_{12}^2$ and c is the speed of light.

The accelerations given by Equations (4.7) and (4.8) are due to Eggleton et al. (1998). The vectors $\boldsymbol{r}_{ij} \equiv \boldsymbol{r}_j - \boldsymbol{r}_i$ are defined in terms of the Jacobi coordinate such that

$$\begin{aligned}
\boldsymbol{r}_1 &= -\frac{m_2}{m_{12}}\boldsymbol{r} - \frac{m_3}{m_{123}}\boldsymbol{R} - \frac{m_4}{m_{1234}}\boldsymbol{r}_{1234} ,\\
\boldsymbol{r}_2 &= \frac{m_1}{m_{12}}\boldsymbol{r} - \frac{m_3}{m_{123}}\boldsymbol{R} - \frac{m_4}{m_{1234}}\boldsymbol{r}_{1234} ,\\
\boldsymbol{r}_3 &= \frac{m_{12}}{m_{123}}\boldsymbol{R} - \frac{m_4}{m_{1234}}\boldsymbol{r}_{1234} ,\\
\boldsymbol{r}_4 &= \frac{m_{123}}{m_{1234}}\boldsymbol{r}_{1234} ,
\end{aligned} \tag{4.10}$$

where $m_{12} = m_1 + m_2$, $m_{123} = m_1 + m_2 + m_3$, etc. The equations of motion for the third and fourth bodies are

$$\ddot{\boldsymbol{R}} = \frac{Gm_{123}}{m_{12}}(-m_1\boldsymbol{\beta}_{13} - m_2\boldsymbol{\beta}_{23} + m_4\boldsymbol{\beta}_{34}) - \frac{Gm_4}{m_{12}}(m_1\boldsymbol{\beta}_{14} + m_2\boldsymbol{\beta}_{24} + m_3\boldsymbol{\beta}_{34}) \tag{4.11}$$

and

$$\ddot{\boldsymbol{r}}_{1234} = -\frac{Gm_{1234}}{m_{123}}(m_1\boldsymbol{\beta}_{14} + m_2\boldsymbol{\beta}_{24} + m_3\boldsymbol{\beta}_{34}) , \tag{4.12}$$

respectively. I should note that Equation (4.11) contains two important corrections to the equation presented by Mardling and Lin (2002).

The total angular momentum is given by

$$\boldsymbol{J}_{tot} = \mu_{12}(\boldsymbol{r} \times \dot{\boldsymbol{r}}) + \mu_{123}(\boldsymbol{R} \times \dot{\boldsymbol{R}}) + \mu_{1234}(\boldsymbol{r}_{1234} \times \dot{\boldsymbol{r}}_{1234}) + I_1\boldsymbol{\Omega}_1 + I_2\boldsymbol{\Omega}_2 \ , \tag{4.13}$$

where $\mu_{12} = m_1 m_2/m_{12}$, $\mu_{123} = m_{12}m_3/m_{123}$, and $\mu_{1234} = m_{123}m_4/m_{1234}$. The total energy is given by

$$E = \left(\frac{1}{2}\mu_{12}\dot{\boldsymbol{r}}\cdot\dot{\boldsymbol{r}} - \frac{Gm_1m_2}{r}\right) + \left(\frac{1}{2}\mu_{123}\dot{\boldsymbol{R}}\cdot\dot{\boldsymbol{R}} - \frac{Gm_{12}m_3}{R}\right) + \left(\frac{1}{2}\mu_{1234}\dot{\boldsymbol{r}}_{1234}\cdot\dot{\boldsymbol{r}}_{1234} - \frac{Gm_{123}m_4}{r_{1234}}\right) + E_{123} + E_{1234} + \mu_{12}\Phi_1 + \mu_{12}\Phi_2 + \frac{1}{2}I_1\Omega_1^2 + \frac{1}{2}I_2\Omega_2^2 \tag{4.14}$$

where

$$E_{123} = \frac{Gm_{12}m_3}{R} - \frac{Gm_1m_3}{r_{13}} - \frac{Gm_2m_3}{r_{23}} \tag{4.15}$$

and

$$E_{1234} = \frac{Gm_{123}m_4}{r_{1234}} - \frac{Gm_1m_4}{r_{14}} - \frac{Gm_2m_4}{r_{24}} - \frac{Gm_3m_4}{r_{34}} \tag{4.16}$$

are interaction energies that are small for "wide" systems, and

$$\Phi_1 = \frac{S_1^5(1+m_2/m_1)k_1}{r^3}\left[(\boldsymbol{\Omega}_1\cdot\hat{\boldsymbol{r}})^2 - \frac{1}{3}\Omega_1^2 - \frac{2Gm_2}{r^3}\right] \tag{4.17}$$

and

$$\Phi_2 = \frac{S_2^5(1+m_1/m_2)k_2}{r^3}\left[(\boldsymbol{\Omega}_2\cdot\hat{\boldsymbol{r}})^2 - \frac{1}{3}\Omega_2^2 - \frac{2Gm_1}{r^3}\right] \tag{4.18}$$

are potentials due to the quadrupole moments of the spin and tidal distortions of bodies 1 and 2, respectively. Note that Equation (4.18) also contains one minor correction to the equation provided by Mardling and Lin (2002).

Assuming that the spins of the planet and innermost moon (bodies 1 and 2) evolve solely as a result of tidal and spin torques, the evolution of the spin vector of body 1 is given by

$$I_1\dot{\boldsymbol{\Omega}}_1 = -\mu_{12}\boldsymbol{r} \times \left(\boldsymbol{f}_{QD}^1 + \boldsymbol{f}_{TF}^1\right) \ , \tag{4.19}$$

with a similar expression for body 2. The orbital elements of each orbit can be calculated from the position and velocity vectors following the procedure outlined in Murray and Dermott (1999).

The acceleration $\boldsymbol{f}_{QD}$ (Equation (4.7)) was derived from a potential and under prevailing circumstances would conserve total energy. On the other hand, the acceleration $\boldsymbol{f}_{TF}$ (Equation (4.8)) represents the effects of a slow dissipation of orbital energy by tidal friction.

The dissipation within the moon causes change in its orbital semimajor axis and spin vector, and the rate of energy loss (tidal heating) can be defined as (see Eggleton et al. (1998), Equation [39a])

$$\dot{E}_{tide} = \frac{1}{2}\frac{Gm_1m_2}{a(t)}\frac{\dot{a}}{a} + I_2\Omega_2\dot{\Omega}_2 = \mu_{12}\boldsymbol{f}_{TF}\cdot(\dot{\boldsymbol{r}} - \boldsymbol{\Omega}_2\times\boldsymbol{r}) \ . \tag{4.20}$$

With this consideration, I do not expect overall energy conservation for computational simulations following this method. However, I do still expect conservation of total angular momentum.

Since Equation (4.20) represents the tidal heating in a satellite according to this tidal model, the surface heat flux in the satellite can be defined as

$$h = \dot{E}_{tide}/4\pi S_2^2 \ , \tag{4.21}$$

where S_2 represents the satellite's radius, following the notation used above.

4.4.2 The Simulation Code

The previous subsection listed clearly defined equations of motion for a multibodied system of up to four bodies. With these equations I was able to create my own computer program that had the ability to simultaneously consider both dynamical and tidal effects, and with it, I could simulate exomoon tidal evolution in low-mass star systems. The program code was written in C++[4] and a Bulirsch-Stoer integrator with an adaptive timestep (Press et al. 2002) was used to integrate the equations of motion.

The robustness of the code was evaluated by tracking the relative error in total angular momentum, where the relative error is defined as $(L_{out} - L_{in})/L_{in}$. The size of the relative error could be controlled by adjusting an absolute tolerance parameter. However, as is often the case with direct orbit integrators, the problem of systematic errors in the semimajor axis existed. Nevertheless, the tolerance was set to allow a maximum error of 10^{-9} per step for the total angular momentum. The algorithm efficiency was such that this level of tolerance resulted in about seven integration steps per orbit, for the smallest orbit (which was always the innermost moon).

Relative errors in total energy ($(E_{out} - E_{in})/E_{in}$) were also tracked, which a typical N-body code would also consider as a measure of robustness. However, for my systems, the conservation of mechanical energy was not expected. For this reason, I did not include energy conservation as a baseline for performance in simulations involving tidal dissipation.

[4]C++ is a compiled, object-oriented programing language.

In this regard, built into the code was the ability to turn off tidal effects in which case the program could be used for strictly dynamical considerations.

A primary drawback to directly integrating orbital motion is the extensive computational processing times required to simulate long-term behavior. With my particular evolution model, the situation is compounded by extra calculations for tidal interactions. Early tests for code efficiency indicated a processing time of roughly two days per million years of simulated time. This time estimate was based on simulations involving two extended objects and a third point mass object. Since the integration timestep is effectively controlled by the object with the shortest orbital period, the exact processing times varied significantly between wide orbit and short orbit satellites. Of course, the required runtime also depends on the number of objects being integrated. In which case, 4-body simulations (2 extended bodies, 2 point mass bodies) required about 3 days per million years of simulated time. From these numbers, I predicted an ability to simulate satellite systems with timescales on the order of 10^6 to 10^7 years. However, careful consideration would be required to properly explore any parameter space in order to conserve limited computational resources.

This subsection provides a precise explanation for the creation of my simulation program. It does not, however, satisfactorily convey the extensive time commitment that was required for its completion. This is highlighted only to emphasize its importance in this study and its potential for future study. As previously mentioned, a publicly accessible simulation program was not available that could simultaneously evaluate the tidal, spin, and dynamical evolution of a many-bodied system. An important advantage to the program is that it is not restricted by any specific mass ratio for the considered bodies. While its current use in this dissertation is applied to the evolution of satellite systems, the code is not limited to moon studies. Investigations can also include tidal evolution for multiplanet systems or even planets in a binary star system. A future goal will be to make this program publicly available as a viable option for tidal evolution simulations.

CHAPTER 5

SIMULATING EXOMOON EVOLUTION: SETUP

5.1 System Architectures and Physical Properties

As part of my investigation into the evolution of exomoons around giant planets in the HZ of low-mass stars, I evaluated three different system architectures. The first involved a minimal 2-body system consisting of only a planet and a moon; the second was a 3-body system of one planet, one moon, and a central star; and lastly, a 4-body system contained one planet, two moons, and a central star. For each system, the planet and innermost moon were given structure while any additional bodies were treated as point masses.

My intent with the 2-body systems was to evaluate tidal heating for an isolated planet-moon binary. These systems would represent what the tidal evolution would be without any external perturbations. The purpose of the 3-body systems was to consider the influence of the star on the orbit of a moon and to evaluate its ability to continually excite a non-zero eccentricity (and thus maintain a non-zero tidal heating rate). For each 3-body simulation, a corresponding 2-body simulation was performed for the same planet-moon binary. Comparing the two simulations would provide a baseline for determining the stellar contribution to a moon's long-term evolution. My purpose with the 4-body systems was to evaluate the potential for additional eccentricity excitation under resonant conditions with a second massive moon, similar to the resonant behavior of the Galilean moons.

Two specific reasons motivated my choice to give extended structure only to the planet and innermost moon: (1) Tidal heating is strongly dependent on distance (refer to Equation (4.1)). The planet and innermost moon will remain the closest pair of bodies in any system; hence, the heating rates due to their mutual interaction will be the most significant. (2) The number of required calculations per integration timestep is substantially greater for extended bodies than for point mass bodies. Therefore, the required computation time greatly increases with each additional extended body. Since a single simulation with two extended bodies can already require a few hundred hours to process, I was better able to

utilize my limited computational resources by restricting the number of extending bodies in each simulation.

Although thousands of extrasolar planets have been detected, very little information is known about their internal structure and composition. Recognizing that limits for tidal dissipation depend critically on these properties, without this information, objects in the solar system provide the best guide for hypothesizing the internal structure and dynamics of extrasolar bodies. For this reason, I used known examples from our Solar System to model my hypothetical extrasolar satellite systems.

5.1.1 The Exomoon Model

Formation models for massive exomoons show reasonable support for moons with roughly the mass of Mars. With a mass of about 0.11 $M_{\oplus}$, a Mars-like exomoon is near the currently proposed detection limit of ~0.2 $M_{\oplus}$ and also lies in the preferred mass regime discussed in subsection 2.5.1 for habitable exomoons. For these reasons, I chose to model the physical structure of my hypothetical exomoons after the Solar System planet Mars.

The specific physical properties used in my moon model are shown in Table 5.1. The bond albedo represents current estimates for Mars. Since I assume habitable exomoons, a more appropriate choice may be an Earth-like value ($\alpha = 0.3$). Bond albedos are not used in the evolution simulations; rather, they are utilized afterwards to estimate the global flux F_{glob} received by the moon (refer to subsection 2.5.2). Habitability considerations from the global flux are made in comparison to the critical flux for a runaway greenhouse F_{RG} defined in Equation (2.6). For a Mars-mass exomoon, the critical flux is $F_{RG} = 269\ W/m^2$. For now, I will continue to use the lower bond albedo of Mars, keeping in mind that it will produce slightly higher estimates of F_{glob}. If the simulation results show a global flux

Table 5.1. Physical properties for a hypothetical Mars-like exomoon. The parameters A, B and C are the principal moments of inertia.

Parameter	**Value**
Mass (M)	0.107 $M_{\oplus}$
Mean Radius (R)	0.532 $R_{\oplus}$
Love Number (k_L)	0.16
Bond Albedo (α)	0.250
Dissipation Factor (Q)	80
C/MR^2	0.3662
C/A	1.005741
C/B	1.005044

greater than 269 W/m^2, I will also consider an Earth-like bond albedo.

The Love number and dissipation factor are also based on recent estimates for Mars (Yoder et al. 2003; Bills et al. 2005; Lainey et al. 2007; Konopliv et al. 2011; Nimmo and Faul 2013). Their specific values represent the higher dissipation range of the estimates. This choice produces a slightly faster tidal evolution and also tests the extent of the gravitational influence of the star against a slightly higher rate of energy loss that continually works to circularize the orbit of the moon. The principal moments of inertia are also based on recent estimates for the planet Mars (Bouquillon and Souchay 1999) and represent a tri-axial ellipsoid for the overall shape of the body. I realize that a Mars-like exomoon orbiting close to a giant planet would undoubtedly develop a different bodily shape than the current shape of Mars. This choice reflects the purpose it serves during the simulations. If I assume a constant moment of inertia, then the principal moments only become important in calculating the evolution of the moon's spin vector (see Equation (4.19)). To minimize this importance, I set the moon's initial obliquity to zero and started each simulation with the moon already in synchronous rotation about the planet. Under these conditions, there is minimal change to the moon's spin vector and the given triaxial shape is effective at keeping the moon tidally locked to the planet as its orbit slowly evolves from tidal interactions. So in that sense, another choice in shape could have equally served the same purpose.

I only considered prograde motion for the moon relative to the spin of the planet. As mentioned in subsection 2.3.1, moons are expected to be roughly coplanar with the planetary orbit; therefore, I use an initial inclination of zero for all moons. In keeping with my use of local examples, I modeled the moon's orbital distance (semimajor axis) after known satellite orbits around giant planets in the Solar System. In terms of their host planet's radius (R_P), the large solar system moons Io, Europa, Ganymede, Titan, and Callisto happen to already posses roughly evenly spaced intervals for orbital distance (5.9, 9.6, 15.3, 21.0, and 26.9 R_P, respectively). In reference to this natural spacing, when discussing orbital distances of a moon, I will often refer to them as Io-like or Europa-like orbits, etc.

The eccentricity of the moon's orbit relative to the planet is an important parameter to explore due to its connection with the tidal heat ($H \propto e^2$). Considering stability constraints, and assuming my satellite systems are not newly formed, I would not expect high eccentricities for stable exomoon orbits. For this reason, I use an initial eccentricity of 0.1 for my 2-body and 3-body models. I then monitor the moon's evolution as the tidal dissipation works to circularize the orbit. In my 4-body simulations, which involves two Mars-like moons, even a moderate eccentricity of 0.1 can easily lead to chaos in these

tightly packed systems. As a result, in these systems I start the moons on circular orbits and observe as the eccentricities become excited to non-zero values.

5.1.2 The Planet Models

Not surprising, moon formation theories suggest that massive terrestrial moons will most likely be found around giant planets. With this consideration, I chose to model my hypothetical planet after the two most massive planets in our Solar System, specifically, planets Jupiter and Saturn. The physical properties used in my planet models are shown in Table 5.2. The bond albedos, Love numbers, and dissipation factors are based on current estimates for these two Solar System planets (Gavrilov and Zharkov 1977; Hanel et al. 1981; Hanel et al. 1983; Meyer and Wisdom 2007; Lainey et al. 2009). There is actually much debate in the literature regarding the dissipation factor Q for the two planets. I specifically chose values which represent more substantial heating in the planets, similar to my choice for the Mars-like moons.

The normalized moments of inertia were also based on recent estimates (Helled 2011; Helled et al. 2011) and the three equal principal moments imply a spherical shape for the planet. I realize this specific choice for the shape may be unrealistic, and that a planet orbiting close to a star with a massive moon is unlikely to maintain a truly spherical shape. However, similar to my argument for the shape of the moon, the planet's exact shape is not particularly important for the purposes of my simulation. With spherical bodies, I also do not match the exact shapes of the solar system planets as they are currently comprised. For example, I ignore their oblateness that results from their short rotation periods (about 10 hrs for Jupiter, 11 hrs for Saturn). I start each planet with zero obliquity and an already synchronous rotation relative to its orbit around the central star, which results in a rotation

Table 5.2. Physical properties for hypothetical giant exoplanets. The planet shape is assumed spherical with principal moments of inertia $A = B = C$.

Jupiter-like	
Parameter	**Value**
Mass (M)	318 $M_\oplus$
Mean Radius (R)	11.0 $R_\oplus$
Bond Albedo (α)	0.343
Love Number (k_L)	0.38
Dissipation Factor (Q)	35000
C/MR^2	0.263

Saturn-like	
Parameter	**Value**
Mass (M)	95.2 $M_\oplus$
Mean Radius (R)	9.14 $R_\oplus$
Bond Albedo (α)	0.342
Love Number (k_L)	0.341
Dissipation Factor (Q)	18000
C/MR^2	0.21

period that ranges from about 20 to 120 days. This setup is consistent with the prediction that planets in the HZ of low-mass stars will most likely be tidally locked to the star.

Table 3.1 contains a list of planets that are believed to orbit in the HZ of low-mass stars. Of the 6 planets listed in the table, 4 can be regarded as giant planets. One in particular corresponds nicely with the Saturn model. The planet HIP 57050 b has a mass of 94.6 $M_{\oplus}$, which is approximately equal to the mass of Saturn. Since no other information is available about the physical properties of these giant planets, only direct comparisons relating to their masses can be made. None of the red dwarf HZ candidates match directly with Jupiter, but two have masses double that of Jupiter. This at least confirms the plausibility for the existence of Jupiter mass planets in the HZ of red dwarf stars.

Although I used two different planet models, each simulated system consisted of only one planet. For the 3-body and 4-body systems, each planet started with a circular orbit relative to the star as well as an orbital distance (semimajor axis) inside the stellar HZ. Due to my continual efforts to conserve computational processing time, I limited my exploration of the HZ to just two specific orbital distances per planetary system. The first location was simply in the center of the HZ for a given star mass, otherwise defined as

$$a_{center} = (\text{inner edge} + \text{outer edge})/2 \ , \tag{5.1}$$

where the inner and outer edges are determined by Equations (1.3) and (1.4). This particular location was to serve as a reference point for the next round of simulations. If most of the hypothetical satellites already experienced intense tidal heating at the center, then the next location should be further out in the zone. On the other hand, if the surface heating rates were below the proposed maximum for habitability ($h_{max} = 2\ W/m^2$), then I would move inward for the next round. As will be shown in Chapter 6, after simulating satellite systems in the center of the HZ, it became clear that the second round of simulations should involve the inner HZ.

While the innermost edge was a reasonable option to explore, an Earth-equivalent distance had obvious attraction, especially considering that my definition of the solar HZ already had the Earth very near the inner boundary. By 'Earth-equivalent' I refer to the Earth's relative position in the Sun's HZ as compared to the total width of the zone. I explained in subsection 1.3.1 that my use of conservative estimates places the inner edge of the Sun's HZ at 0.99 AU and the outer edge at 1.67 AU. With these boundaries, I define Earth's relative location in the solar HZ as

$$d_{rel} = 1 - (1.67AU - 1AU)/(1.67AU - 0.99AU) = 0.0147 \ . \tag{5.2}$$

For a given star, I use this relative location and the width of its HZ to define a planet's Earth-equivalent orbital distance as

$$a_{eq} = \text{inner edge} + (\text{outer edge} - \text{inner edge}) * d_{rel} \ . \tag{5.3}$$

5.1.3 The Star Models

Information relating to a star's mass, radius, and effective temperature is required to calculate its circumstellar HZ (see subsection 1.3.1 and subsection 1.3.3) and to estimate the global flux received by a moon. In my simulations, the stars are treated as point masses, and so the stellar mass is the only physical characteristic used in the actual simulation of a system. In my study, I considered a star mass range from 0.075 $M_{\odot}$ to 0.6 $M_{\odot}$. This particular range covers the entire red dwarf (low-mass) star regime (~0.075 $M_{\odot}$ to ~0.5 $M_{\odot}$) which is comprised of mostly M spectral type stars. The small extension above red dwarf masses involves late K type stars.

5.2 Estimates for Eccentricity Damping Timescales

Following Equation (4.2), I can estimate the eccentricity damping timescales (τ_e) for my hypothetical satellite systems. As previously described, these systems are comprised of a Mars-like moon orbiting a giant planet. The timescales are summarized in Table 5.3 for the two planet models and for the various moon orbital distances considered.

It was fortunate to see timescales around one million years since integration times of order 10^6 or even 10^7 years represent achievable computational processing times. I concluded that I would be able to simulate a complete tidal evolution for moons with Io-like and Europa-like orbital distances. Unfortunately, it was unlikely that I could show any significant evolution for the wider orbits. It should be noted that Equation (4.2) was derived from a two body calculation. As such, it does not take into account any perturbing effects from additional bodies. Since the degree to which the central star would influence a moon's orbit was unknown, I decided to include the wider orbits in my considerations for 3-body and 4-body systems.

5.3 2-body Orbital Evolution: Tides versus No-Tides

After running several initial 2-body simulations which considered both tidal and dynamical evolution, I did indeed find that orbital energy dissipated through tidal heat resulted in the slow decay of the moon's eccentricity and caused a corresponding shift in its semimajor axis. The time required for the eccentricity (and thus the tidal heating) to reach a steady

Table 5.3. Eccentricity damping timescale estimates for a Mars-like moon at different orbital distances.

Jupiter-like Host Planet	
Orbital Distance	τ_e **(years)**
Io-like ($5.9 R_{Jupiter}$)	4 x 10^5
Europa-like ($9.6 R_{Jupiter}$)	9 x 10^6
Ganymede-like ($15.3 R_{Jupiter}$)	2 x 10^8
Titan-like ($21.0 R_{Jupiter}$)	1 x 10^9
Callisto-like ($26.9 R_{Jupiter}$)	7 x 10^9

Saturn-like Host Planet	
Orbital Distance	τ_e **(years)**
Io-like ($5.9 R_{Saturn}$)	6 x 10^5
Europa-like ($9.6 R_{Saturn}$)	1 x 10^7
Ganymede-like ($15.3 R_{Saturn}$)	3 x 10^8
Titan-like ($21.0 R_{Saturn}$)	2 x 10^9
Callisto-like ($26.9 R_{Saturn}$)	1 x 10^{10}

minimum varied greatly depending on the moon's initial orbital distance; however, several million years of simulated time were necessary for even the fastest evolution rate.

In my simulations, the decay of the semimajor axis and eccentricity are in contrast to a strictly dynamical simulation in which both angular momentum and energy conservation require more constant values for those orbital elements. Figures 5.1 and 5.2 demonstrate some typical evolutions for a Mars-like moon around a Jupiter-like planet. Each plot shows results for two separate simulations, one which included tidal interactions (red curves) and another that did not (black curves). As expected, these plots show no significant change to the orbits without tidal interactions. When tidal interactions are included, the rate of change depends strongly on the moon's orbital distance, as expected.

Figures 5.3 and 5.4 are similar to the previous figures, except they involve a Saturn-like host planet. The satellite evolutions are similar to those with a Jupiter-like host planet, with one major exception. Note the difference in scaling used for the ordinate axes of the semimajor axis plots (the plots on the right). In particular, a comparison of 5.1(a) and 5.3(a) indicate that an Io-like moon orbit around Saturn experienced a significantly greater change in semimajor axis than the Io-like moon orbit around Jupiter. The explanation for this is related to the different radii of the two planets. A moon's initial orbital distance is defined by R_P, the planet radius. For example, an 'Io-like' orbit is 5.9 R_P. Because of Saturn's smaller radius, a moon with an Io-like orbital distance is actually closer to the

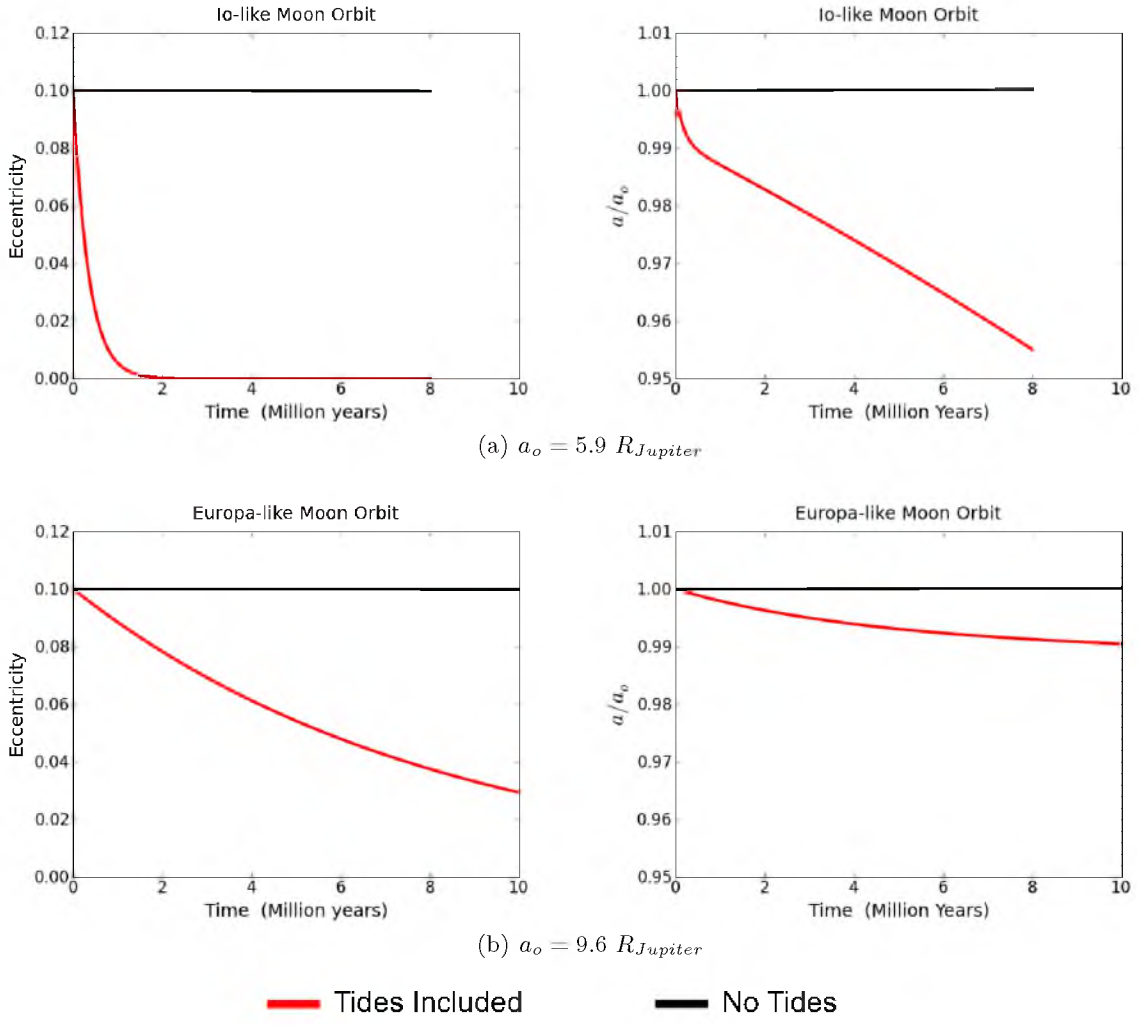

(a) $a_o = 5.9\ R_{Jupiter}$

(b) $a_o = 9.6\ R_{Jupiter}$

Figure 5.1. Orbital evolution comparisons for shorter moon orbital distances. The systems included a Jupiter-like planet and a Mars-like moon (2-body system). The two curves in each plot represent two separate simulations, one with tidal interactions and one without.

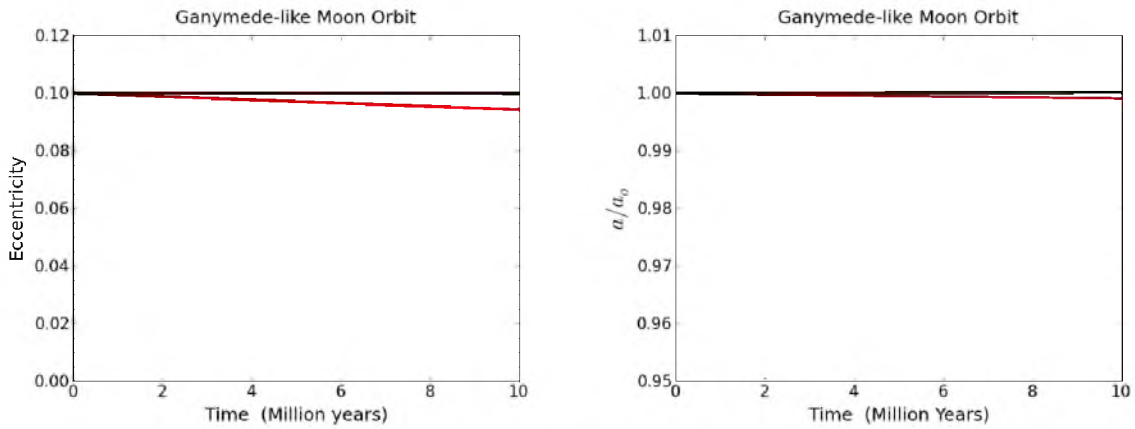

(a) $a_o = 15.3\ R_{Jupiter}$

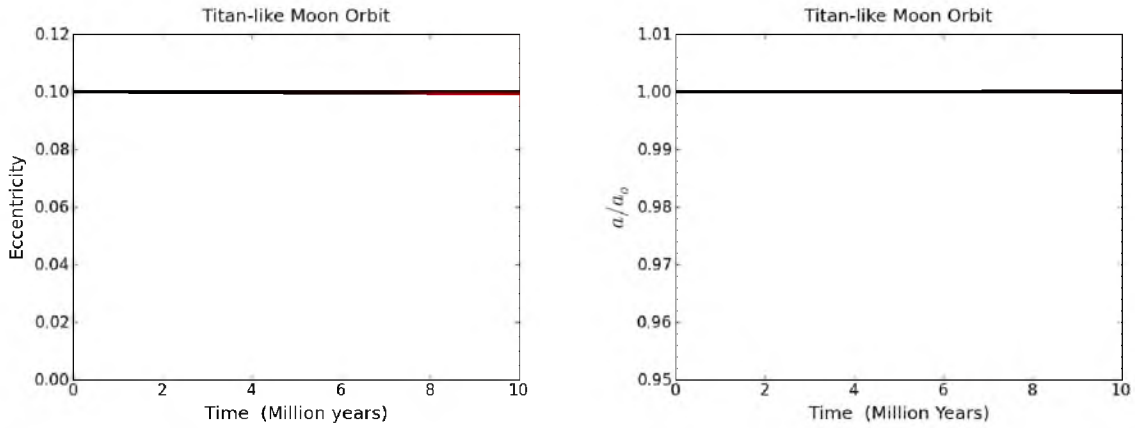

(b) $a_o = 21.0\ R_{Jupiter}$

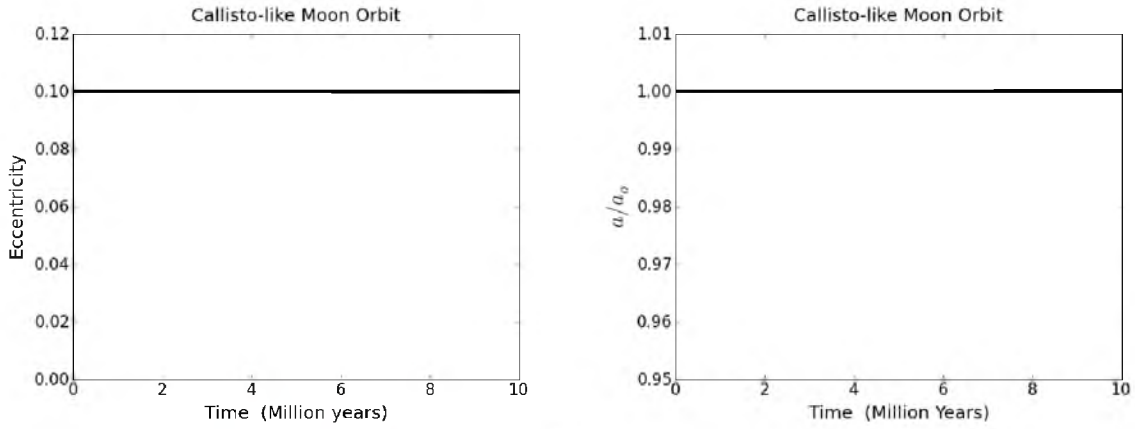

(c) $a_o = 26.9\ R_{Jupiter}$

Figure 5.2. A continuation of Figure 5.1 for wider moon orbital distances. The 2-body systems included a Jupiter-like planet.

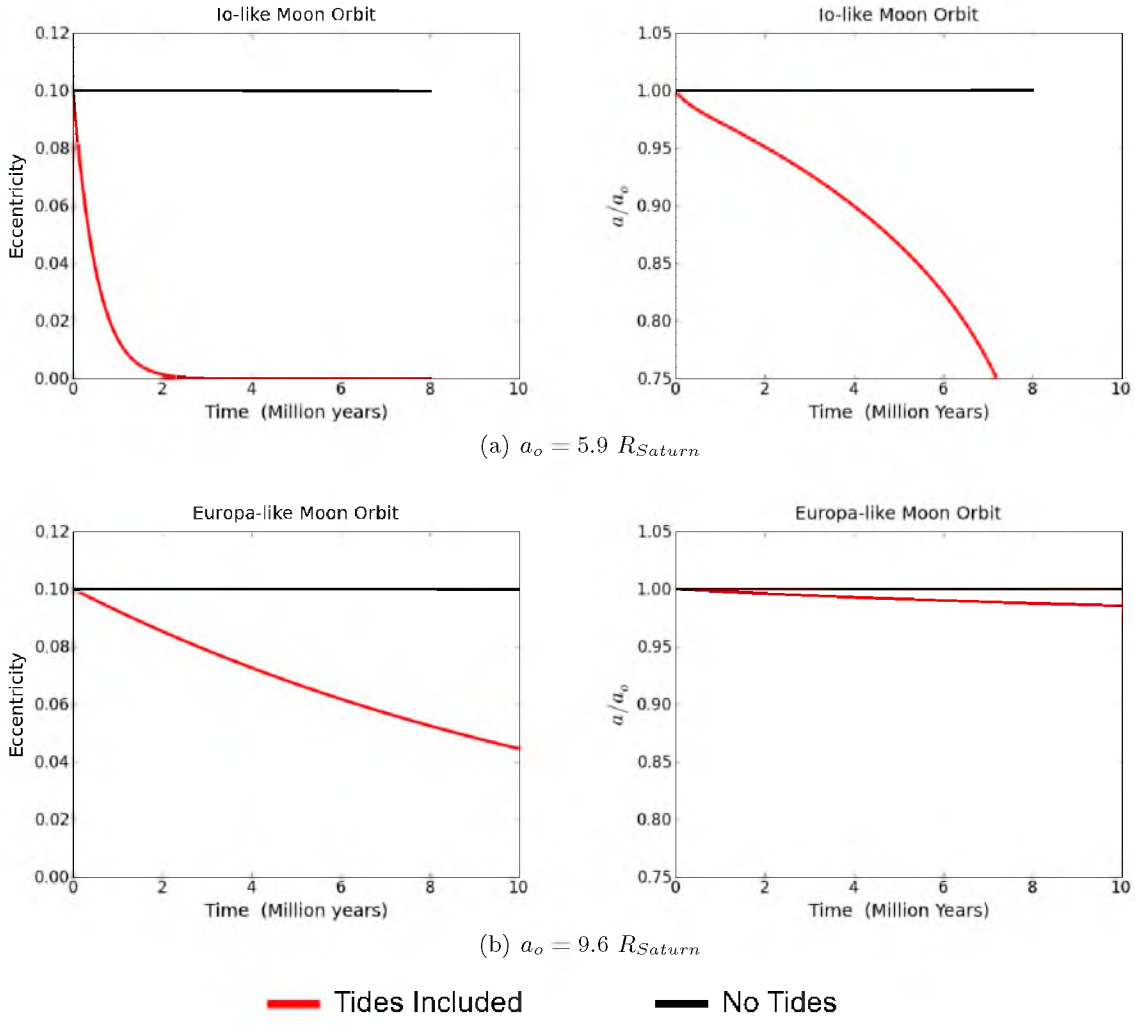

(a) $a_o = 5.9\ R_{Saturn}$

(b) $a_o = 9.6\ R_{Saturn}$

Figure 5.3. Orbital evolution comparisons for shorter moon orbital distances involving a Saturn-like planet and a Mars-like moon (2-body system). The two curves in each plot represent two separate simulations, one with tidal interactions and one without.

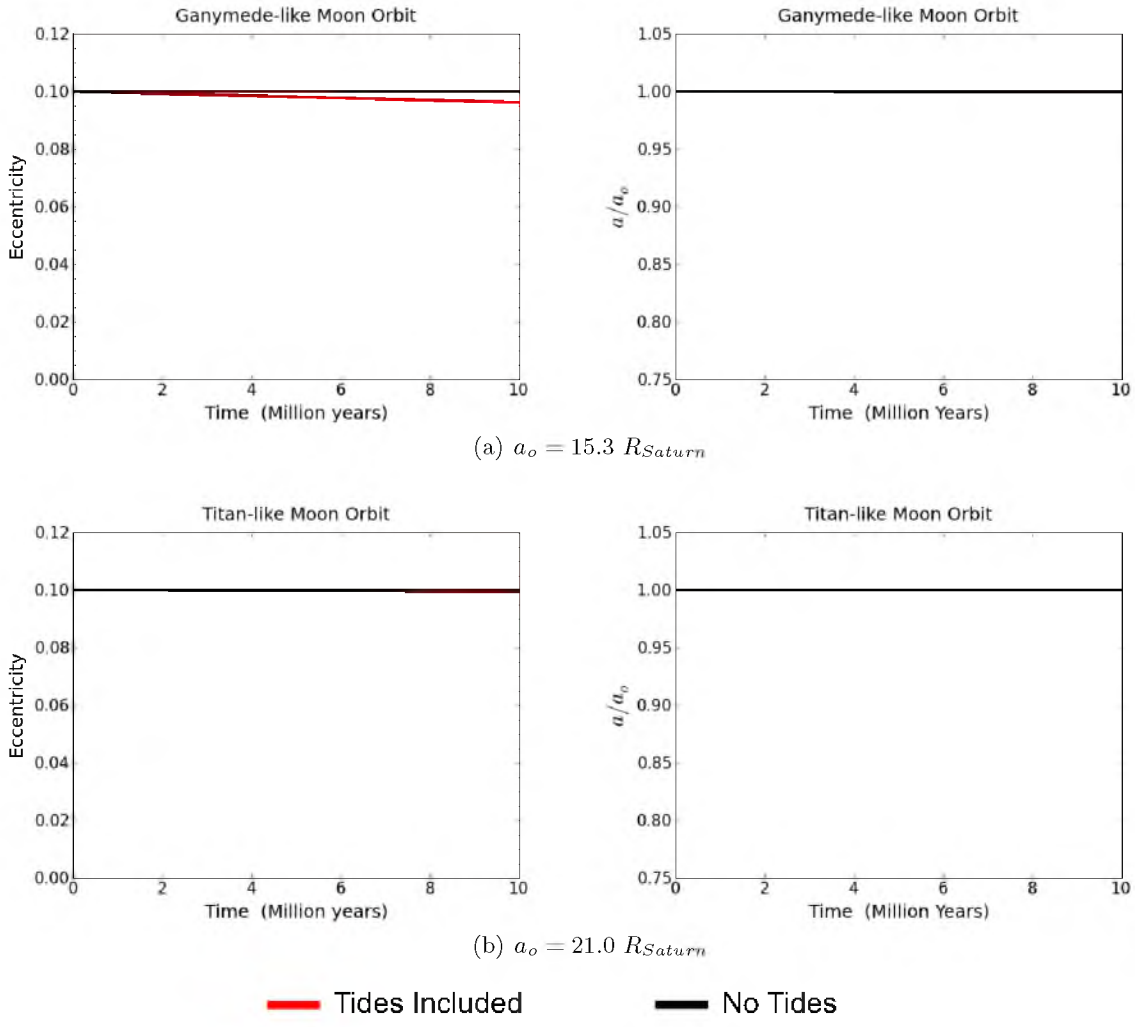

(a) $a_o = 15.3\ R_{Saturn}$

(b) $a_o = 21.0\ R_{Saturn}$

Figure 5.4. A continuation of Figure 5.3 for wider moon orbital distances. The 2-body systems involved a Saturn-like planet.

planet than an Io-like orbit around Jupiter, since 5.9 $R_{Saturn} < 5.9\ R_{Jupiter}$. Following this formulation for the orbital distances, identical moons around each planet will experience different heating rates. In a similar regard, the planets have different internal heating rates due to their unique physical properties.

While different tidal heating rates might explain part of the discrepancy in semimajor axis evolution between Saturn-like and Jupiter-like host planets, it cannot possibly account for all of it. The eccentricity plot in Figure 5.3(a) shows that the orbit was circularized after 3 million years at which point the tidal heating would cease. Therefore, any change in the semimajor axis after 3 million years can no longer be attributed to tidal dissipation. However, after this time, the orbital distance continues to decrease and its rate of change increases. This same behavior is only marginally noticeable for Europa-like orbits and is insignificant in the wider orbits.

The explanation for the persistent evolution of the moon's semimajor axis relates to torques that result from both spin and tidal distortions in the planet and moon. In my simulation code, the effects of torque on the spin of a body were represented by Equation (4.19), with the corresponding accelerations defined in Equations (4.7) and (4.8). As a result, the continued evolution of the semimajor axis does not reflect a continued dissipation of orbital energy, but rather, the conservation of total angular momentum. The distortion torques act to keep the moon tidally locked to the planet, even as its orbit decays from tidal dissipation. Once the orbit is circularized and the dissipation ceases, the continuing effects of the torques will depend on the moon's distance from the planet, as well as the relative spin rates of the two bodies. Since I assume the planet to be tidally locked to a central star, their corresponding spin rates are rather slow in comparison to the orbital period of the moon. In this particular case, the rotation period of the planet was about 100 days, compared to just a couple days for the moon. As such, a planet's tidal bulge will lag behind the imaginary line connecting its center to that of the moon. The result will be a small increase in the planet's spin rate which must be countered by a decrease in the moon's semimajor axis in order to conserve total angular momentum. This decrease will, in turn, increase the moon's spin as it synchronizes with its orbital period. This leads to another decrease in orbital distance, causing the cycle to repeat itself. This description is simply a more detailed discussion of the potential for inward spiraling already mentioned in previous sections. Note that the situation is reversed for the Earth and its moon (the Moon) which involves an outward spiraling.

The effects of distortion torques and the consequences of angular momentum conserva-

tion serve well in explaining why the continued semimajor axis evolution is much more significant for Io-like orbits versus wider orbits, as well as explaining the discrepancy between Saturn-like host planets and Jupiter-like host planets. The connection is simply the different distances involved between the planet and moon. Io-like orbits are the shortest considered orbits and the Saturn-like hosts have the shortest Io-like orbits (as explained above). Therefore, the torques and corresponding accelerations will be greater in these systems than in any other system. In fact, the increasing rate of change for the moon's semimajor axis suggests that the moon will completely spiral into the Saturn-like planet in another few million years. Using the corresponding slope in Figure 5.1(a) for the Jupiter host system, I can estimate a total lifetime of roughly 200 million years for its moon under the current conditions. Considering these are just preliminary results for an isolated planet-moon binary, it will be necessary to monitor the long-term behavior of Io-like moon orbits in my 3-body and 4-body simulations.

A graphical representation of the spin evolution for the Io-like systems is provided in Figure 5.5, with the corresponding semimajor axis evolution already shown in Figures 5.1(a) and 5.3(a). The solid blue line in Figure 5.5(a) is the best representation for how the spin rate of change has an inverse behavior to the rate of change in the semimajor axis. Comparing the planet spin rates (the dashed lines), the Saturn-like planet had a noticeable increase relative to the Jupiter-like host; however, the increase appears somewhat exaggerated by the log scaling for the ordinate axis. This difference is explained by the unequal distances for the otherwise identical Mars-like moons as well as the unequal moments of inertia for the planets. The short satellite orbit around Saturn combined with its lower moment of inertia leads to the small, but noticeable increase in spin. This small increase, however, has led to the moon almost doubling its initial spin rate, whereas the wider orbit and more massive Jupiter host planet caused very little change for both the moon and planet in this system.

The tidally locked state of the moons throughout the simulated time are demonstrated in Figure 5.5(b). A perfectly synchronized spin rate would produce a value of 1 for the ratio between spin magnitude and mean orbital motion. Notice that the ratio is not exactly 1 for the first million years (although the difference is small). This discrepancy can be explained by the shapes of the orbit during that time. Referring to the eccentricities plotted in Figures 5.1(a) and 5.3(a), the spin cannot completely synchronize with the orbital period until the eccentricity approaches zero. This fact has lead some authors to make a specific distinctions between 'synchronous' orbits and 'tidal locking'; however, such distinction is not necessary

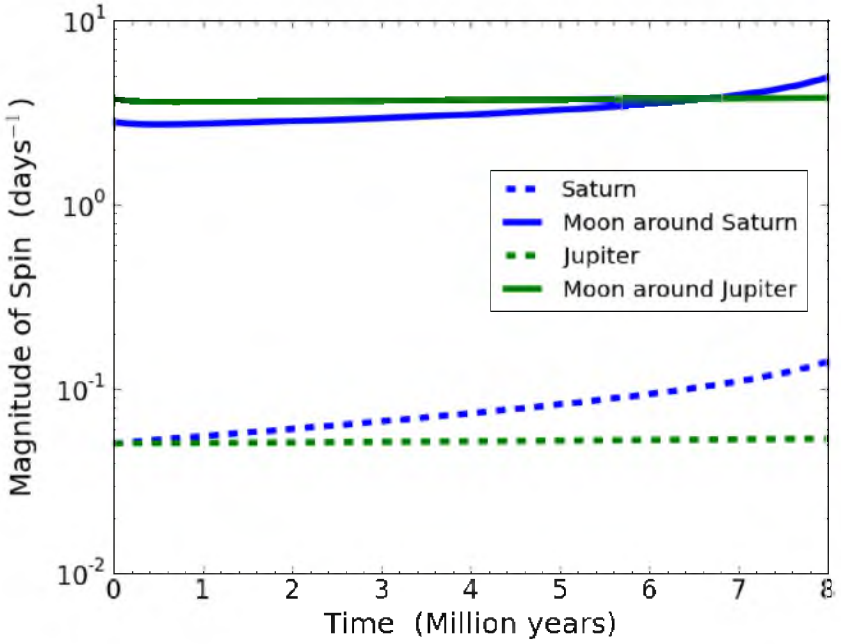

(a)

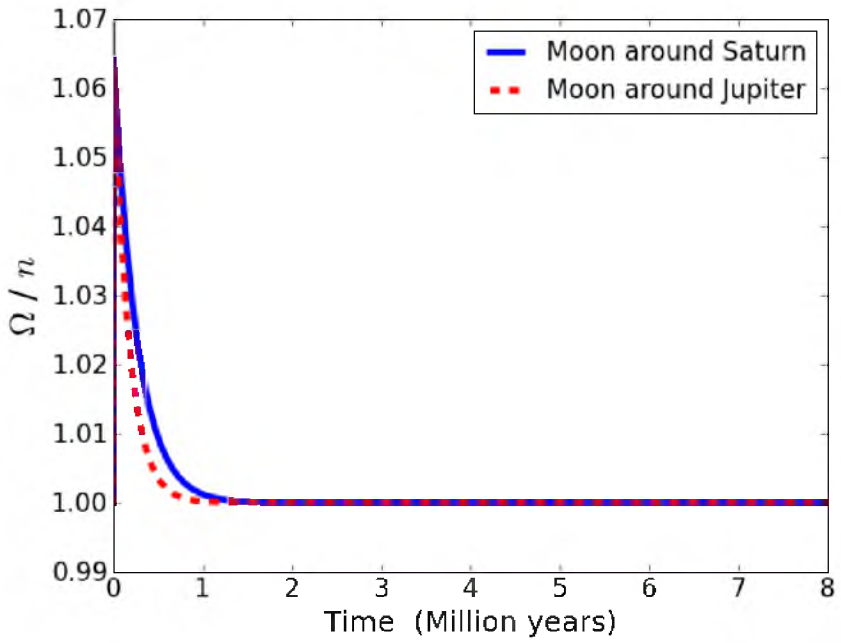

(b)

Figure 5.5. Spin evolution for Io-like orbits. (**a**) Two binary systems are represented. The blue lines comprise a system with a Jupiter-like host planet, the green lines involved a Saturn-like host. All bodies are represented, referring to both the planet and moon in each system. (**b**) Ratio of spin magnitude (Ω) and mean motion (n) for the moons represented in plot a.

in this study.

In order to verify that the decrease in satellite semimajor axis was indeed caused by a lagging tidal bulge in the planet, I repeated the simulation for an Io-like orbit around Saturn with a much faster spin rate for the planet. I used a rotation period of 11 hours. In this way, the tidal bulge would lead the motion of the moon, which should cause an outward spiral, and a decrease in the moon's rotation rate. The results are shown in Figure 5.6. It is clear by the increasing semimajor axis that the moon slowly moved away from the planet. As expected, the moon's spin rate also decreased during this time. In this case, the planet's spin was so fast that its corresponding change is not obvious from the figure as it was for the slow rotation model. This example demonstrates the consequences of assuming a tidally locked rotation for the planet relative to the star. However, since the assumption is supported by theory, I will continue to use it in the creation of my 3-body and 4-body systems.

As a final observation, one similarity between the Jupiter and Saturn-like systems is that for Ganymede-like orbits and greater, there is little change in the orbital elements over a period of 10 million years. This was not particularly surprising as the result was predicted from the damping timescales. At these wider orbits, the dissipation rate would simply be much lower for a given eccentricity due to the $a^{-15/2}$ dependence of tidal heating. On the other hand, a central star's potential for exciting the eccentricity is still untested. I continued to include the wider orbits in my 3-body analysis.

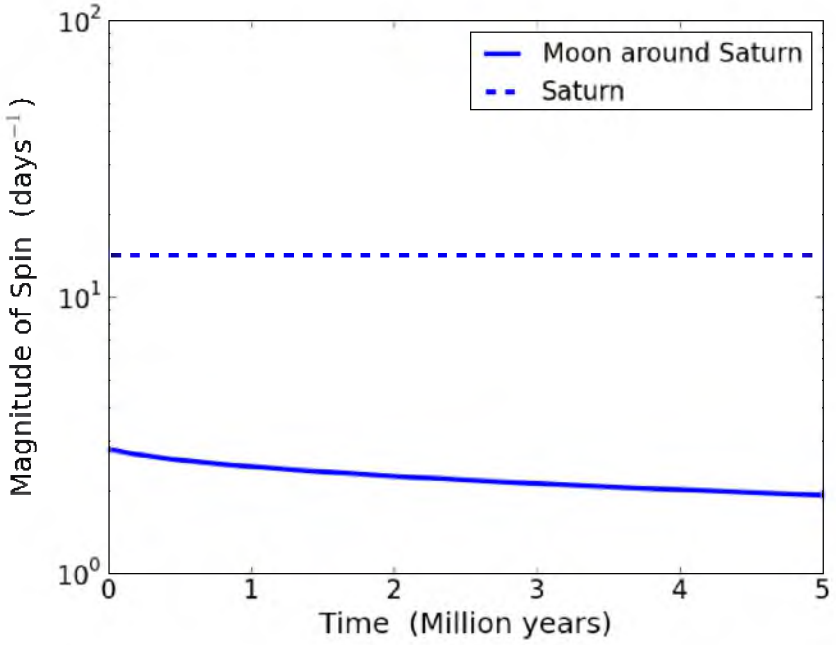

(a)

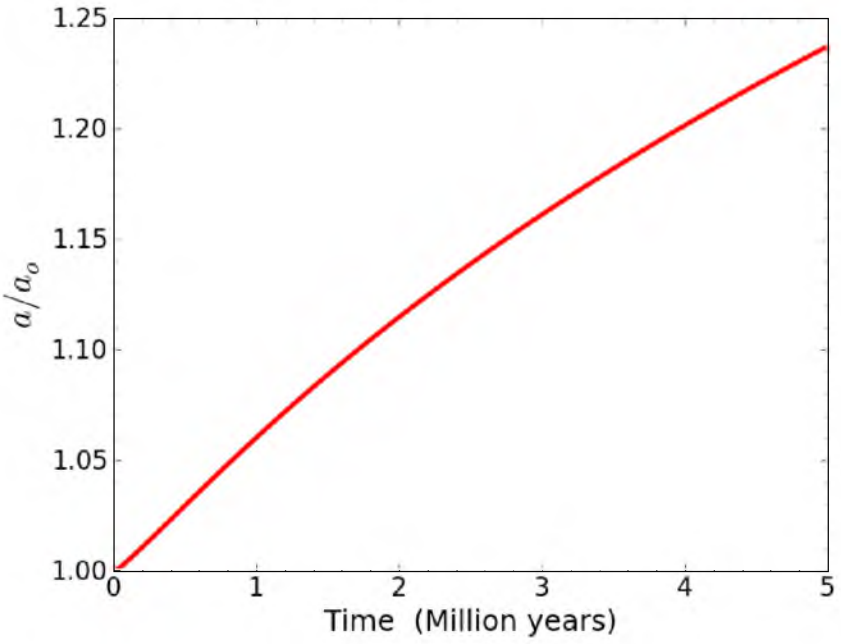

(b)

Figure 5.6. Evolution for an Io-like moon orbit around a fast spinning Saturn-like host. (**a**) Spin evolution for the satellite and host planet. (**b**) Semimajor axis evolution for the satellite.

CHAPTER 6

3-BODY SIMULATIONS

Specific details for the architecture and physical properties of my 3-body model were provided in section 5.1. These systems consist of one planet, a moon, and a star. The planet was either a Jupiter-like or Saturn-like giant, which was given a circular orbit inside the stellar HZ at either an Earth-equivalent distance or in the center of the HZ. The Mars-like moon was given an initial eccentricity of 0.1, measured relative to its orbit about the planet. It was expected that the average eccentricity would decay as a result of tidal dissipation in the moon and planet. For each eccentric satellite system, I decided to also run a nearly identical simulation with the moon instead starting with a circular orbit. In this way, I could test if the stellar perturbation raised the eccentricity to the same steady state value as was achieved following the decay from a higher initial value. For each 3-body simulation, I ran a corresponding 2-body simulation with just the planet and moon to show what the evolution would be without the influence of the star.

6.1 3-body Stability Considerations

With a central star ranging in mass from 0.075 $M_{\odot}$ to 0.6 $M_{\odot}$ and with my chosen properties for the host planet, the exomoon Hill stability became severally limited. This result stems from the decision to confine planetary orbits within the stellar HZ since the HZ is very close to the star in this stellar mass range. Following Equations (2.1) and (2.2), I expected a stability limit of $\sim 0.4\ R_{Hill}$ for my chosen moon orbits, all of which were prograde. For this research, I used a stability limit of $0.5\ R_{Hill}$, meaning, I did not simulate any system for which the moon's semimajor axis about the planet was greater than $0.5\ R_{Hill}$ for the planet-star binary. The results showed that for even the tightest exomoon orbit, which was an Io-like orbit at $a = 5.9\ R_P$, no stable systems were expected around stars less than 0.1 $M_{\odot}$. For this reason, I only ran extended simulations for stellar masses $\geq 0.1\ M_{\odot}$ using intervals of 0.1 $M_{\odot}$ (i.e. the considered star masses were 0.1, 0.2, 0.3, 0.4, 0.5, and 0.6 $M_{\odot}$).

For the described intervals of stellar mass, the stable region around a planet slowly increased with stellar mass (i.e. with increasingly larger HZ distances). As explained in subsection 5.1.1, I considered a discrete range of moon orbital distances for each star-planet pair. The distances were modelled after existing solar system moons. Not surprisingly, many of the wider moon orbits were unstable for the lowest star masses. This instability resulted in the moon becoming unbound from the planet. In the end, my 3-body simulations were only able to maintain long-term stability for a satellite orbit of $a_{sat} \lesssim 0.4\ R_{Hill}$, which was the expected value described above. A summary of the stable 3-body systems is provided in Table 6.1. Note that in the table the moon semimajor axes are modelled after the Solar System moons Io, Europa, Ganymede, Titan, and Callisto, respectively. The stability summaries are repeated in Tables 6.2 and 6.3 with the moon semimajor axes given in terms of the Hill Radius (R_{Hill}) of the host planet.

Table 6.1. 3-body stability summary. The J symbol means the moon was stable around a Jupiter-like planet, an S for a Saturn-like planet. The symbol "-" represents an unstable satellite system.

Earth-Equivalent Planet Orbit						
Star Mass	Planet Distance (AU)	Moon Semimajor Axis				
		5.9 R_P	9.6 R_P	15.3 R_P	21.0 R_P	26.9 R_P
0.1 $M_\odot$	-	-	-	-	-	-
0.2 $M_\odot$	0.076	J, S	-	-	-	-
0.3 $M_\odot$	0.11	J, S	J	-	-	-
0.4 $M_\odot$	0.15	J, S	J, S	-	-	-
0.5 $M_\odot$	0.21	J, S	J, S	J	-	-
0.6 $M_\odot$	0.29	J, S	J, S	J, S	J	-

Planet Orbit in Center of HZ						
Star Mass	Planet Distance (AU)	Moon Semimajor Axis				
		5.9 R_P	9.6 R_P	15.3 R_P	21.0 R_P	26.9 R_P
0.1 $M_\odot$	0.051	J	-	-	-	-
0.2 $M_\odot$	0.11	J, S	J	-	-	-
0.3 $M_\odot$	0.16	J, S	J, S	-	-	-
0.4 $M_\odot$	0.22	J, S	J, S	J	-	-
0.5 $M_\odot$	0.30	J, S	J, S	J, S	J	-
0.6 $M_\odot$	0.41	J, S	J, S	J, S	J, S	J

Table 6.2. 3-body stability summary for a Jupiter-like host planet. The moon semimajor axes are presented as fractions of R_{Hill}. Blue shaded cells represent stable moon orbits.

Earth-Equivalent Planet Orbit					
Star Mass	Moon Semimajor Axis				
	5.9 R_{Jup}	9.6 R_{Jup}	15.3 R_{Jup}	21.0 R_{Jup}	26.9 R_{Jup}
0.1 $M_{\odot}$	0.54	0.88	1.4	1.9	2.5
0.2 $M_{\odot}$	0.32	0.52	0.82	1.1	1.4
0.3 $M_{\odot}$	0.25	0.41	0.66	0.91	1.2
0.4 $M_{\odot}$	0.20	0.33	0.53	0.72	0.93
0.5 $M_{\odot}$	0.16	0.26	0.41	0.57	0.72
0.6 $M_{\odot}$	0.12	0.20	0.31	0.43	0.55

Planet Orbit in Center of HZ					
Star Mass	Moon Semimajor Axis				
	5.9 R_{Jup}	9.6 R_{Jup}	15.3 R_{Jup}	21.0 R_{Jup}	26.9 R_{Jup}
0.1 $M_{\odot}$	0.38	0.61	0.98	1.3	1.7
0.2 $M_{\odot}$	0.22	0.36	0.57	0.79	1.0
0.3 $M_{\odot}$	0.18	0.29	0.46	0.63	0.80
0.4 $M_{\odot}$	0.14	0.23	0.37	0.50	0.65
0.5 $M_{\odot}$	0.11	0.18	0.29	0.39	0.51
0.6 $M_{\odot}$	0.09	0.14	0.22	0.30	0.39

Table 6.3. 3-body stability summary for a Saturn-like host planet. The moon semimajor axes are presented as fractions of R_{Hill}. Blue shaded cells represent stable moon orbits.

Earth-Equivalent Planet Orbit					
Star Mass	Moon Semimajor Axis				
	5.9 R_{Sat}	9.6 R_{Sat}	15.3 R_{Sat}	21.0 R_{Sat}	26.9 R_{Sat}
0.1 $M_{\odot}$	0.66	1.1	1.7	2.3	3.0
0.2 $M_{\odot}$	0.39	0.63	1.0	1.4	1.8
0.3 $M_{\odot}$	0.31	0.50	0.80	1.1	1.4
0.4 $M_{\odot}$	0.25	0.40	0.64	0.88	1.1
0.5 $M_{\odot}$	0.19	0.32	0.50	0.69	0.88
0.6 $M_{\odot}$	0.15	0.24	0.38	0.53	0.67

Planet Orbit in Center of HZ					
Star Mass	Moon Semimajor Axis				
	5.9 R_{Sat}	9.6 R_{Sat}	15.3 R_{Sat}	21.0 R_{Sat}	26.9 R_{Sat}
0.1 $M_{\odot}$	0.46	0.75	1.2	1.6	2.1
0.2 $M_{\odot}$	0.27	0.44	0.70	0.96	1.2
0.3 $M_{\odot}$	0.22	0.35	0.56	0.77	0.98
0.4 $M_{\odot}$	0.17	0.28	0.45	0.61	0.79
0.5 $M_{\odot}$	0.14	0.22	0.35	0.48	0.62
0.6 $M_{\odot}$	0.10	0.17	0.27	0.37	0.47

6.2 Short-Term Orbital Variation

While significant eccentricity evolution for a moon involved timescales of millions of years, on much shorter timescales, the instantaneous eccentricity fluctuated substantially for the 3-body systems. An example of typical short-term fluctuations is provided in Figure 6.1. The figure represents three individual simulations. The top and middle plots involved 3-body simulations, while the bottom plot represents an isolated planet-moon (2-body) simulation. The satellite system represented in the top plot had a tight planetary orbit around the central star ($a_P = 0.078$ AU) due to the extra short distance of the HZ. The middle plot represents the same planet-moon binary around a more massive star which provided a noticeably larger orbital distance ($a_P = 0.21$ AU). In these two upper plots, the period of the high frequency oscillation corresponds to the moon's orbit about the planet, while the lower frequency oscillation in the overall behavior corresponds to the planet's orbit about the star. The latter stems from the planet developing a very small, but non-zero eccentricity relative to the star, caused by the presence of the moon.

The diminishing influence of the star at higher stellar masses (i.e. wider HZ distances) is clearly seen by the decreasing amplitudes of fluctuation in Figure 6.1. When the star's influence is removed completely, as represented by the bottom plot, the fluctuations cease and the satellite eccentricity remains quite stable.

The short-period eccentricity fluctuations in the 3-body simulations are not particularly surprising. My definition of eccentricity is based on traditional formulations involving a two-body problem which assumes Keplerian motion for a smaller body orbiting a larger body. With the addition of a third body, the actual motion of the moon as it orbits the planet, which in-turn orbits the star, is not exactly Keplerian about the planet. Therefore, it seems reasonable to see variability that corresponds with the proximity of the star. It is also of note that these relatively short period fluctuations in eccentricity are the result of gravitational perturbations, not tidal interactions which occur over much longer timescales. To verify this, I ran the same simulations without tidal interactions and reproduced identical results.

Also significant about the variability shown in Figure 6.1 is that the eccentricity fluctuates about an average value of roughly 0.1. This average value happens to also be the initial value set for these particular simulations. This result was not by chance and had to be carefully constructed. It was determined during early testing that the moon's average eccentricity over the period of one *planetary* orbit[1] could deviate in comparison to its

[1]One planetary orbit around the star involves about a dozen orbits of the moon around the planet.

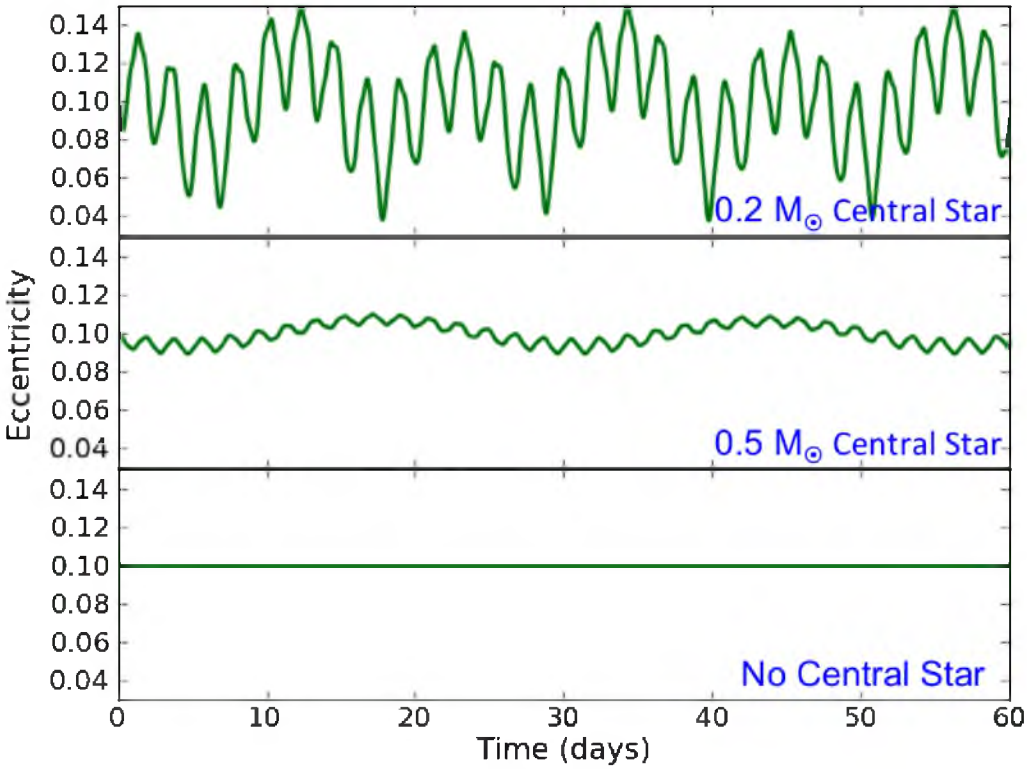

Figure 6.1. Comparison of satellite eccentricity for three different simulations. The top and middle plots represent 3-body simulations. The bottom plot represents an isolated planet-moon system (2-body simulation).

assigned initial value. The average value would scatter either higher than the initial value, or lower than the initial value, but not both (meaning, the average did not oscillate). The degree to which the average eccentricity deviated depended on the moon's initial position relative to an imaginary line between the star and planet.

While the scattering of the initial eccentricity is interesting, it does not represent any 'real-world' physical concerns. The scattering is merely an artifact (i.e. product) of my system creation process. This issue extends again from the fact that the moon's initial eccentricity is defined relative to the planet, assuming an isolated two-body system. As a consequence, from the moon's perspective, when I start a 3-body simulation, it is as if the star suddenly appeared. Naturally, the initial tug from the star is going to have a lasting effect on the moon's orbit as it adjust to a new source of gravitational perturbation. A potential fix to this issue would be to define the initial orbits relative to the planet-moon center of mass. However, I did not do this because satellite orbital elements for tidal

considerations would still need to be measured relative to the planet. In addition, I had no real need to ensure a specific value for the initial eccentricity since I was not simulating known systems. My primary concern in this regard was to maintain consistency between my many simulated systems. Therefore, I decided to use only initial positions and velocities which produced an initial average eccentricity that was as close as possible to a desired value. Here, I refer to an average over the course of several planetary orbits.

In this subsection, I have focused on satellite eccentricity, and while its short-term behavior is interesting, my ultimate interest is the tidal heating of a moon and its potential impact on habitability. Due to the strong dependence of tidal heating on eccentricity ($H \propto e^2$), I could also show similar short-period fluctuations for the heating of the moon. However, my primary concern is the long-term tidal evolution, not the specific short-term behavior. For this reason, I chose to focus on the average values for tidal heating. I took this focus into consideration when I created my simulation program. I designed it so that each time a simulation was to output data, it took several samples[2] over the course of one moon orbit and then reported the average values over that period of time. With these considerations, for the remainder of this dissertation I will present only orbit averaged heating values and will focus on tidal heating rather than eccentricity.

6.3 Results

After completing my investigations into system stability and short-term behavior, I was finally left with a set of 3-body systems for which I could expect stability and reasonably predict the long-term behavior. This level of confidence was important since each simulation would require a significant investment of computational processing time. Once I began running extended simulations, their integrated time was continually extended until one of three results was achieved: (1) After an initial decrease, the orbit-averaged surface heat flux (h) settled to a reasonably constant value; (2) The average surface heat flux had not yet stabilized, but had already fallen well below the proposed maximum limit for habitability, $h_{max} = 2\ W/m^2$; (3) The tidal evolution was slow enough that it was not practical to continue the simulation further.

For planetary orbits in the center of the HZ, tidal evolution plots for moons with a Jupiter-like host planet are shown in Figures 6.2, 6.3, 6.4, 6.5, and 6.6. Similar plots for a Saturn-like host planet in the center of the HZ are included in Figures 6.7, 6.8, 6.9, and 6.10. Results for moons with a Jupiter-like host planet at Earth-equivalent distances are

[2]The sampling over one moon orbit involved about 15 randomly chosen points along the orbit.

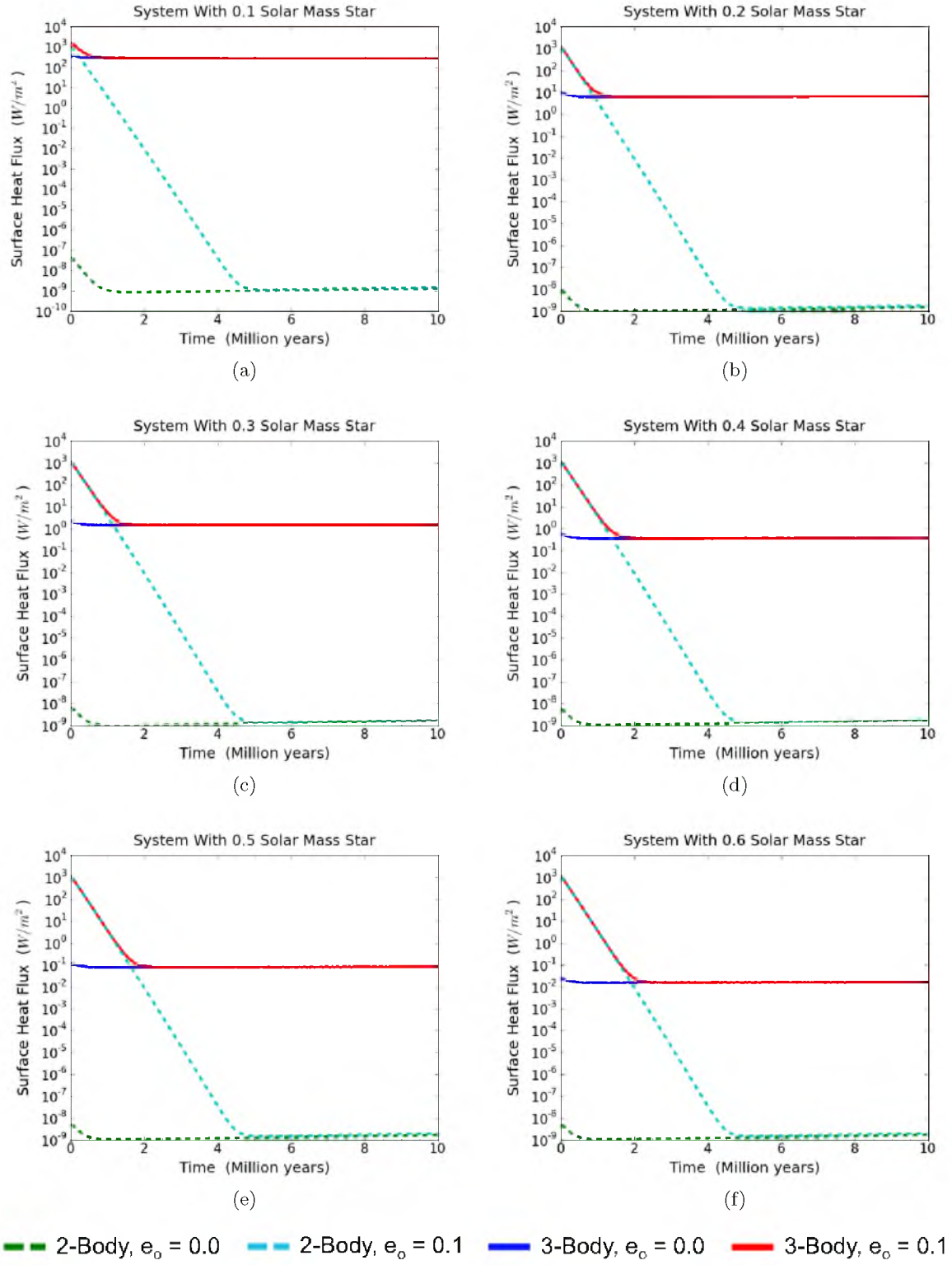

Figure 6.2. Satellite tidal evolution. Planet orbit in the center of the HZ. Io-like moon orbit. Jupiter-like host planet.

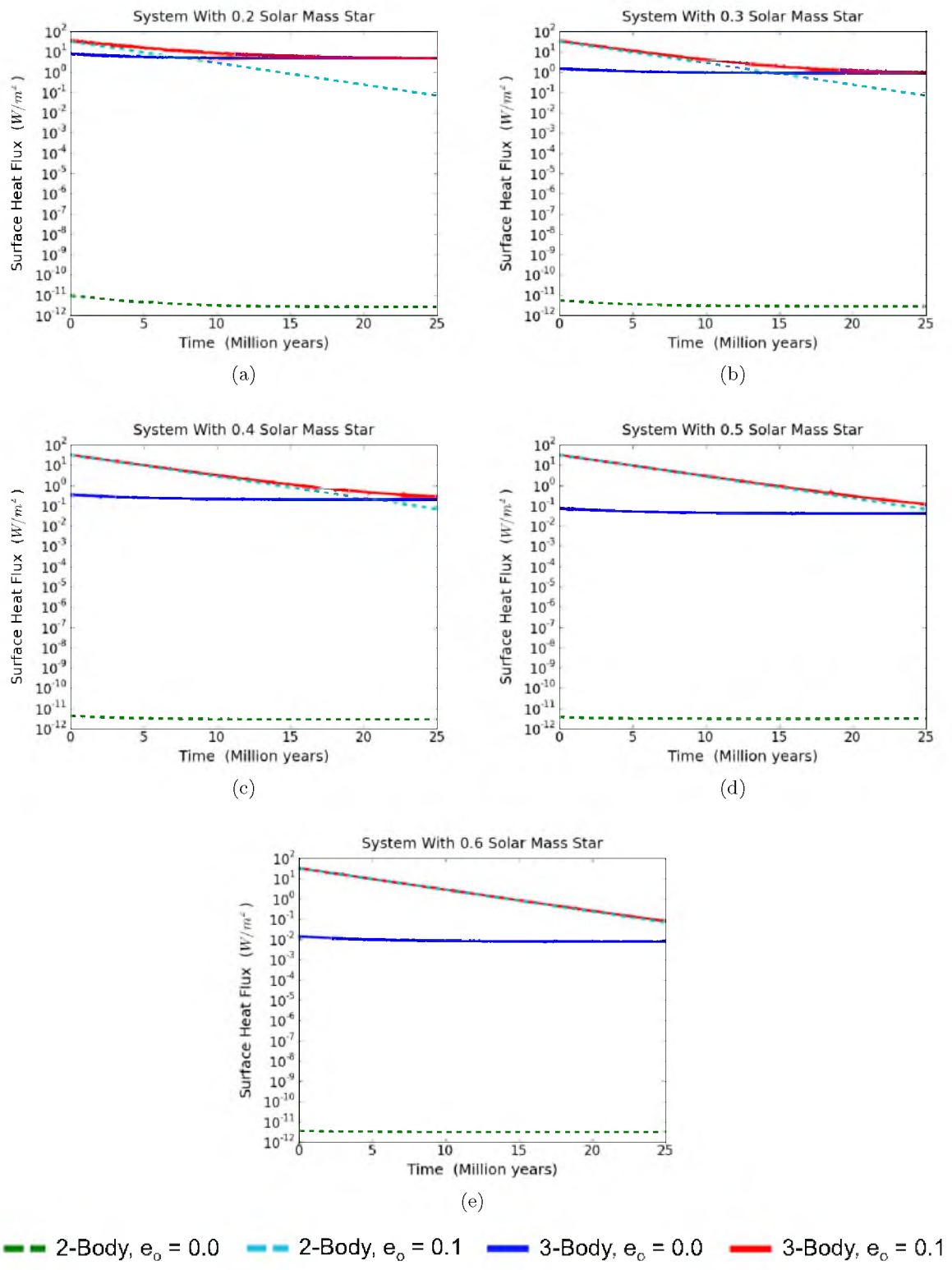

Figure 6.3. Satellite tidal evolution. Planet orbit in the center of the HZ. Europa-like moon orbit. Jupiter-like host planet.

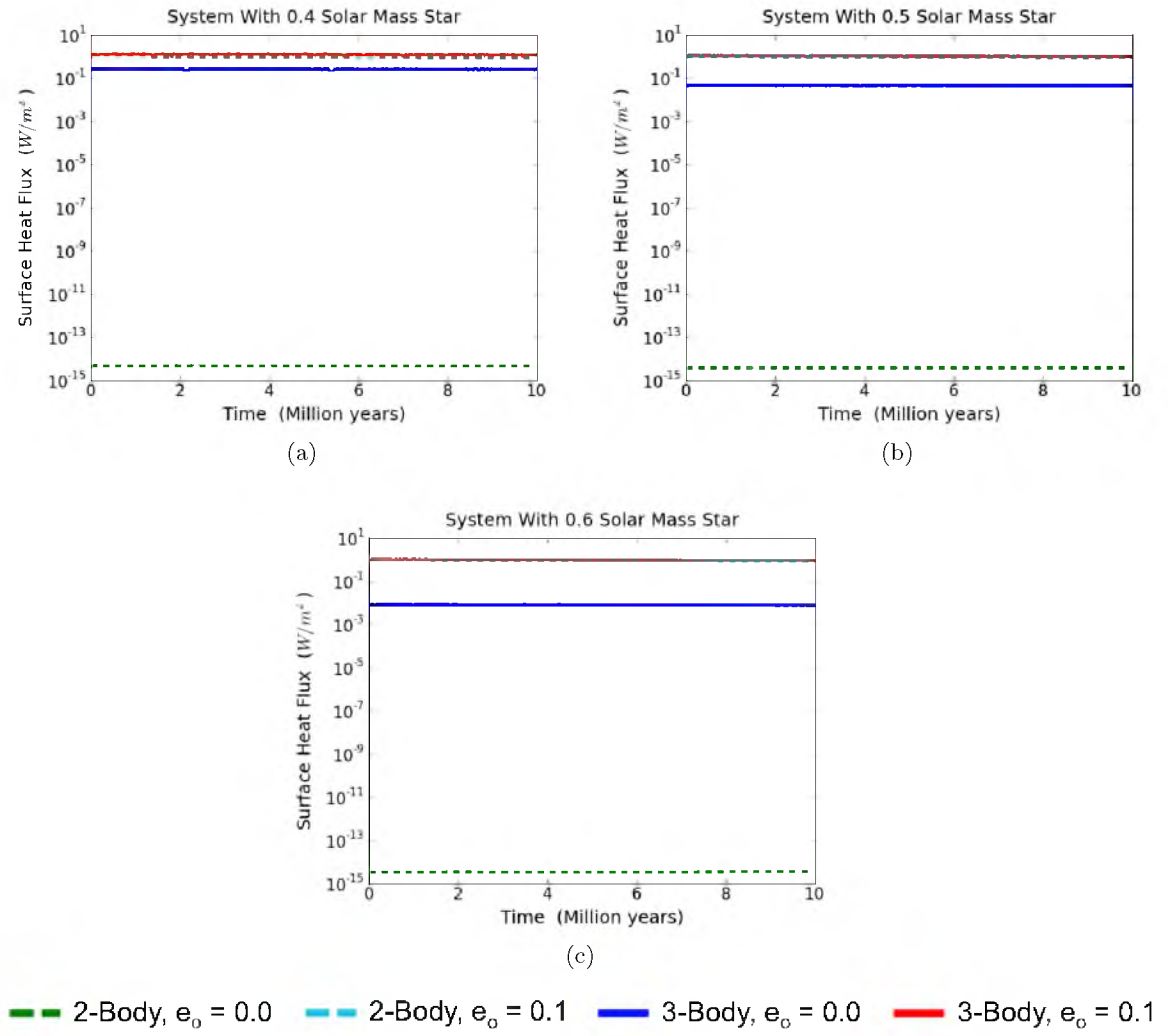

Figure 6.4. Satellite tidal evolution. Planet orbit in the center of the HZ. Ganymede-like moon orbit. Jupiter-like host planet.

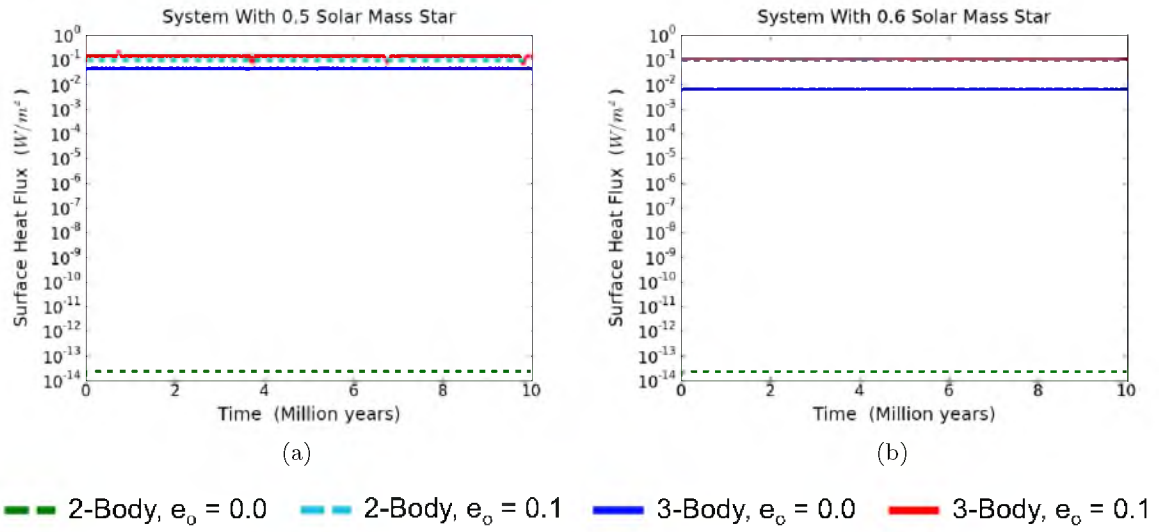

Figure 6.5. Satellite tidal evolution. Planet orbit in the center of the HZ. Titan-like moon orbit. Jupiter-like host planet.

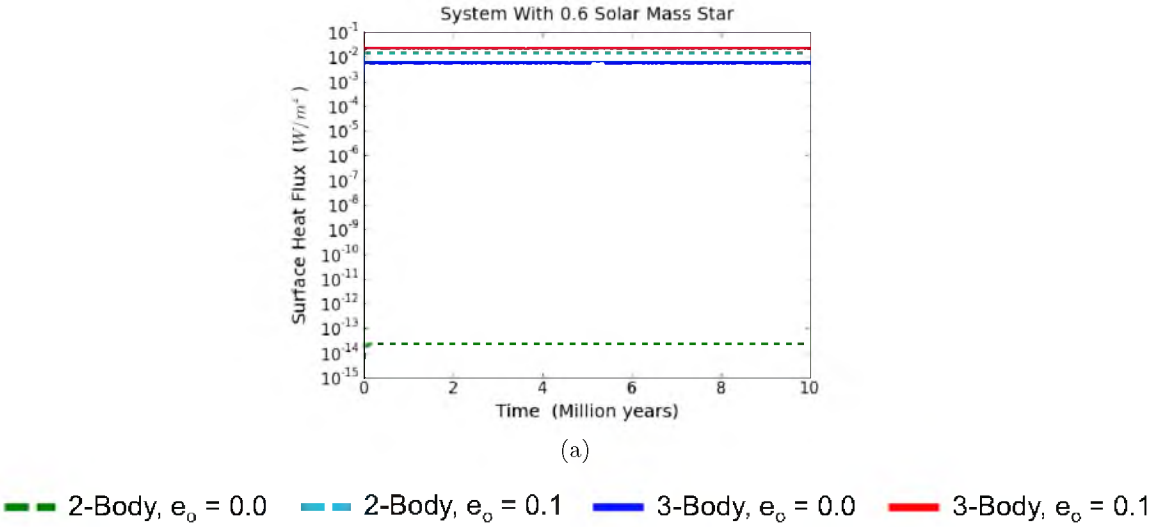

Figure 6.6. Satellite tidal evolution. Planet orbit in the center of the HZ. Callisto-like moon orbit. Jupiter-like host planet.

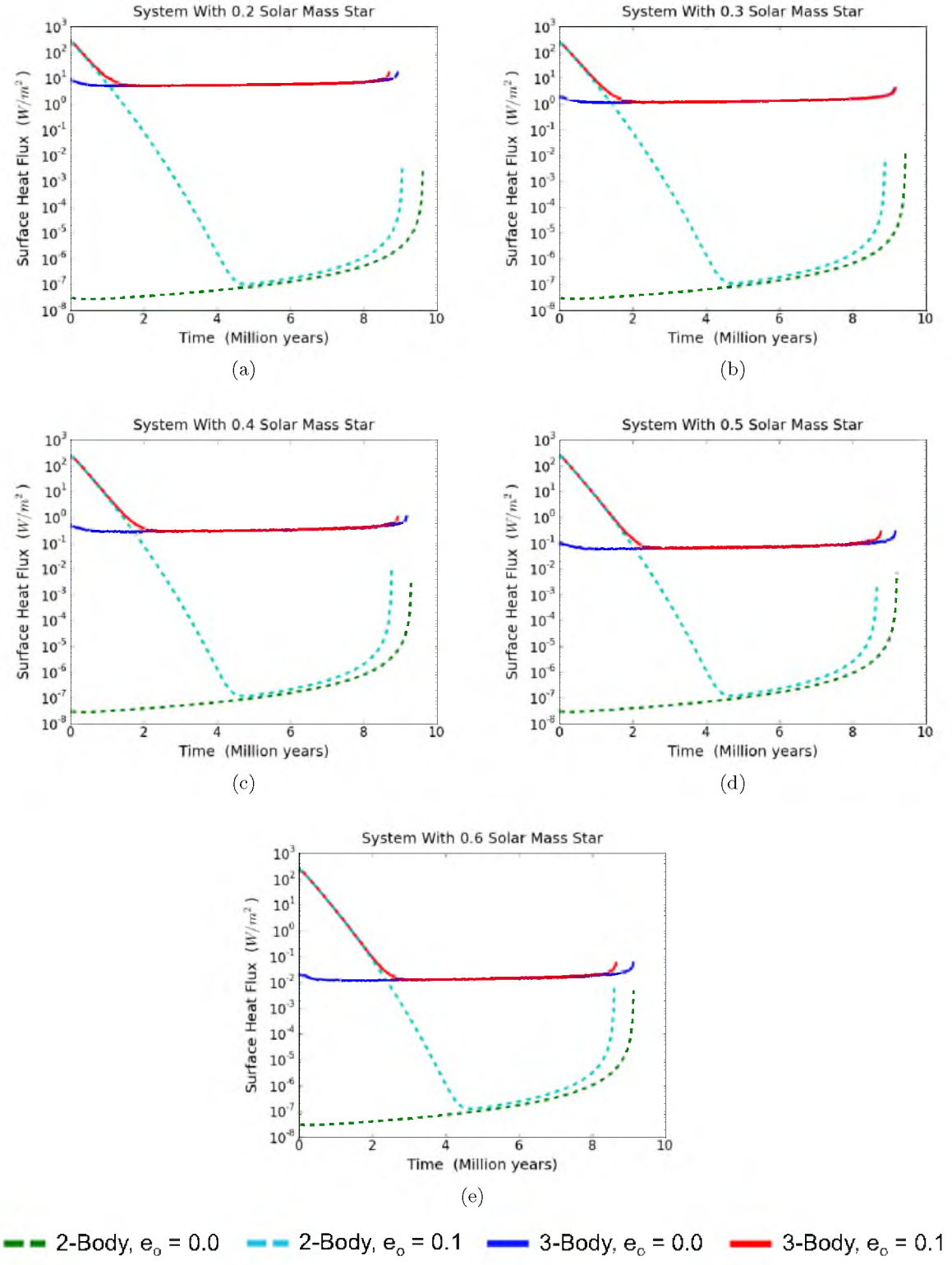

Figure 6.7. Satellite tidal evolution. Planet orbit in the center of the HZ. Io-like moon orbit. Saturn-like host planet.

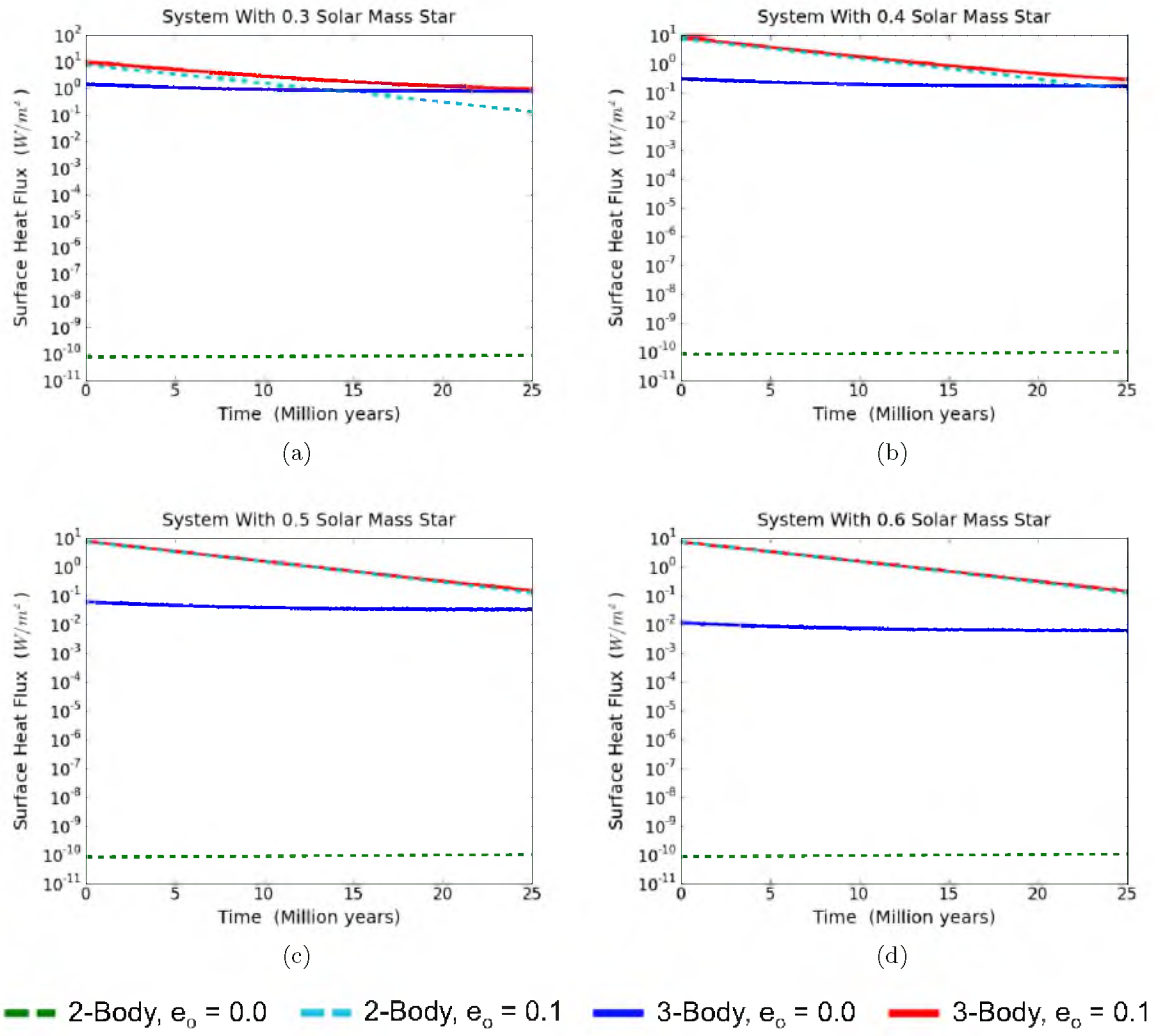

Figure 6.8. Satellite tidal evolution. Planet orbit in the center of the HZ. Europa-like moon orbit. Saturn-like host planet.

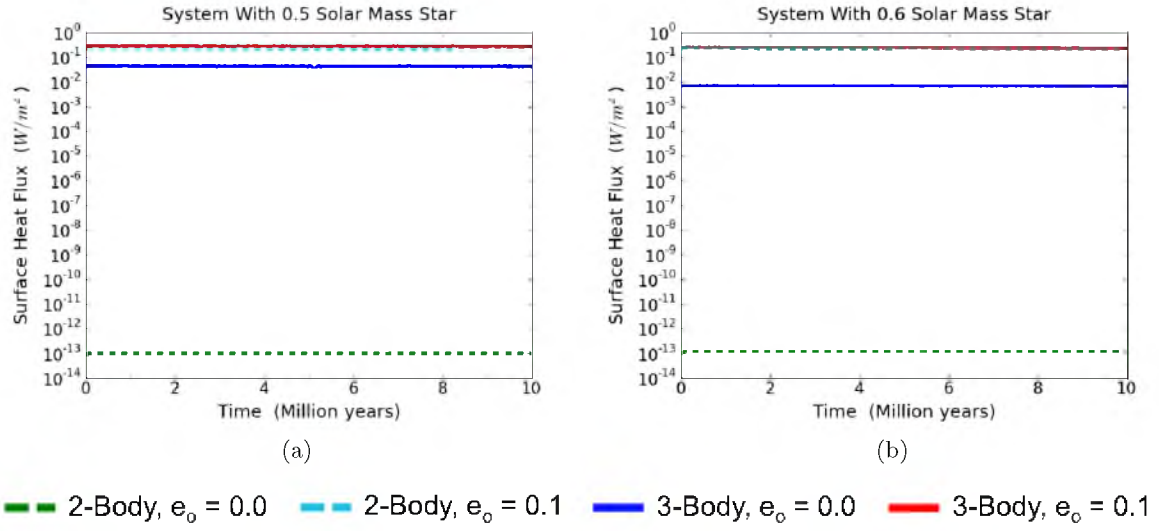

Figure 6.9. Satellite tidal evolution. Planet orbit in the center of the HZ. Ganymede-like moon orbit. Saturn-like host planet.

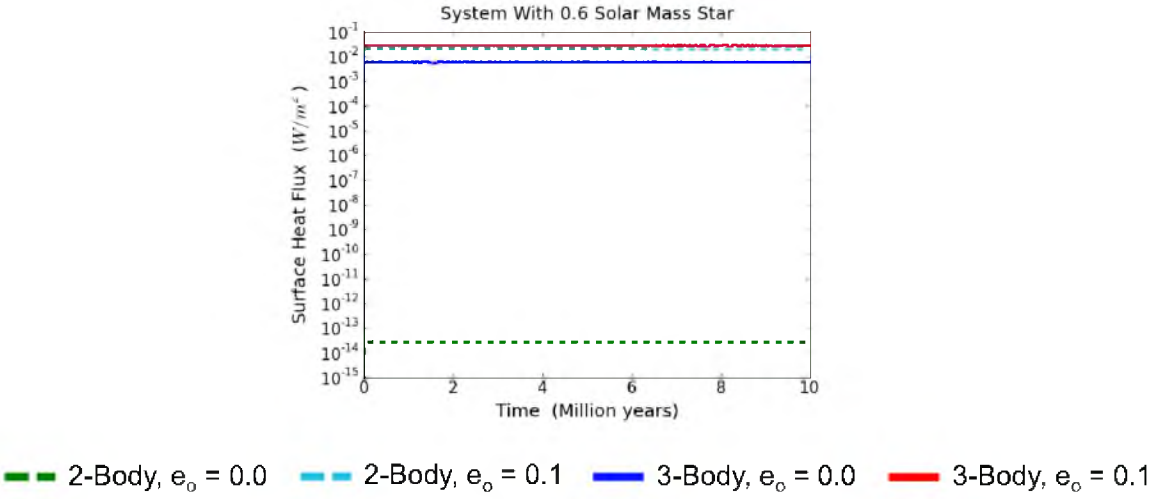

Figure 6.10. Satellite tidal evolution. Planet orbit in the center of the HZ. Ganymede-like moon orbit. Saturn-like host planet.

included in Figures 6.11, 6.12, 6.13, and 6.14, while Saturn-like host planets are represented in Figures 6.15, 6.16, and 6.17.

Displayed in these figures is the average surface heat flux (h) in the moon as a function of time, with h defined by Equation 4.21. Each figure includes results for one specific moon orbital distance while the individual plots in each figure represent the different masses considered for the central star. Note that a greater star mass signifies a larger orbital distance for the planet (refer to Table 6.1 for the exact planet distances). Each plot includes four curves which show results for four separate simulations. These include a 3-body system where the moon began with an average eccentricity of $e_o = 0.1$ and a nearly identical 3-body system with the exception of an initially circular orbit for the moon. The other two curves represent isolated planet-moon (2-body) systems which used the same initial conditions for the planet and moon as the corresponding 3-body simulations. Comparing the 2-body and 3-body curves is useful in demonstrating the star's influence on the long-term tidal evolution of the moon. An extended and complete discussion of the 3-body simulation results is performed in section 6.4.

6.4 Discussion

First, it is important to reemphasizing the motivation for each one of the four curves shown in every evolution plot. The red curve represents a 3-body system consisting of a low-mass star, a giant planet in the HZ, and a Mars-like moon that was given an initial eccentricity of 0.1 relative to the planet. The focus of this study involves the long-term behavior of this particular curve. With it, I am testing the extent to which a low-mass star has influence over a moon's evolution in the HZ as a consequence of the short distance of the HZ. This is done by comparing the red curve to the dashed cyan curve which represents an isolated planet-moon binary that began the simulation with the same initial conditions, minus the star. Essentially, the dashed cyan curve shows what the red curve would look like without the influence of the central star.

The blue and the dashed green curves in each plot relate directly to the red and dashed cyan curves, respectively, with the only difference being an initial eccentricity of zero. Since tidal heating works to circularize the orbits, these initially circular orbits should continue to maintain little to no heating, unless of course there are significant perturbations to the orbit. Therefore, the purpose of these simulations was to test if the central star would excite the heating upward to the same steady state value that was achieved through the slow decay of an initially higher value. If that result was observed, then there is confidence

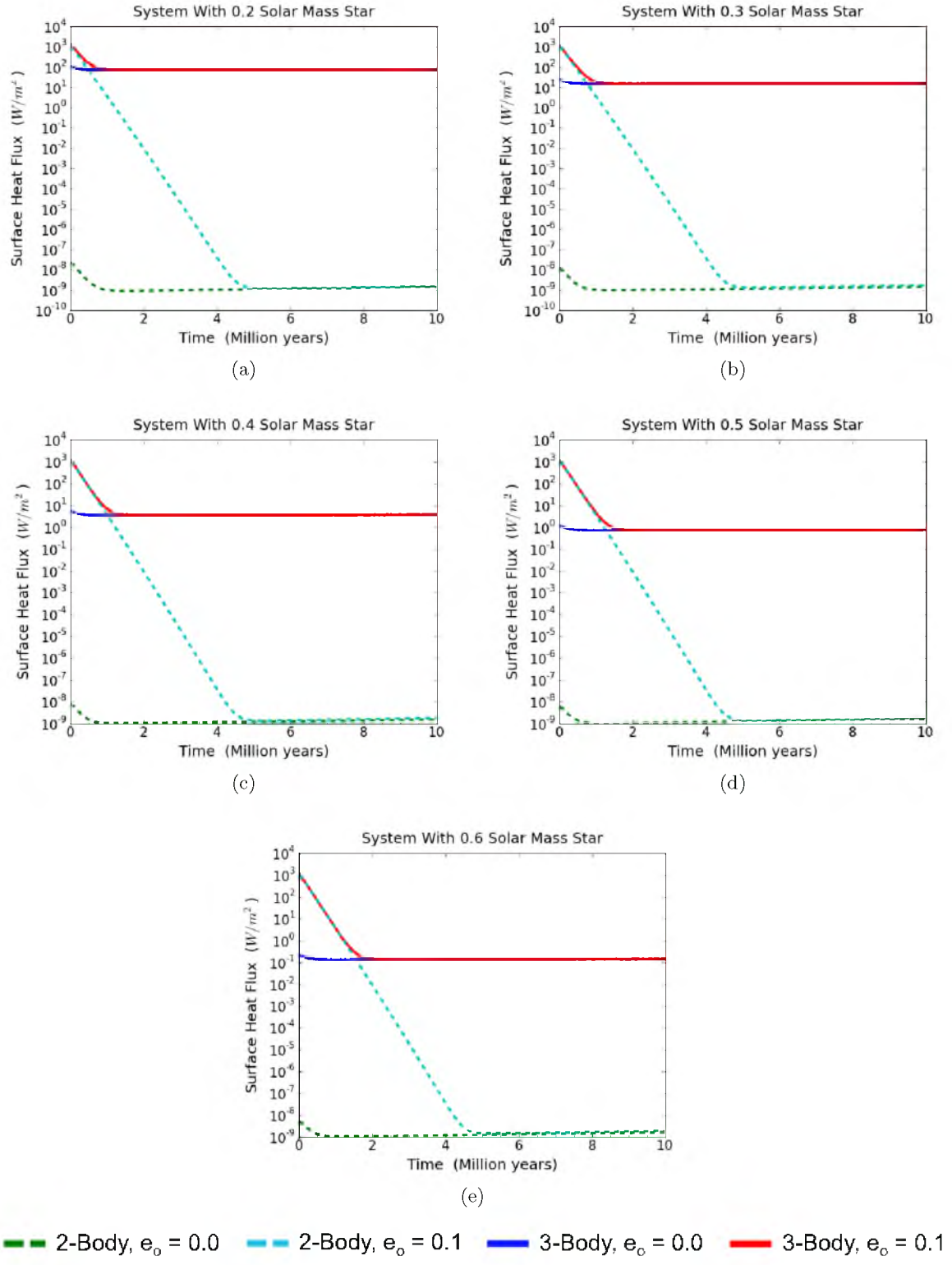

Figure 6.11. Satellite tidal evolution. Earth-equivalent planetary distance. Io-like moon orbit. Jupiter-like host planet.

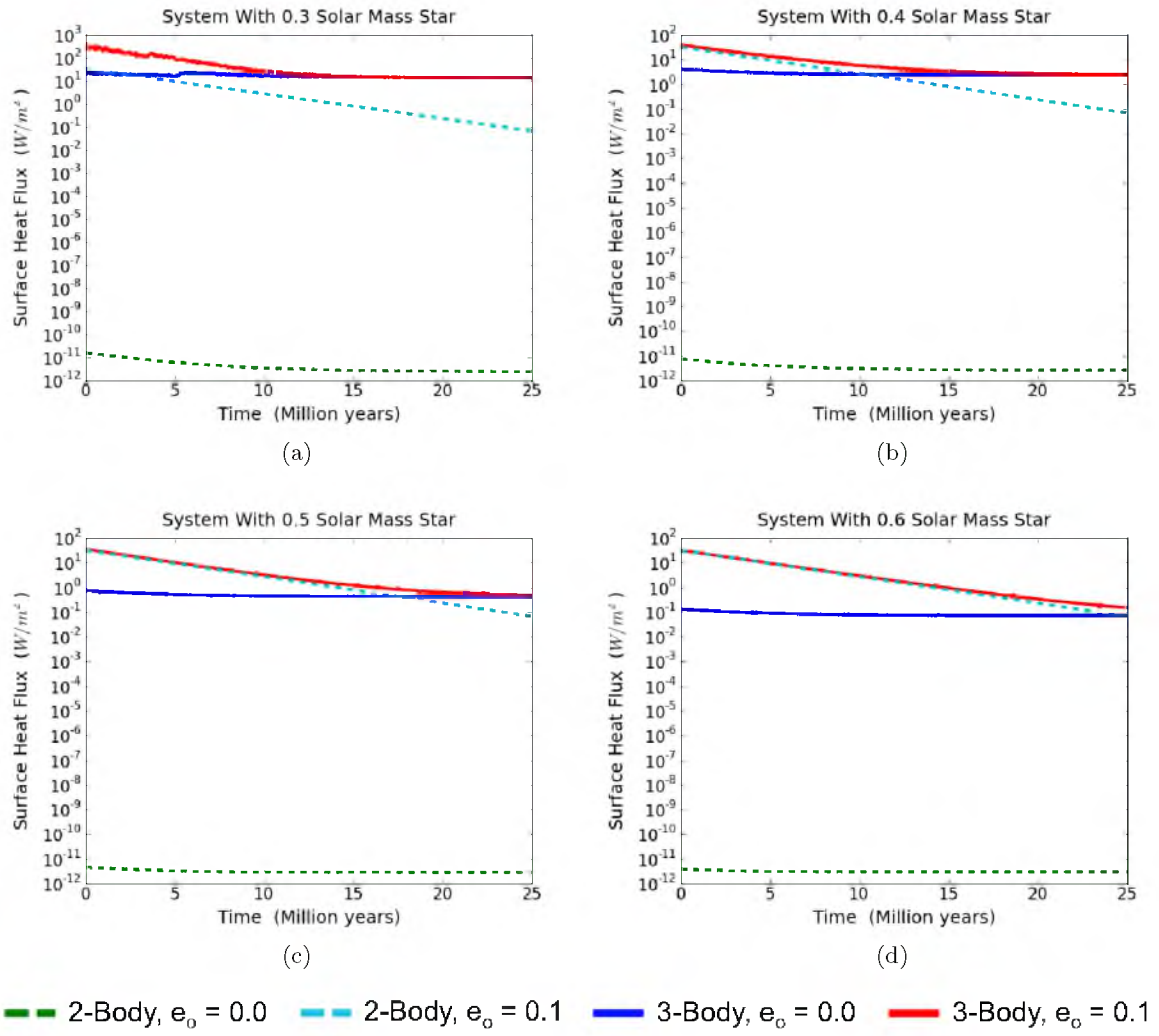

Figure 6.12. Satellite tidal evolution. Earth-equivalent planetary distance. Europa-like moon orbit. Jupiter-like host planet.

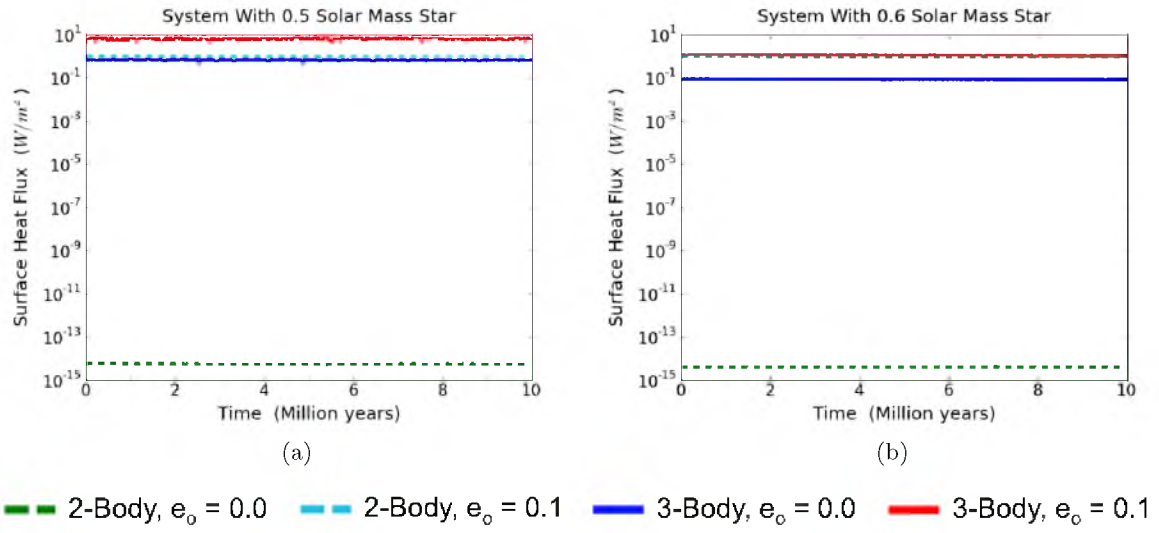

Figure 6.13. Satellite tidal evolution. Earth-equivalent planetary distance. Ganymede-like moon orbit. Jupiter-like host planet.

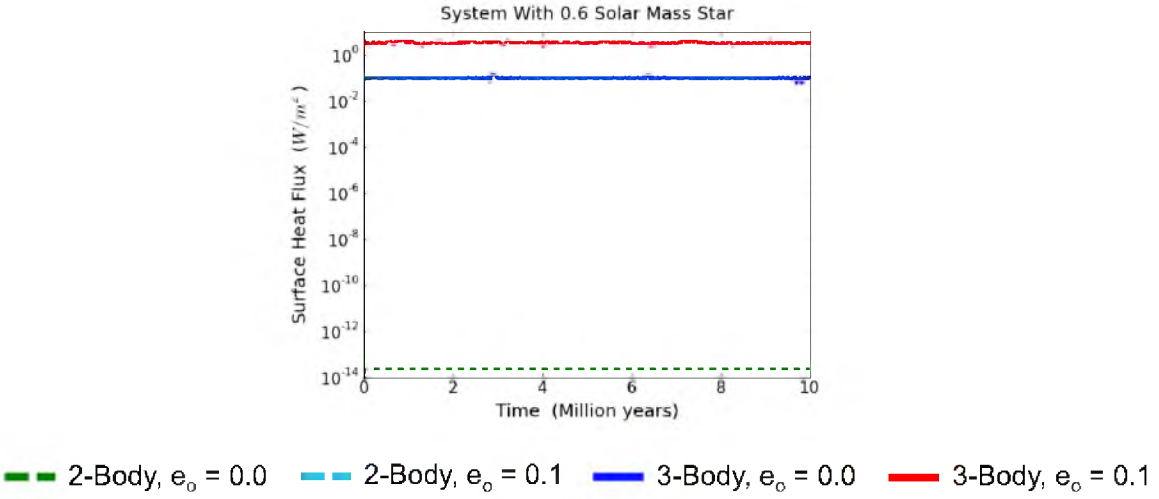

Figure 6.14. Satellite tidal evolution. Earth-equivalent planetary distance. Titan-like moon orbit. Jupiter-like host planet.

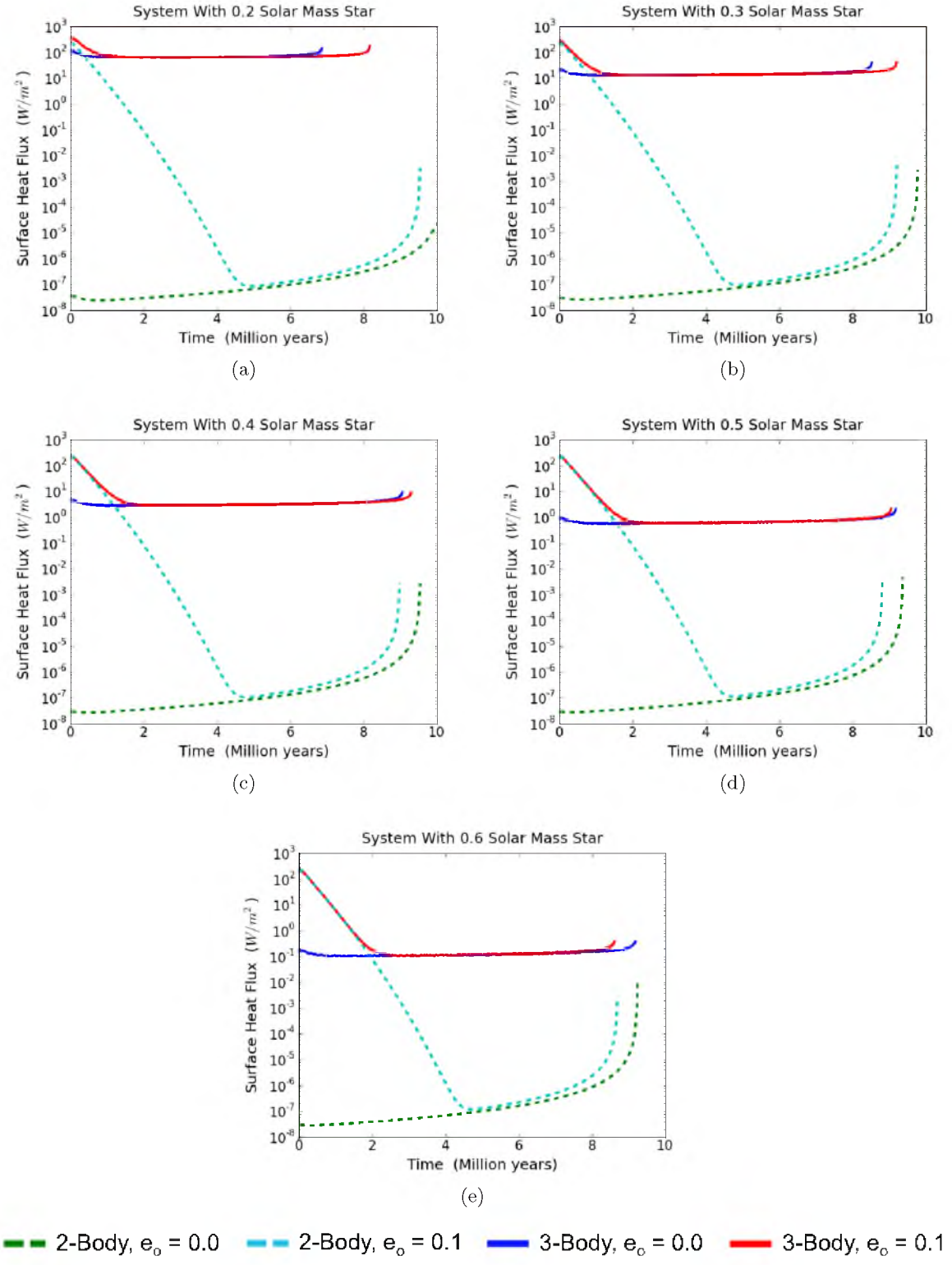

Figure 6.15. Satellite tidal evolution. Earth-equivalent planetary distance. Io-like moon orbit. Saturn-like host planet.

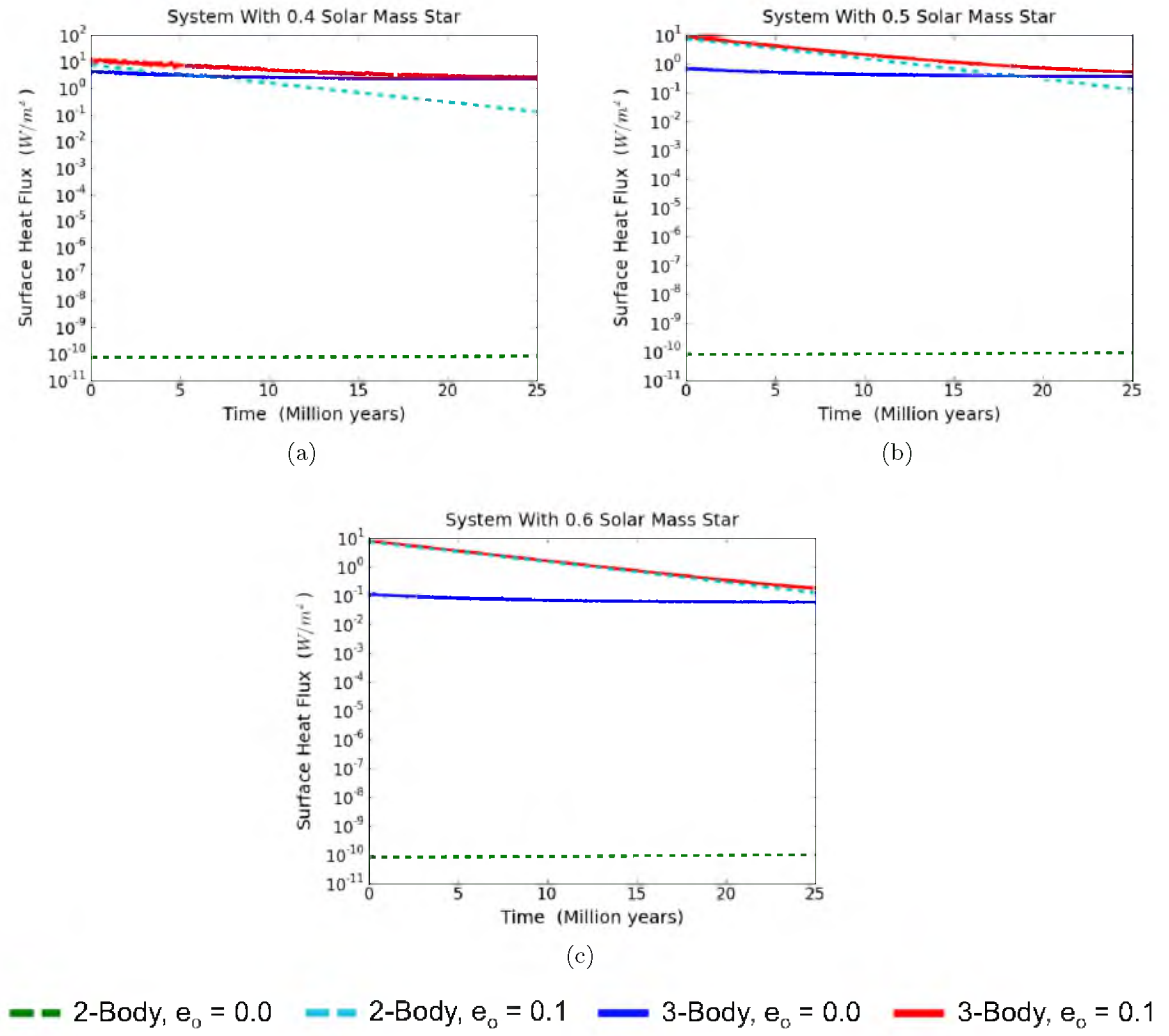

Figure 6.16. Satellite tidal evolution. Earth-equivalent planetary distance. Europa-like moon orbit. Saturn-like host planet.

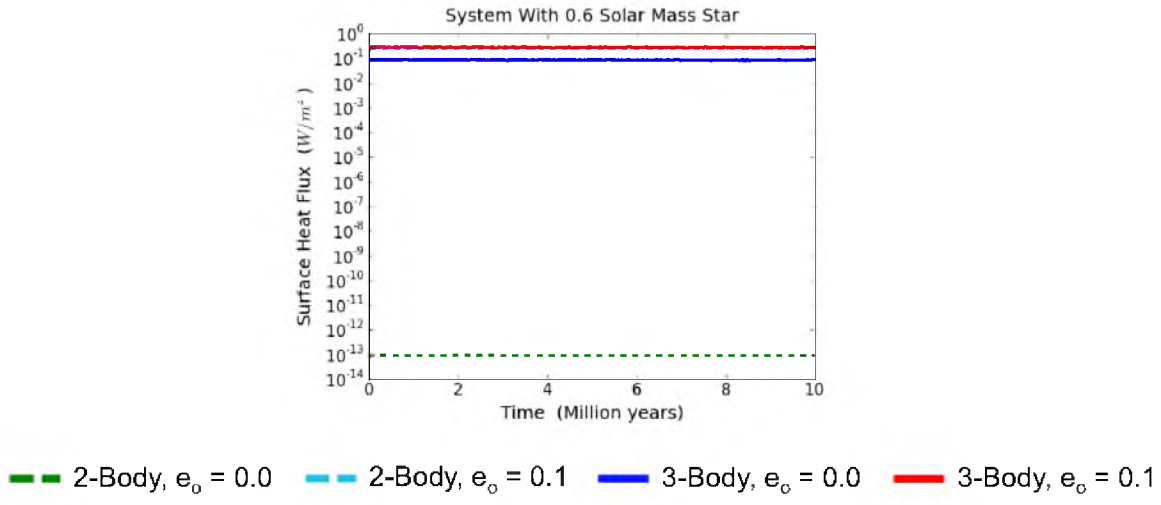

Figure 6.17. Satellite tidal evolution. Earth-equivalent planetary distance. Ganymede-like moon orbit. Saturn-like host planet.

in stating that a non-zero, steady state value for the surface heat flux was the product of perturbations from the star and not simply based on my choice of initial conditions or an external artifact of my computer code. As it turned out, this desired result was observed for Io-like and Europa-like orbital distances. On the other hand, no such behavior was observed for the wider orbits, which included the Ganymede-like, Titan-like, and Callisto-like orbits. Instead, the relative difference between the eccentric and circular simulations remained constant throughout. Given the 10 million years of simulated time, this should have been sufficient to show some sort of long-term excitation, if the system truly had the potential for it.

In most of the tidal evolution plots, the red curve and the dashed cyan curve appear to have the same initial behavior. However, there seems to be some exceptions to this, where the two curves do not line up initially. I refer specifically to Figures 6.5(a), 6.6(a), 6.12(a), 6.13(a), and 6.14. The discrepancy does not actually raise cause for concern as the explanation is simply the same artifact of system creation that was described in section 6.2. For these systems, the moons are near the stability limit for their particular star-planet system. As such, they are more affected by the 'sudden' appearance of the star at the beginning of the simulation, the result being that their initial orbit is more noticeably perturbed relative to more tightly bound systems.

After accounting for any initial discrepancy in the eccentric 3-body and 2-body results, my specific concern is actually the difference in the red and cyan curves by the end of the simulation. If the star truly has a significant influence on the moon, then the excitation that results from its continual perturbations should stop the moon's eccentricity from reaching zero, thus maintaining a non-zero tidal heating rate. Therefore, the slope of the red line should begin to deviate from the dashed cyan line and eventually level off, indicating a sustainable value for the surface heat flux. This predicted behavior is observed for all the Io-like and Europa-like orbital distances. It should be pointed out that the timescales necessary to achieve the constant state were more than double the estimates listed in Table 5.3. For convenience, I will refer to Io-like and Europa like orbits as "short" orbits. At these distances, the initially circular simulation eventually reached the same approximate steady state value as the noncircular system. This result helps to confirm the degree of excitation to which the central star can influence the tidal evolution of a moon.

An examination of Figures 6.7 and 6.15 shows unique behavior that is not observed in any of the other figures. In these simulations, the surface heat flux rapidly increases near the end of the simulated time. The cause for this behavior was already discussed in

section 5.3. Using 2-body models, I showed that Mars-like moons with Io-like orbits and Saturn-like host planets experience significant evolution in their semimajor axis as a result of tidal torques and exchanges of angular momentum. These 3-body results indicate that the star's influence does little to change this long-term behavior. In this case, the rapid rise in tidal heating is due to the equally rapid decay of the moon's semimajor axis as the moon spirals ever closer to the planet. The sudden end to the plots in Figures 6.7 and 6.15 reflects the early termination of the simulations when the moon became too close to the planet. This occurred when the distance between their centers became less than two planet radii. Given the rapid decay at this point, the moon will soon fall completely into the planet. Notice that the complete inward spiral occurred in less than 10 million years.

In conclusion for the shorter orbits, perturbations from a low-mass star can prevent the eventual circularization from tidal heating and are able to maintain non-zero heating levels in the moon for extended periods of time. While this effect was predicted to occur, this is the first instance in which it has actually been tested with an evolution model that simultaneously and self-consistently considered gravitational and tidal effects. Predictions for the intensity of the heating and consequences for exomoon habitability are discussed in subsection 6.4.1.

At wider orbital distances of $a_{sat} \gtrsim 15R_p$, very little change to the surface heat flux occurred over 10 million years. Also for convenience, reference to these distances as "wide" orbits will correspond to Ganymede, Titan, and Callisto-like moon orbits. In accordance with the lack of surface heat flux evolution at wide orbits, there was very little relative deviation from the 2-body models. I expected this behavior based on estimates of eccentricity damping timescales and early 2-body test runs. However, the potential for stellar excitation was untested, making the simulations necessary. For these orbits, it is important to compare the scales involved. Even with the influence of the star, most of their surface heat fluxes are roughly 0.1 W/m^2 and below. This is a full order of magnitude less than the shorter orbit moons and well below h_{max}. Such low heating rates would not be expected to noticeably effect the orbit over the timescales considered.

At first glance, there appears to be two exceptions to my previous statement. Figures 6.13(a) and 6.14 show average values above 2 W/m^2 for the eccentric 3-body systems (red curves) which are noticeably higher than the corresponding 2-body values (dashed cyan curves). Although this may seem like a meaningful result, it is actually just another artifact of the simulation process. It is obvious that stellar perturbation is the source for the discrepancy between the 3-body and 2-body models. The fact that the circular 3-body

simulations (blue curves) show no increase towards the same steady state values suggests that the high heating rates do not represent tidally evolved final states. Otherwise, 10 million years should have been enough time to show some excitation relative to the initial heating rate. This particular situation is similar to the one described above relating to system stability. These two particular moons orbit their host planet just inside the stability limit for their systems. Despite my attempts to create an average initial eccentricity of 0.1, the star had too much influence over these loosely bound satellites, resulting in higher than average eccentricities. The final eccentricities were 0.136 for plot 6.13(a) and 0.209 for plot 6.14. I suppose that this simulation could represent a satellite system that was recently formed through the capture method which could explain the high initial eccentricity. However, seeing as how the eccentricity will not decay for at least another billion years, these high eccentricity moons are too close to becoming unstable, and therefore, less than likely to exist in a real-life system. On the other hand, if the moon formed in-situ with a low eccentricity, then perhaps such a moon could exist. In that case, the heating rate would be low and not a concern for potential limitations to exomoon habitability.

The main take-away from the above situation is that tidal heating rates for wide orbit moons will arbitrarily reflect my choice of initial conditions. Therefore, I cannot make any definitive statements as to their ultimate tidal evolution. It is interesting that there is basically no change up or down in the surface heat flux at wide orbits. While tidal heating is not significantly evolving the orbits on these timescales, there is also very little excitation caused by the star's influence. It is worth noting that very few wide orbit moons are even stable in the red dwarf star range ($M_* \lesssim 0.5 M_\odot$). From this I concluded that even if a wide orbit moon is stable in the HZ of a low-mass star, the star's influence does not show significant potential for *maintaining* high levels of tidal heating via stellar excitation.

Aside from the interesting behavior shown in the time evolution plots, they are actually meant to provide only a qualitative demonstration of the tidal evolution. My primary interest in these results is actually the final value for the average surface heat flux at the end of each simulation. As a point of emphasis, these ending values represent one of three conditions mentioned at the beginning of section 6.3.

6.4.1 Simulation End Value Summary

The final 3-body simulation results for satellite systems in the center of the HZ are summarized in Tables 6.4 and 6.5, while the final results for systems at Earth-equivalent distances are summarized in Table 6.6. The tables show the average values at the end of each simulation and only include simulations that started with $e_o = 0.1$ for the moon.

Table 6.4. 3-body moon evolution summary for systems in the center of the stellar HZ around a Jupiter-like host planet. Values represent the average at the end of each simulation. Shaded rows are 2-body planet/moon systems. Red text indicates steady state values above h_{max}. Values of ** indicates the moon spiraled into the planet.

Jupiter-like Host Planet							
Moon Distance ($R_{Jupiter}$)	Star Mass ($M_{\odot}$)	h (W/m^2)	h_{conv} (W/m^2)	e	a/a_o	F_{glob} (W/m^2)	Sim. Time (10^6 Years)
Io-like 5.9	–	0.00	0.00	0.000	0.95	–	10
	0.1	264.70	421.93	0.030	0.82	371	10
	0.2	6.46	11.09	0.008	0.94	113	10
	0.3	1.51	2.59	0.004	0.95	107	10
	0.4	0.38	0.66	0.002	0.95	106	10
	0.5	0.08	0.14	0.001	0.95	107	10
	0.6	0.02	0.03	0.000	0.95	109	10
Europa-like 9.6	–	0.07	0.07	0.005	0.99	–	25
	0.2	4.94	7.22	0.049	0.98	109	25
	0.3	0.97	1.53	0.022	0.99	105	25
	0.4	0.29	0.39	0.011	0.99	104	25
	0.5	0.12	0.12	0.006	0.99	105	25
	0.6	0.08	0.08	0.005	0.99	108	25
Ganymede-like 15.3	–	0.87	0.80	0.094	1.00	–	10
	0.4	1.17	0.75	0.099	1.00	105	10
	0.5	0.98	0.83	0.094	1.00	106	10
	0.6	0.92	0.83	0.094	1.00	108	10
Titan-like 21.0	–	0.09	0.08	0.099	1.00	–	10
	0.5	0.13	0.08	0.101	1.00	105	10
	0.6	0.10	0.09	0.099	1.00	107	10
Callisto-like 26.9	–	0.01	0.01	0.100	1.00	–	10
	0.6	0.02	0.01	0.103	1.00	107	10

Table 6.5. 3-body moon evolution summary for systems in the center of the stellar HZ around a Saturn-like host planet. Values represent the average at the end of each simulation. Shaded rows are 2-body planet/moon systems. Red text indicates steady state values above h_{max}. Values of ** indicates the moon spiraled into the planet.

Saturn-like Host Planet							
Moon Distance (R_{Saturn})	Star Mass ($M_{\odot}$)	h (W/m^2)	h_{conv} (W/m^2)	e	a/a_o	F_{glob} (W/m^2)	Sim. Time (10^6 Years)
Io-like 5.9	–	**	**	**	**	**	10
	0.2	**	**	**	**	**	10
	0.3	**	**	**	**	**	10
	0.4	**	**	**	**	**	10
	0.5	**	**	**	**	**	10
	0.6	**	**	**	**	**	10
Europa-like 9.6	–	0.13	0.13	0.012	0.97	–	25
	0.3	0.97	1.38	0.041	0.97	105	25
	0.4	0.29	0.36	0.020	0.97	104	25
	0.5	0.15	0.15	0.013	0.97	106	25
	0.6	0.14	0.14	0.013	0.97	108	25
Ganymede-like 15.3	–	0.21	0.19	0.096	1.00	–	10
	0.5	0.27	0.19	0.099	1.00	105	10
	0.6	0.23	0.20	0.096	1.00	107	10
Titan-like 21.0	–	0.02	0.02	0.099	1.00	–	10
	0.6	0.03	0.02	0.103	1.00	107	10

Table 6.6. 3-body moon evolution summary for systems at Earth-equivalent distances. Values represent the average at the end of each simulation. Shaded rows are 2-body planet/moon systems. Red text highlights steady state values above h_{max}. Values of ** indicates the moon spiraled into the planet.

Jupiter-like Host Planet							
Moon Distance ($R_{Jupiter}$)	Star Mass ($M_\odot$)	h (W/m^2)	h_{conv} (W/m^2)	e	a/a_o	F_{glob} (W/m^2)	Sim. Time (10^6 Years)
Io-like 5.9	–	0.00	0.00	0.000	0.95	–	10
	0.2	72.67	121.33	0.024	0.92	292	10
	0.3	15.42	26.72	0.013	0.94	234	10
	0.4	3.68	6.45	0.006	0.94	223	10
	0.5	0.76	1.35	0.003	0.95	221	10
	0.6	0.14	0.25	0.001	0.95	222	10
Europa-like 9.6	–	0.07	0.07	0.005	0.99	–	25
	0.3	13.28	19.94	0.056	0.91	229	25
	0.4	2.42	3.94	0.035	0.98	218	25
	0.5	0.48	0.77	0.015	0.99	217	25
	0.6	0.15	0.18	0.008	0.99	219	25
Ganymede-like 15.3	–	0.87	0.80	0.094	1.00	–	10
	0.5	5.39	1.67	0.136	0.99	221	10
	0.6	1.03	0.82	0.094	1.00	219	10
Titan-like 21.0	–	0.09	0.08	0.099	1.00	–	10
	0.6	3.29	0.55	0.209	0.99	221	10

Saturn-like Host Planet							
Moon Distance (R_{Saturn})	Star Mass ($M_\odot$)	h (W/m^2)	h_{conv} (W/m^2)	e	a/a_o	F_{glob} (W/m^2)	Sim. Time (10^6 Years)
Io-like 5.9	–	**	**	**	**	**	10
	0.2	**	**	**	**	**	10
	0.3	**	**	**	**	**	10
	0.4	**	**	**	**	**	10
	0.5	**	**	**	**	**	10
	0.6	**	**	**	**	**	10
Europa-like 9.6	–	0.13	0.13	0.012	0.97	–	25
	0.4	2.64	3.71	0.068	0.96	218	25
	0.5	0.51	0.70	0.029	0.97	217	25
	0.6	0.18	0.19	0.015	0.97	219	25
Ganymede-like 15.3	–	0.21	0.19	0.096	1.00	–	10
	0.6	0.28	0.17	0.101	1.00	218	10

Included is the moon's average surface heat flux (defined by Equation (4.20)), the average eccentricity, and the average semimajor axis (in comparison to its initial value). The initial value for the semimajor axis is listed as the moon distance. I also included the 'conventional' surface heat flux h_{conv}. This value was calculated with Equation (4.3), using the simulation results for the final eccentricity and semimajor axis, and serves as a comparison between my chosen model and the conventional model for tidal heating. In regards to overall exomoon habitability, I included the orbit-averaged global flux (F_{glob}) received by a satellite, as defined by Equation (2.4). The total integration time considered for each simulation is also included.

In an effort to demonstrate the influence of the low-mass star in comparison to an isolated planet-moon system, results from a 2-body simulation for each moon orbital distance were also included in Tables 6.4, 6.5, and 6.6. The planet's spin rate in the 2-body simulations represented a tidally locked rotation around a 0.6 solar mass star. As such, the spin is the slowest of all the considered planets. It turned out that only the semimajor axis evolution differed among the 2-body models, so it was not necessary to show the corresponding 2-body simulation for every star mass.

As discussed in the previous subsection, moons with initial Io-like orbits and Saturn-like host planets spiralled into the planet after about 10 million years. Over that same time period, distortion torques were much less effective at evolving the semimajor axis for Io-like orbits around Jupiter-like hosts. Note that for a given star mass, the two planets were at equal distances from the star and they both started with a tidally locked rotation relative to the star. This results in approximately equal spin rates for the two planets. The relative effectiveness of the torques is then due to the difference in orbital distances for the satellites. While moons with a Jupiter host evolved much slower in comparison to a Saturn host, their inward migration was still noticeable. If I assume the inward migration rate will remain constant, a rough estimate would give a total lifetime of 200 million years for a Mars-like moon with an initial Io-like orbit and Jupiter-like host planet in the HZ of a red dwarf star. Since the actual evolution rate will increase with decreasing distance from the planet, a better estimate would be less than 200 million years.

Lifetime estimates for the inward spiral of all the Io-like and Europa-like moon orbit simulations are included in Figure 6.18. The figure shows results from simulations that started with circular moon orbits, which limits orbital effects of tidal heating and emphasizes evolution due to distortion torques. Simulations that started with eccentric orbits have shorter estimates for moon lifetimes. Estimates for Europa-like orbits are significantly

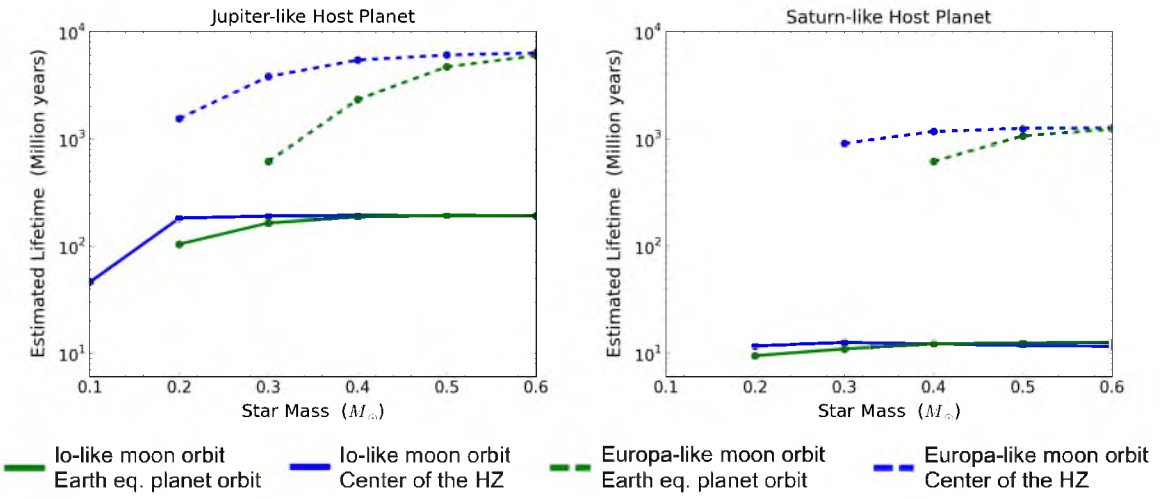

Figure 6.18. Estimated lifetimes from each 3-body simulation for the moon to completely spiral into the host planet.

longer than the Io-like orbits, around a maximum of one billion years for Saturn-like host planets and several billion years for a Jupiter-like host. Figure 6.18 indicates that the lifetime of moons at larger orbital distances are more sensitive to the planet's position in the HZ since they are more weakly bound to the planet and can experience greater influence from the central star. The sensitivity, however, becomes negligible for HZ distances around 0.6 solar mass stars.

One result that stands out in Tables 6.4, 6.5, and 6.6 is the difference between the conventional model for surface heat flux and my chosen model. In some cases, the conventional model is significantly higher while in others, it is slightly lower. The latter situation can be explained by noticing it only applies to results involving higher eccentricities. As mentioned in section 4.1, the conventional model can break down for high eccentricities while my chosen model is still appropriate at large values. For results involving lower eccentricities, h_{conv} is consistently higher than h. The difference in the two values scales down for the lowest eccentricities until the there is little difference between them. The greatest total difference was less than a factor of 2. The inconsistency between the two models is unfortunate, but as previously mentioned, the exact mechanisms of tidal dissipation are still poorly understood. Therefore, some difference between two separate tidal models is not surprising.

A similarity between the two tidal models is a direct dependence on the tidal Love number k_L and an inverse dependence on the dissipation factor Q. Higher values for Q decrease the heating estimates and represent lower dissipation rates in the moon. On the

other hand, higher values for k_L produce higher estimates for tidal heating and represent an increased susceptibility of the moon's shape to change in response to a tidal potential. This would also produce a larger acceleration due to the quadrupole moment of the moon, resulting in a shorter inward spiral towards the planet. Recent measurements of these two parameters for the Solar System planet Mars contain significant uncertainty (e.g. $k_L = 0.148 \pm 0.017$; $Q = 88 \pm 16$; from Nimmo and Faul (2013)). While these uncertainties can be considered in the simulation results for a single orbit, the long-term effects of varying k_L and Q would require each simulation to be repeated with the different values.

Besides the differences in tidal heating estimates, it is important to compare the 3-body results with the provided 2-body result for each moon distance in Tables 6.4, 6.5, and 6.6. The shaded rows indicate 2-body simulation results. In each case, the difference between the 3-body and 2-body models decreases with increasing star mass. In other words, the influence of the star can be seen to decrease as the HZ moves outward for higher mass stars. Other than these general similarities, I will discuss each table separately. A graphical representation of the surface heat flux in each table, as a function of stellar mass, is also provided in Figure 6.19.

6.4.1.1 Satellites at the Center of the HZ (Tables 6.4 and 6.5)

Taking into account that the hypothetical moons are in the HZ of the central star and continuing with the assumption that exomoons cannot be habitable above $h_{max} = 2W/m^2$, the table indicates that most of the moons would have the potential for habitability. The important exceptions to this have surface heat flux values highlighted in red. Not only are these flux values above h_{max}, they also represent a tidally evolved, steady state value from the 3-body simulations.

The highest surface heat flux involves an Io-like orbit around a Jupiter-like planet with a 0.1 solar mass central star. Note this was the only stable satellite orbit for a 0.1 $M_\odot$ star; therefore, this represents the tightest 3-body simulation (smaller star systems were considered, but none were stable). The effects of such a tight system can clearly be seen by the long-term excitation of the moon in comparison to an isolated planet-moon binary whose orbit was completely circularized during the same time period. It is interesting that the final eccentricity is not unreasonably large ($e = 0.035$), but it is more than enough to generate extreme heating when combined with the short orbital distance. The next star mass interval of 0.2 $M_\odot$ involved heating rates that almost seem manageable by comparison. Considering the surface fluxes are still about 3 times more than the most geologically active surface in

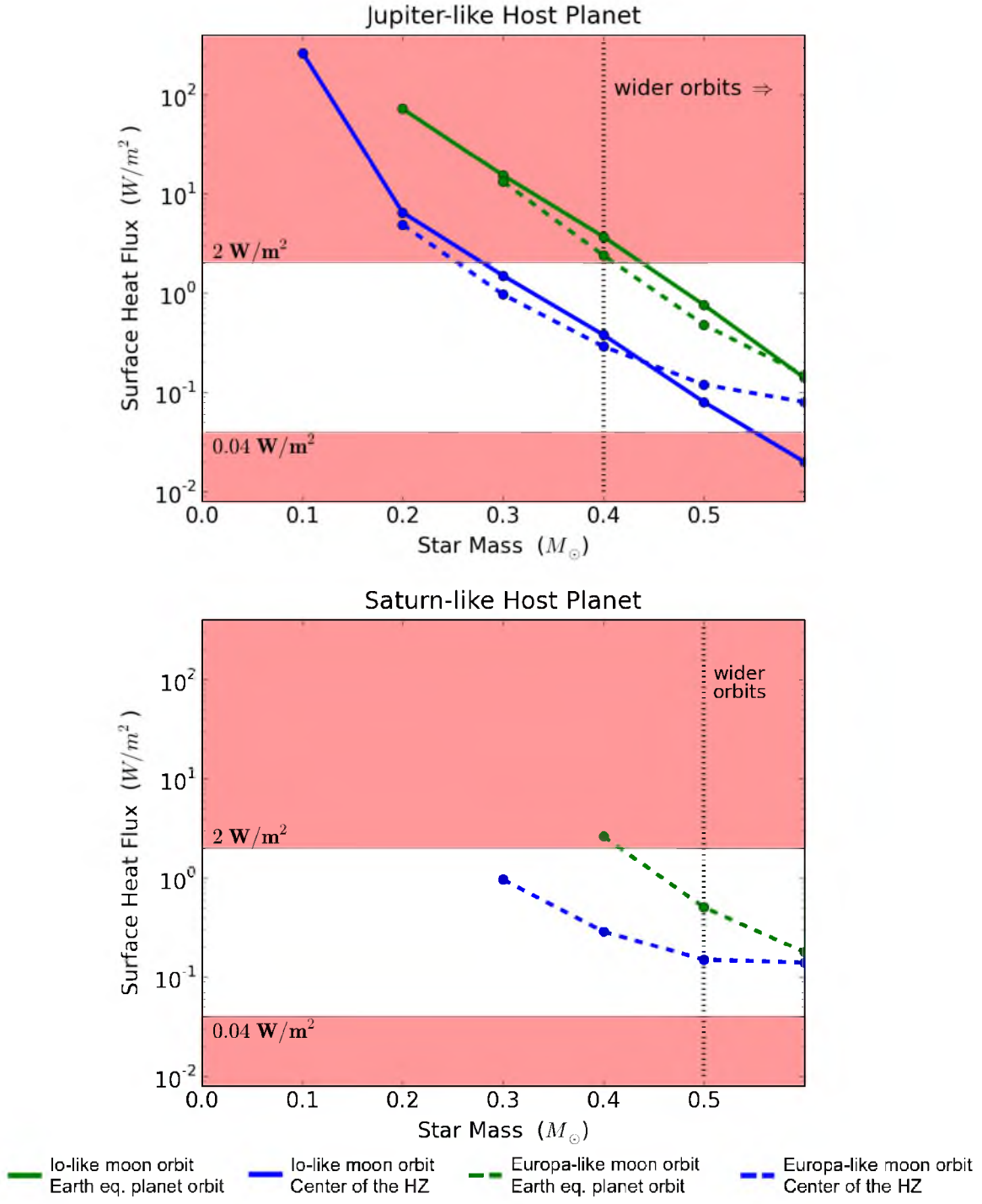

Figure 6.19. Graphical representations of the surface heat fluxes listed in Tables 6.4, 6.5, and 6.6. The red shaded regions represent surface heating values above $h_{max} \equiv 2\ W/m^2$ or below $h_{min} \equiv 0.04\ W/m^2$ for exomoon habitability. The dashed vertical lines at 0.4 and 0.5 $M_\odot$ are where Ganymede-like orbits (wider orbits) begin to be gravitationally stable.

our solar system, it seems reasonable to exclude them from habitability considerations as well. Notice that all systems with a 0.2 $M_{\odot}$ star had heating rates well above the maximum for habitability.

For a star mass of 0.3 $M_{\odot}$, there was mixed results in regards to heating for the different moon distances. Both planet models had stable Europa-like moon orbits and the two moons were comfortably below h_{max}. On the other hand, both the Jupiter and the Saturn-like host planets had Io-like moon orbits with surface heat flux below h_{max} for my model, but just above that for the conventional model. Given the inherent uncertainty in the tidal heating estimates, I do not think it is necessary to discuss which model gives the better estimate in an attempt to limit the potential for habitability for these systems. Instead, it is more relevant at this point to discuss the global flux (F_{glob}) observed in the center of the HZ. Excluding the previously mentioned case of extreme tidal heating, the global flux for all the satellites is about 110 W/m^2. Although the global flux does not lead to a direct estimate for the exomoon's surface temperature, a useful comparison can be made with the critical flux (F_{RG}) estimate of 269 W/m^2 for a runaway greenhouse in a Mars-mass exomoon (refer to subsection 2.5.2). Clearly, the habitability of exomoons at this location is not at risk based on runaway greenhouse conditions from the global energy flux. Since F_{glob} is less than half of F_{RG}, the surface temperatures are probably low. In this case, a high heating rate from tidal dissipation may serve beneficial in warming large bodies of surface water that may otherwise freeze.

Central star masses of 0.4 $M_{\odot}$ mark a cutoff for all exomoon habitability concerns based on intense tidal heating alone. This is due to the fact that all the hypothetical exomoons are comfortably below h_{max} at this point. This observation also applies to the now available wide orbits (Ganymede, Titan, and Callisto-like) who have retained their initial eccentricity due to the relatively small energy dissipation. As already discussed in reference to the previous tidal evolution plots, surface heat flux for the wide orbits do not represent steady state values achieved through tidal evolution. This fact can be represented in Tables 6.4 and 6.5 by comparing the 3-body and 2-body results. Notice that there is little to no difference for any of the wide orbits, which suggest that the star had essentially no perturbing influence on the moon's tidal evolution at these distances. On the other hand, the star did influence the short orbit moons (Io and Europa-like distances). However, the influence can be seen as a benefit in promoting surface activity in the exomoons rather than any kind of restriction for habitability.

As a final observation, it is interesting that there does not seem to be a large difference

in the final satellite heating rates between the two planet models and a given star mass. This only seems to be the case for short orbits since the wide orbits do not really evolve from tidal effects on these timescales. For example, with a star mass of 0.3 $M_{\odot}$ and an Io-like moon orbit, the moon around Jupiter had $h = 1.49W/m^2$. In comparison, the moon around Saturn had $h = 1.56W/m^2$. Other examples have even less percent difference with some matching perfectly. The same cannot be said for the orbital elements, yet these parameters would have to vary in order to compensate for the unique physical characteristics of the planet. Given the physical differences and the corresponding difference in orbital distances for the moons, I did not expect the tidally evolved heating rates to be so similar.

The 3-body simulation results involving the center of the HZ helped determine my second location for exploration inside the zone. Considering that the majority of the satellites had heating rates below h_{max} and that the global flux was well below the critical flux for a runaway greenhouse, it was clear that the next round of simulations should involve the inner HZ.

6.4.1.2 Earth-equivalent Satellite Distances (Table 6.6)

For this second round of 3-body simulations, I essentially took the prior 3-body systems and moved the planet-moon binary closer to the star. By decreasing the orbital distance from the star, the Hill radius of the planet also decreased. This led to a reduction in stable satellite systems, especially for wider orbits.

Once again there was little change to the wide orbits over the 10 million years of simulated time, with the apparent exception of two systems. The Ganymede-like and Titan-like orbital distances around Jupiter actually show a significant increase in heating compared to the isolated 2-body simulations. Notice that these values are not highlighted in red since the heating rates do not represent tidally evolved, steady state values. This specific observation was already discussed near the end of section 6.4 in which I referred to long-term behaviors shown in Figures 6.13(a) and 6.14. In summation, these systems are near instability and are more sensitive to the chosen initial condition of the simulation. The high surface heat flux is a consequence of the increased eccentricity that resulted from an initial scattering at the beginning of the simulation. When I repeated the simulations with an initially circular orbit, the same high heating rates were not reproduced. Therefore, they are nothing more than artifacts of my simulation creation process. These simulations do show that after the systems have settled from the initial scattering, the star does not cause any additional long-term excitation.

For short orbit moons, the analysis of surface heating effects on habitability is made

simple. All stable satellite systems involving a central star of mass 0.4 $M_{\odot}$ and below experience surface heating greater than h_{max}. This is true for estimates from both tidal heating models. More importantly, since the surface heat fluxes represent tidally evolved, steady state values, the heating has the potential to be maintained for extended periods of time. Also, there is not a large difference in final heating rates between specific moon orbits around Jupiter or Saturn-like host planets, as was seen for systems in the center of the HZ.

In regards to global flux, extreme tidal heating was the only cause for two satellites to be above the critical flux of 269 W/m^2. In those situations, the extreme heating was already enough to rule them out for potential habitability. The rest of the satellites are comfortably below the critical flux, leaving the surface heat flux as my primary consideration for exomoon habitability in these systems. At least, that is the case for the chosen physical parameters. An interesting future study would be to vary parameters in regards to the global flux and then investigate changes to the tidal evolution of each system.

CHAPTER 7

4-BODY SIMULATIONS

The motivation for the 4-body systems was to test if an orbital resonance with a second moon would continue to excite significant levels of heating in the innermost moon, in addition to the influence of the star. An artistic representation of one of my 4-body systems is shown in Figure 7.1. In constructing the 4-body systems, I used the groundwork already completed with the 3-body simulations. Systems involving the center of the HZ were used since the satellites had lower surface heating than those at Earth-equivalent distances. I considered all stable 3-body systems and tried adding an additional Mars-like outer moon.

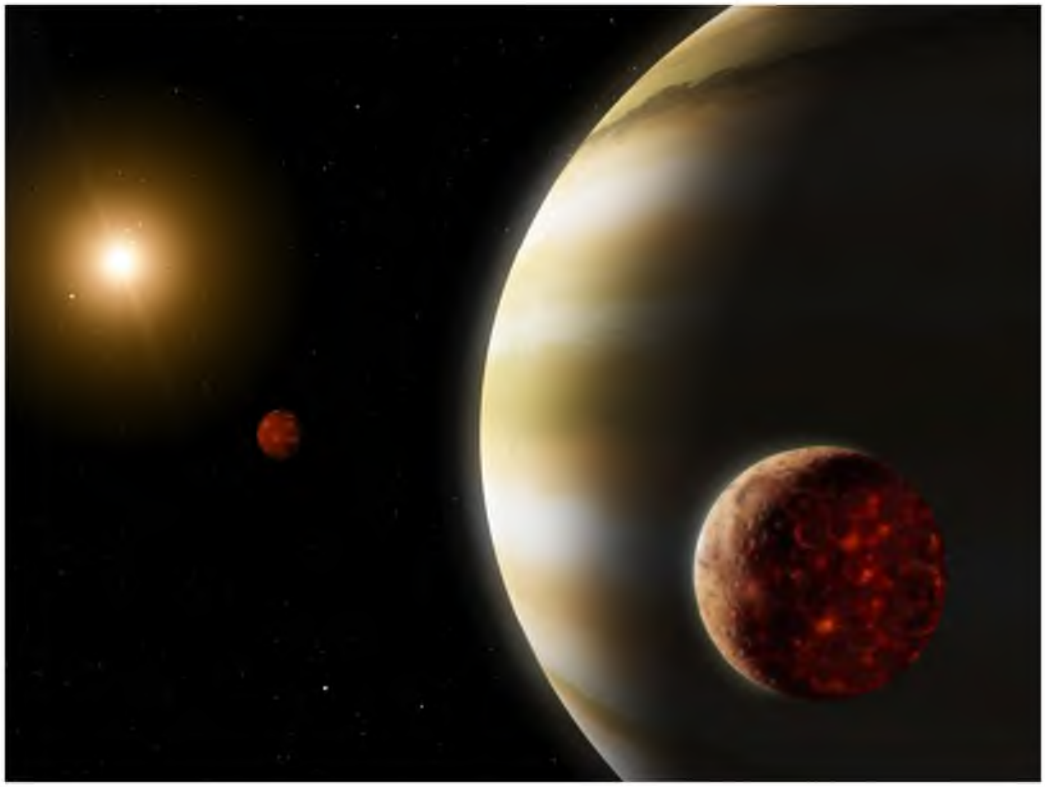

Figure 7.1. Artistic representation of two Mars-like moons around a Jupiter-like giant planet.

The second moon was placed at specific distances corresponding to resonant orbits (i.e. an outer orbital period that is an integer multiple of the inner orbital period). Since I am assuming equal masses for both moons, the outer moon's semimajor axis is related to the inner moon as

$$a_{outer,n} = n^{2/3} a_{inner}, \qquad n = 2, 3, 4, \ldots \quad , \tag{7.1}$$

where n in this case represents the ratio of the outer orbital period and the inner orbital period ($n = P_{outer}/P_{inner}$).

For this study, it was necessary to use a reduced stellar mass range than the one used in the 3-body study. I considered the range $M_{star} \leq 0.5 M_{\odot}$, which specifically correspond to red dwarf stars. The reason for the reduced range was the computational processing time required for each 4-body simulation. Each system required more than 22 days of continuous computation to show an acceptable sample for the system's long-term behavior. Therefore, it was necessary to limit the total number of simulations by reducing the considered star mass range.

7.1 4-body Stability Considerations

With the 4-body simulations built from stable 3-body systems in the center of the HZ, this gave me 20 systems to consider within the chosen star mass range. Following Equation (7.1), only 9 of the 20 systems could support a second (outer) moon within the previously determined Hill stability limit ($a_{outer} \lesssim 0.4 R_{Hill}$). A few of the 9 candidate systems could also support wider orbital resonances of $n = 3$ and above. However, several of these systems became unstable after an extended period of time due to the mutual interaction of the moons. A summary of the stable 4-body systems is provided in Table 7.1, which is provided as a comparison to the original 3-body systems. A complete listing of all the performed 4-body simulations is shown in Table 7.2. Notice in this table how the lower-mass Saturn-like host planet has a noticeably reduced stability region in comparison to the Jupiter-like host at the same distance from the star.

7.2 Results

Results for the extended 4-body simulations are displayed in a manner similar to the 3-body results using tidal evolution plots (surface heat flux as a function of time). The plots are contained in Figures 7.2 through 7.6. Since the outer moon was treated as a point mass with no tidal interactions during the simulations, the tidal evolution plots can only include results for the inner moon. This restriction is not particularly important since

Table 7.1. 4-body Hill stability summary, as compared with Table 6.1. The shaded cells represent stable 3-body simulations. The J symbol means a second moon was stable around a Jupiter-like planet, an S for a Saturn-like planet. The symbol "-" represents an unstable satellite system.

Planet Orbit in Center of HZ						
Star Mass	Planet Distance (AU)	Inner Moon Semimajor Axis				
		5.9 R_P	9.6 R_P	15.3 R_P	21.0 R_P	26.9 R_P
0.1 $M_\odot$	0.051	-	-	-	-	-
0.2 $M_\odot$	0.11	-	-	-	-	-
0.3 $M_\odot$	0.16	J	-	-	-	-
0.4 $M_\odot$	0.22	J	-	-	-	-
0.5 $M_\odot$	0.30	J, S	J	-	-	-

the physically identical outer moon will always experience lower heating rates under stable conditions.

One benefit to building upon the 3-body models is that their results can be compared to the 4-body models. Included in each tidal evolution plot is the corresponding 3-body evolution for the inner moon. This serves as a comparison to determine the influence of the outer moon. Considering that my intent was to develop resonant conditions between the inner and outer moon, included to the right of each tidal evolution plot is the ratio between the outer and inner moon orbital periods (P_{outer}/P_{inner}). An integer value in these plots indicates resonant conditions between the two moons.

7.3 Discussion

Comparing the 4-body and 3-body curves in Figures 7.2 through 7.6 shows an inconsistent and sometimes chaotic evolution for the inner moon when a second Mars-like moon is added to the system. In several instances, the inner moon experiences periods of excited heating that lasts for about a million years. When comparing the timing of these events to the ratio of the orbital periods, it is clear that they do not correlate to resonance with the outer moon. A good example for this is represented in Figure 7.3(c), where the inner moon undergoes a noticeable increase in surface heating starting at 2 million years and ending a little less than a million years later. The corresponding ratio of orbital periods during that time was about 3.9. Roughly 3 million years later, the inner and outer moons develop a 1:4 resonant configuration. However, the heating of the inner moon shows no discernable change in behavior as a response. Similar behavior is observed in the other simulations where temporary resonance does not directly excite tidal heating in the inner moon.

Table 7.2. A more detailed 4-body stability summary. Included are all systems that had potential for multiple moons based on Hill stability alone ($a_{outer} \lesssim 0.4 R_{Hill}$). The 'Extended Stability' column represents instability caused by the mutual interaction of the two moons.

Jupiter-like Host Planet			
Star Mass	Inner Moon Orbit	Resonance Mode for Outer Moon (P_{outer}/P_{inner})	Extended Stability
0.3 $M_\odot$	Io-like	2	yes
		3	yes
0.4 $M_\odot$	Io-like	2	yes
		3	yes
		4	yes
	Europa-like	2	no
0.5 $M_\odot$	Io-like	2	yes
		3	yes
		4	yes
		5	yes
	Europa-like	2	yes
		3	yes

Saturn-like Host Planet			
Star Mass	Inner Moon Orbit	Resonance Mode for Outer Moon (P_{outer}/P_{inner})	Extended Stability
0.3 $M_\odot$	Io-like	2	no
0.4 $M_\odot$	Io-like	2	no
		3	no
0.5 $M_\odot$	Io-like	2	no
		3	yes
		4	yes
	Europa-like	2	no

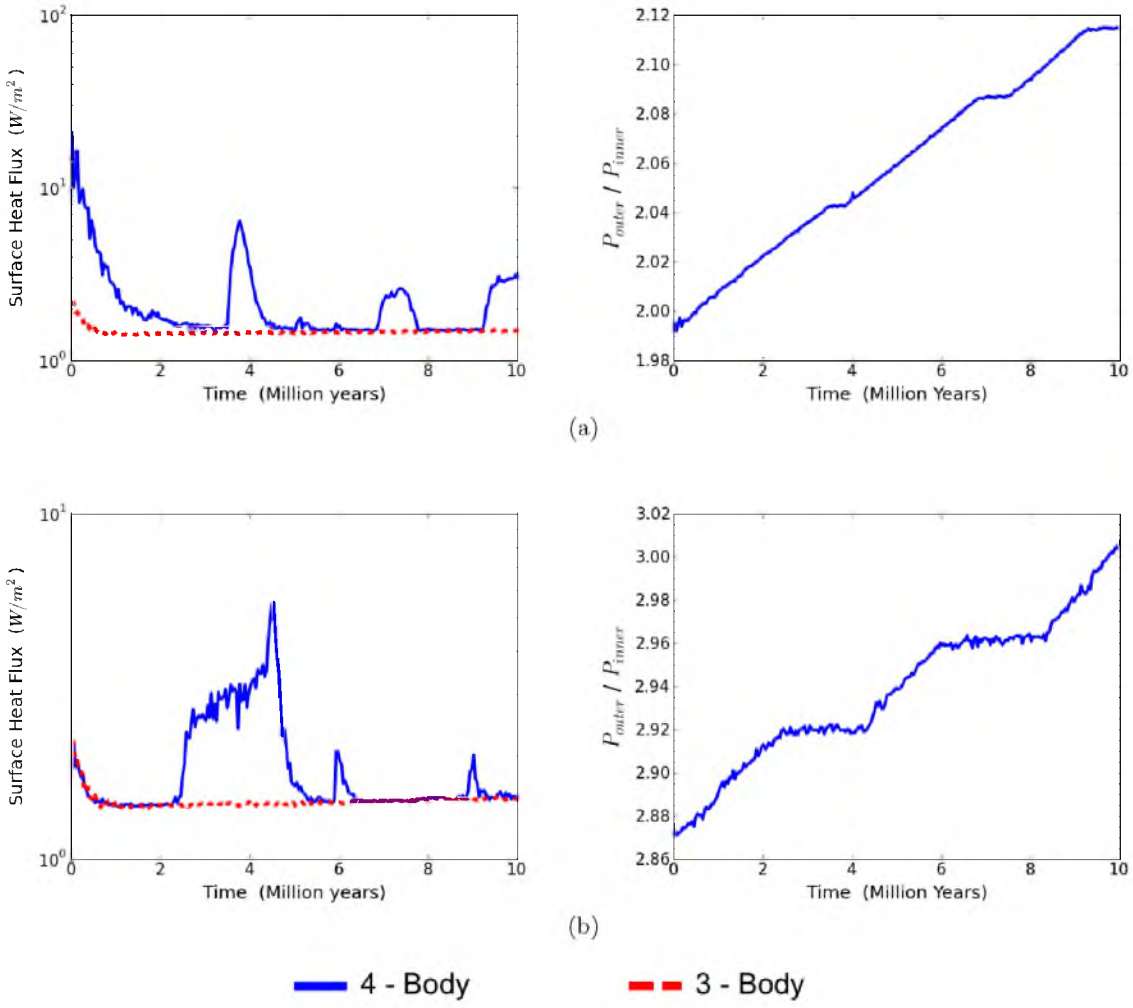

Figure 7.2. Jupiter-like host planet with two moons and a 0.3 solar mass central star. The inner moon started with an Io-like orbit. Surface heating plots only show results for the inner moon. (a) Attempted 1:2 resonance. (b) Attempted 1:3 resonance.

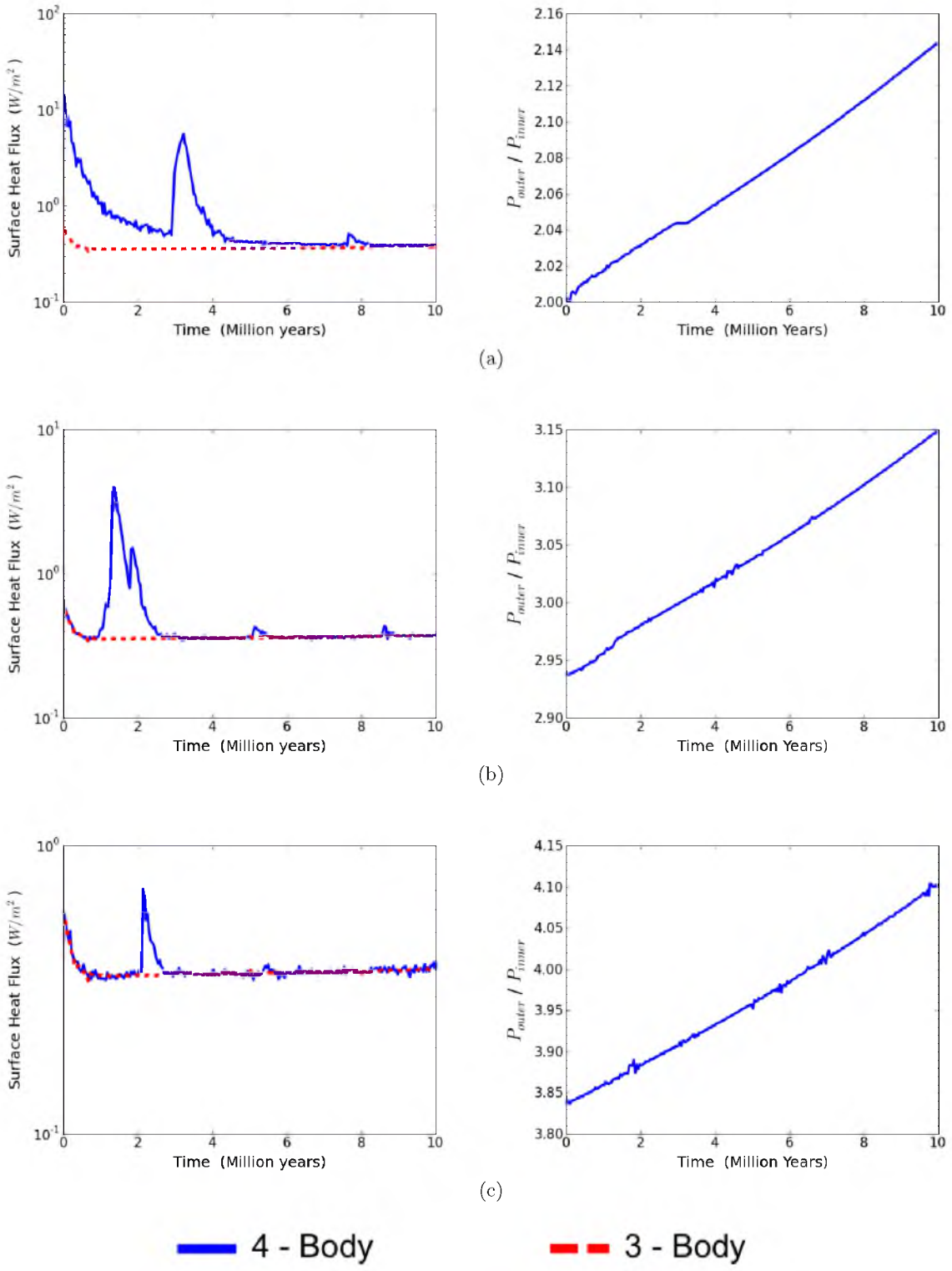

Figure 7.3. Jupiter-like host planet with two moons and a 0.4 solar mass central star. The inner moon started with an Io-like orbit. Surface heating plots only show results for the inner moon. (a) Attempted 1:2 resonance. (b) Attempted 1:3 resonance. (c) Attempted 1:4 resonance.

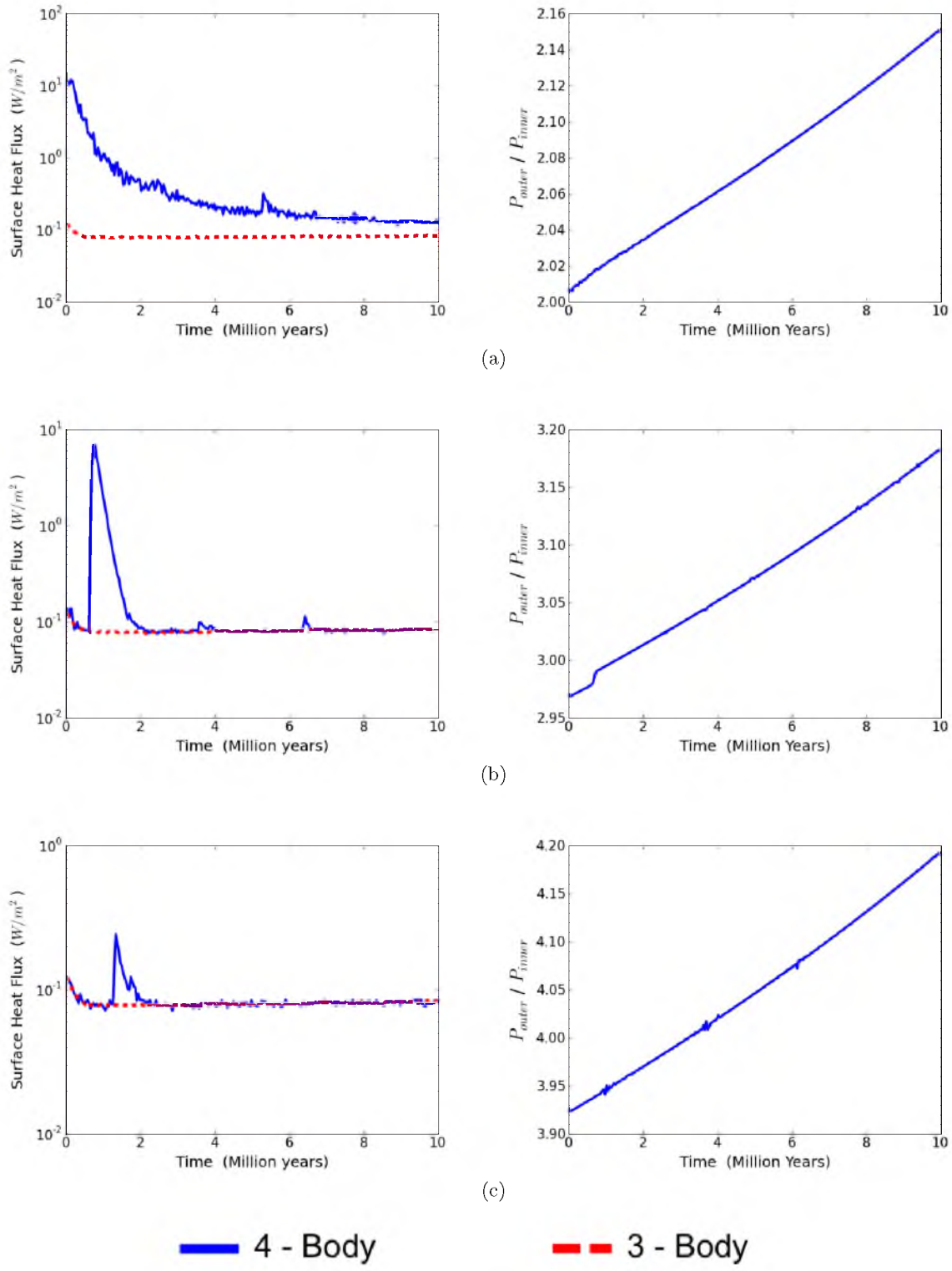

Figure 7.4. Jupiter-like host planet with two moons and a 0.5 solar mass central star. The inner moon started with an Io-like orbit. Surface heating plots only show results for the inner moon. (a) Attempted 1:2 resonance. (b) Attempted 1:3 resonance. (c) Attempted 1:4 resonance.

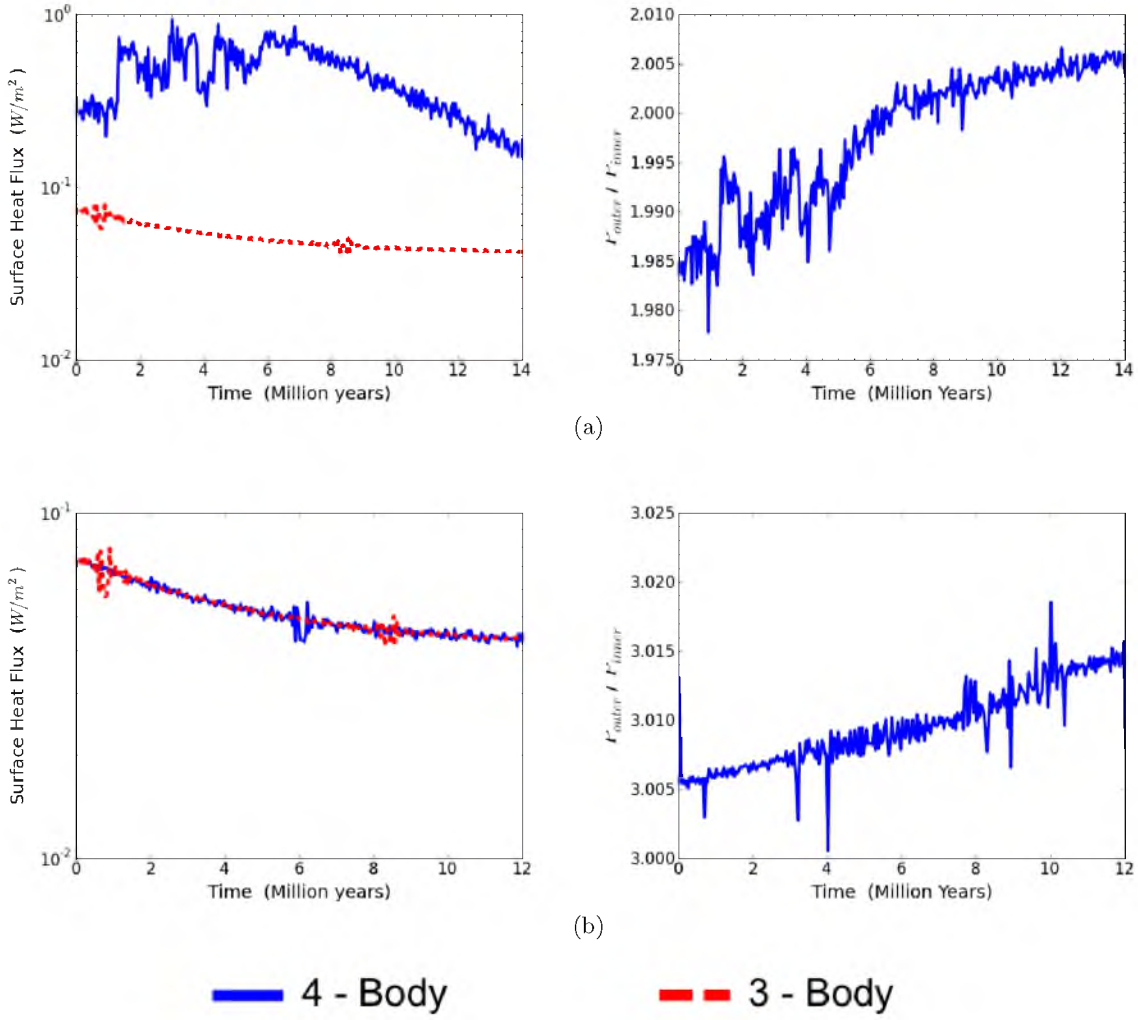

Figure 7.5. Jupiter-like host planet with two moons and a 0.5 solar mass central star. The inner moon started with a Europa-like orbit. Surface heating plots only show results for the inner moon. (a) Attempted 1:2 resonance. (b) Attempted 1:3 resonance.

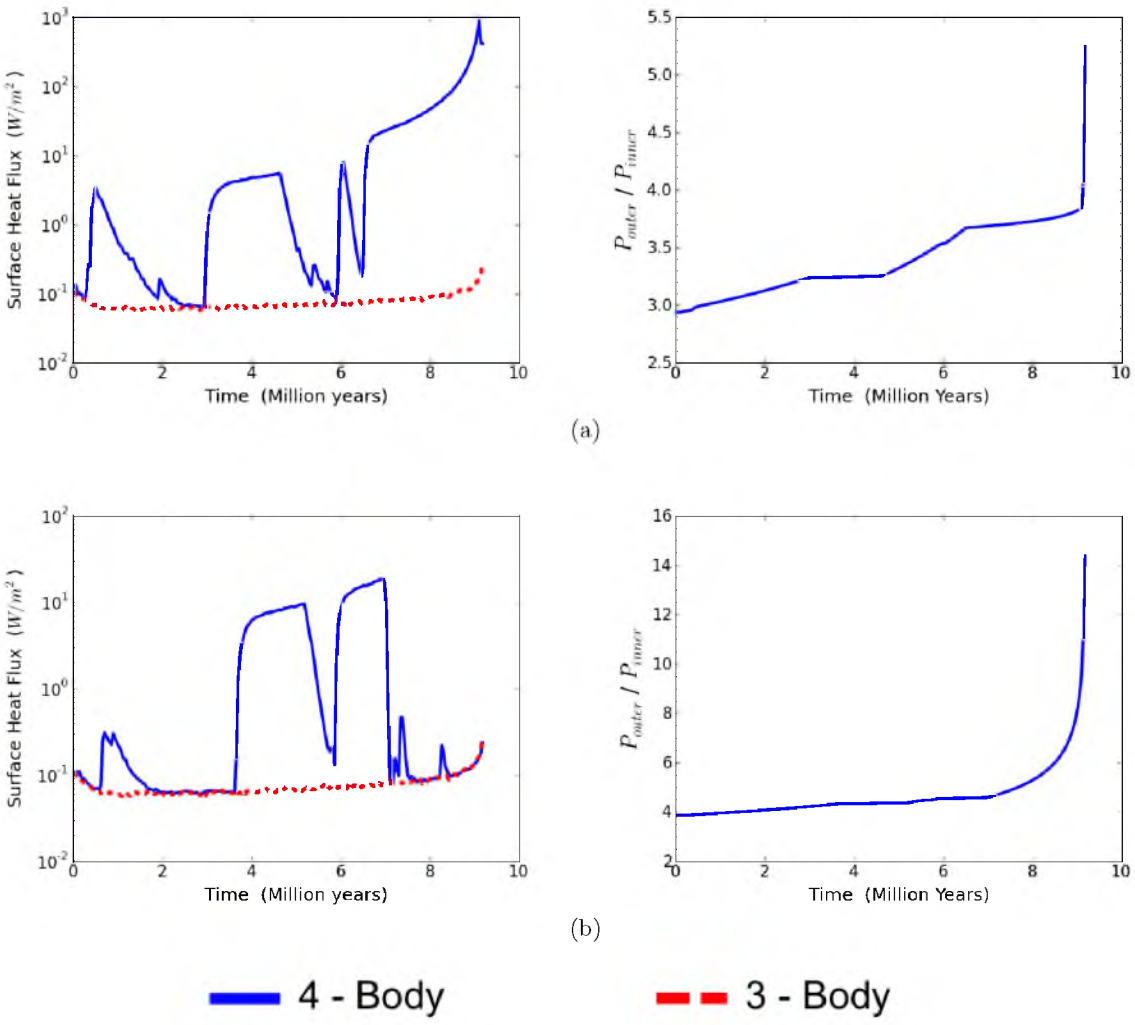

Figure 7.6. Saturn-like host planet with two moons and a 0.5 solar mass central star. The inner moon started with an Io-like orbit. Surface heating plots only show results for the inner moon. Note that for these systems, the simulations terminated early when the inner moon spiraled into the host planet. A 1:2 resonance was not included due to early system instability which ejected the outer moon. (a) Attempted 1:3 resonance. (b) Attempted 1:4 resonance.

The steadily increasing slopes of the period ratio curves (right plots) suggests that the two moons are consistently moving away from each other. Because no tidal interactions are considered for the outer moon, its semimajor axis is expected to remain roughly constant. On the other hand, the inner moon's semimajor axis would be expected to decrease as a consequence of tidal dissipation and distortion torques. Since most of the systems involve an Io-like orbit for the inner moon, the rate of change in semimajor axes would be significant based on the 3-body evolutions. This helps to explain why the two moons do not settle into resonant orbits. The spin and tidal evolution are effective enough at changing the massive inner moon's orbit that temporary resonance effects are insubstantial in comparison. In addition, the central star also has a small, but disruptive influence on the orbits.

An inward evolving semimajor axis explains why the slopes of the period ratio curves are positive. As the inner moon moves closer to the planet, it also moves away from the outer moon. In this regard, the two initially stable systems involving a Saturn-like planet would expect a relatively rapid inward spiraling of the inner moon. Their evolutions are shown in Figure 7.6 where the extremes in tidal heating are a reflection upon their tightness in comparison to all other considered systems. The rapid increase in period ratios around 9 million years represents a drastic decrease in semimajor axis as the inner moon gets closer to the planet. The simulations were terminated soon after when the distance between the moon and planet became too small.

While the inconsistent periods of excited tidal heating do not directly correspond to orbital resonance, they do correlate to the shapes and relative orientations of the moon orbits. The non-zero heating rates indicate that the inner moon maintains a small eccentricity relative to the planet. The outer moon also developed a noncircular orbit. Consequently, each moon has points of closest approach and furthest approach to the planet (pericenter and apocenter, respectively). Since these satellite systems involve tightly-packed moons, the relative orientation of their orbits can be important. Figure 7.7 illustrates the effects of orientation on two eccentric moon orbits. The orbital element that defines the angular location of the pericenter is the argument of pericenter (ω) which ranges in value from 0° to 180°. The inline orbits in Figure 7.7(a) would have the same arguments of pericenter ($\omega_{out} - \omega_{in} = 0°$). With this configuration, the minimum possible distance between the two moons occurs when they are both at pericenter. If the outer orbit is rotated by 180 degrees, as in Figure 7.7(b), then the arguments of pericenter would differ by 180 degrees ($\omega_{out} - \omega_{in} = 180°$). In this case, the minimum distance occurs when the inner moon is at apocenter and the outer moon is at pericenter. Notice that the minimum possible distance

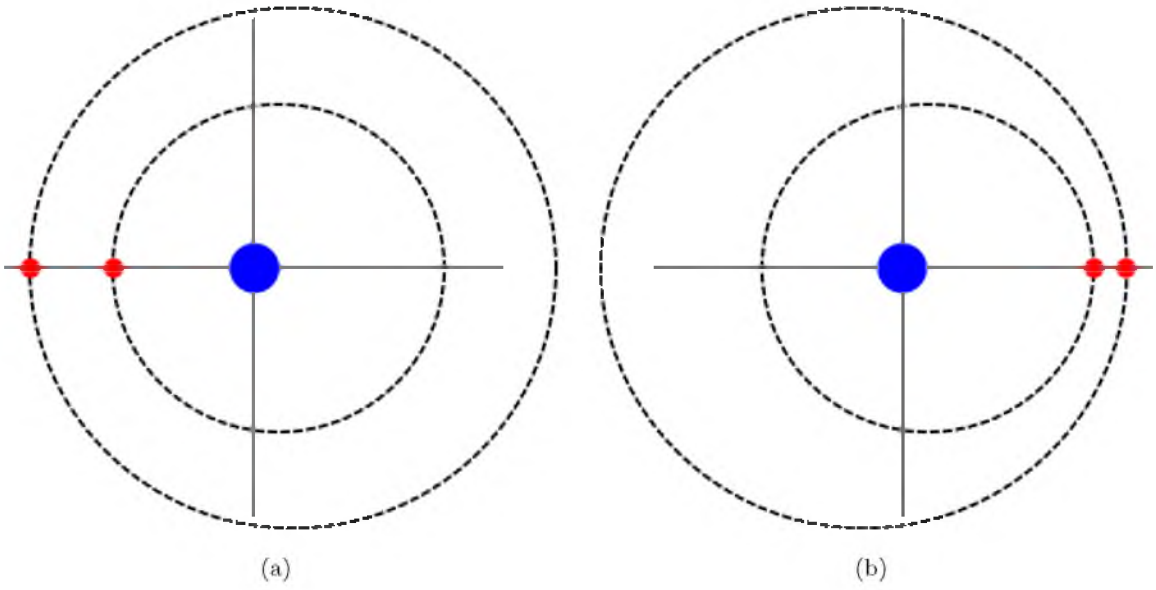

Figure 7.7. Illustration showing how relative orientation changes the minimum distance between two satellites. The large blue disk represents a planet; small red disks are moons. Both orbits have an eccentricity of 0.15. The semimajor axes are consistent with a 1:2 resonant configuration. The planet is located at a focus for each orbit. (**a**) Inline orbits with $\omega_{out} - \omega_{in} = 0°$. (**b**) The inner orbit is the same, the outer orbit was rotated 180 degrees so that $\omega_{out} - \omega_{in} = 180°$.

between the two moons is shorter in the latter example. The difference in minimum distance for the 4-body simulations is much less than the exaggerated example of Figure 7.7, but even a small difference can lead to noticeable perturbations for moons with tight orbits.

Since the orbit of a single moon is perturbed by the second moon and the star, its argument of pericenter cannot be expected to remain constant, even on timescales relating to the orbital period.[1] As previously discussed, the orbits do not involve strictly Keplerian motion. The short-term behavior of ω in a 4-body simulation involves sinusoidal oscillations with a period equal to about one orbital period and an amplitude of a few degrees. There is also a slow change of about one degree per day in the mean value. In order to explain the excited heating rates for the inner moon, the important consideration is the difference in arguments of pericenter between the two moons. For ease of reference, I define $\omega_{diff} \equiv \omega_{out} - \omega_{in}$, where ω_{diff} can range from -180° to +180°.

The 4-body simulations began with $\omega_{diff} \sim 0°$. This difference was maintained on

[1]On longer timescales, an isolated moon would still undergo precession of its argument of pericenter, as described by general relativity.

average during the simulations. The maximum deviations from the average did not remain constant. The deviations are defined as $\omega_{abs} \equiv |\omega_{out} - \omega_{in}|$ which can range from 0° to 180°. The two extremes for ω_{abs} are represented in Figure 7.7. When ω_{abs} is high, the two moons are more likely to interact at reduced distances and cause greater mutual scattering. Enhanced scattering events of this type should reflect an exchange of orbital angular momentum.

Figure 7.8 is a representative example for the connection between increased tidal heating and the difference in arguments of pericenter. Figure 7.8(a) is the same tidal evolution plot shown in Figure 7.2(a). Figure 7.8(c) shows how the maximum of ω_{abs} changes with time. The actual distribution of ω_{diff} is included in Figure 7.8(e), with the standard deviation in Figure 7.8(f). A comparison of these figures shows that differences above zero do not immediately excite the heating rates, but increases in the difference are always accompanied by increased heating.

Figures 7.8(b) and 7.8(d) are included to represent the exchange in orbital angular moment during the enhanced scattering phases. The inner moon's orbit averaged eccentricity fluctuates in accordance with its tidal heating; however, the overall behavior is similar to the 3-body curve. The semimajor axis evolution for the inner moon appears to be unaffected by the presence of the outer moon. Notice that a temporary increase in the eccentricity of the inner moon always corresponds to a decrease in eccentricity or semimajor axis (or both) for the outer moon. These results confirm the additional interactions between the two moons during periods of enhanced heating for the inner moon. It is worth noting that the orbital elements of a given orbit continually fluctuate in these many-body systems. A possible extension to this study could involve a closer inspection of specific interactions over single orbits, just before the periods of increased activity. The investigation may reveal short period resonances between the moons which could explain the specific mechanisms causing the enhanced activity. This type of analysis cannot be performed from the existing simulation data since it lacks the necessary output resolution to accurately consider detailed interactions over single orbital periods.

At the beginning of this chapter, I explained that a primary interest in the 4-body simulations was to test if an outer moon could help *maintain* higher heating rates in the inner moon. I was looking for long-term excitation that lasted well after the systems settled in from their initial creation conditions. In that sense, the temporary periods of increased heating are relatively short term. In many of the simulations, the heat flux changes by an order of magnitude, sometimes reaching levels above h_{max}. Since the occurrence rates

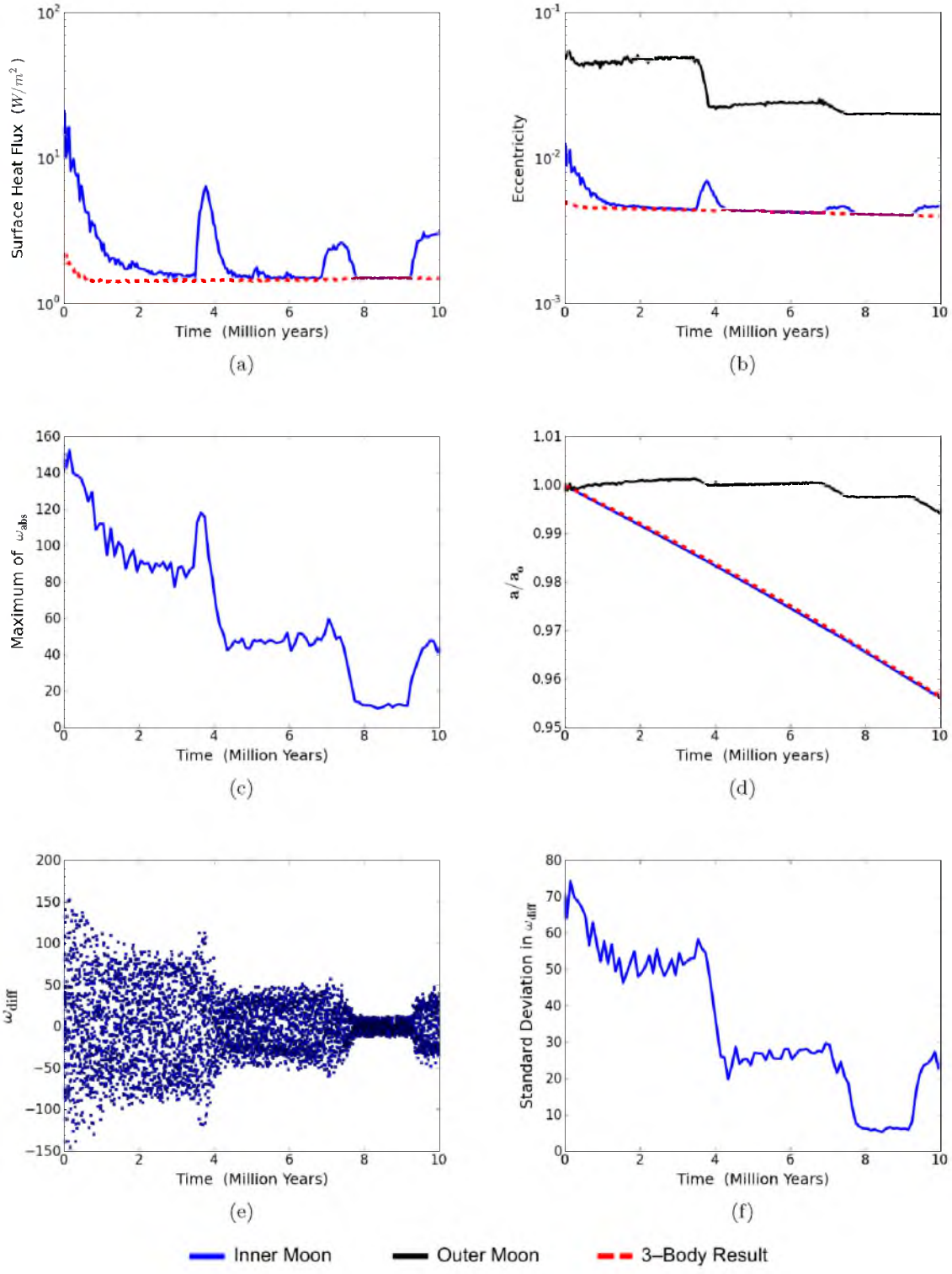

Figure 7.8. A typical example for the overall evolution of a 4-body system. This particular system is represented in Figure 7.2(a).

for temporary excitation are inconsistent, it is hard to predict their long-term effects on habitability. If I look past the temporary excitations, then the overall tidal evolutions do not deviate significantly from the 3-body simulations. Figures 7.4(a) and 7.5(a) appear to show the potential for additional heating; however, the apparent increase is simply an artifact of the simulation creation process. Similar to examples of 2-body and 3-body comparisons, the very beginning of these particular simulations was a little more chaotic than the others. The result was that the inner moon quickly developed a slightly larger average eccentricity in the 4-body system than it did in the 3-body system. An indication for this is the small fluctuations in the average surface heat flux (blue line) as compared to the 3-body curve (dashed red line). In addition, the overall separation between the two curves is decreasing with time and will eventually line up as the tidal heating in the inner moon works to remove the extra initial eccentricity.

CHAPTER 8

DISCUSSION AND FUTURE WORK

8.1 Summation of Key Points

For this dissertation, I have performed a computational exploration into specific characteristics of theoretical exomoon systems. This study has focused on satellite systems in the habitable zone (HZ) of red dwarf stars. Interest in this particular stellar mass range stemmed from their significantly reduced HZ distances in comparison to Sun-like stars. For a planet-moon binary in the HZ of a low-mass star, the close proximity of the star presents dynamical restrictions to the stability of the moon, forcing it to orbit close to the planet to remain gravitationally bound. At short orbital distances, tidal heating and tidal torques between the planet and moon become more substantial. The relatively close star can also influence the long-term tidal evolution of the moon by continually exciting its orbit through gravitational perturbations. The question this dissertation has attempted to answer addresses at what stellar mass does an exomoon need to orbit so close to the planet that tidal interactions render an otherwise habitable moon, uninhabitable. Challenges to habitability result from frequent resurfacing of the planet or an induced runaway greenhouse effect.

Several tidal models exist which are appropriate for evaluating the tidal evolution of an isolated planet-moon binary. However, satellite systems in the HZ of low-mass stars are certainly not isolated due to the nearby central star. Therefore, a tidal model which simultaneously considers both tidal and dynamical effects is required. Utilizing an appropriate tidal model, I created a computational program for calculating self-consistently the tidal, spin, and dynamical evolution of a many-body system. With this new program, I performed an investigation into the effects of tidal evolution on exomoon habitability in low-mass star systems.

At the time of this writing, no moon outside the Solar System has been detected. Exomoon formation theory suggests that massive exomoons around giant planets are plausible, and searches are currently underway to achieve the first exomoon detection. Considerations

of formation theory, detectability, and constraints on terrestrial world habitability suggest a preferred mass regime of 0.1 to 0.2 earth-masses for habitable moons that can be detected in the near future. Since little information is known about the internal structure and composition of extrasolar planets, objects in the Solar System provide the best guide for hypothesizing the dynamics of extrasolar bodies. Following these consideration, I modeled hypothetical exomoon systems after existing solar system bodies. The two largest planets in our Solar System were used as templates for extrasolar planets in the HZ of low-mass stars. The physical characteristics of Mars were used to model massive exomoons around the giant planets, since the mass of Mars lies in the preferred mass regime for potentially habitable and detectable exomoons.

8.2 Constraints on Exomoon Habitability

• M dwarfs with masses $\lesssim 0.2\ M_{\odot}$ cannot host habitable exomoons within the stellar habitable zone.

As predicted for planets in the habitable zone of low-mass stars, constraints from gravitational stability require massive exomoons to orbit close to their host planet. Specific limits on orbital distances depend on the stellar and planetary masses. Considering planets up to one Jupiter mass, stars with masses $\lesssim 0.2\ M_{\odot}$ can support only one Mars-like satellite out to distances of $\sim 10\ R_P$ (Europa-like orbits). Though these systems are gravitationally stable, the close proximity to the star continually excites non-zero eccentricities in the moon's orbit. With limited orbital distances, tidal heating in the moon was significant, resulting in surface heating rates well above the proposed limit of $h_{max} = 2\ W/m^2$. Considering the excessively high heating estimates, these systems are unlikely to host habitable exomoons.

Implications extend beyond stellar mass limits for exomoon habitability. These results suggest for this specific mass range that exomoons inside the HZ are most likely not habitable. This confirms that exomoon habitability is more complex than traditional definitions for planet habitability which are based primarily on irradiation from a host star. Consequently, massive moons in the stellar HZ are not necessarily habitable by definition. An expanded model is necessary when considering exomoon habitability (e.g. Heller and Barnes 2013). Since the intense heating rates in the hypothetical exomoons are maintained by stellar perturbations, moving the host planet slightly outside the HZ should reduce the stellar influence. In this case, a balance between higher heating rates and lower surface temperatures could enable habitability in a moon that would otherwise

be considered uninhabitable.

• **In the mass range 0.2 $M_{\odot} < M_{star} < 0.5\ M_{\odot}$, perturbations from the central star may continue to influence the long-term tidal evolution of exomoons in the stellar habitable zone.**

For stellar masses $\gtrsim 0.3\ M_{\odot}$, the distinction for habitable exomoons became less defined when based primarily on tidal evolution. The hypothetical exomoon simulations suggest that the host planet's location in the HZ has to be taken into consideration. Results from simulations involving Earth-equivalent distances (the inner HZ) show that M dwarfs with masses $\lesssim 0.4\ M_{\odot}$ promote surface heating beyond an acceptable limit for habitability. In comparison, planetary orbits in the center of the HZ are within the established limits for habitability. Since a star's influence on a moon decreases with distance, so does its ability to excite higher heating rates. Therefore, this result for the center of HZs can be applied, by extension, to outer HZs.

It should be noted that my assumed maximum limit for habitability ($h_{max} = 2\ W/m^2$) is based on a single example – the solar system moon Io. There is little doubt that Io does not support a habitable environment in its current state. However, there is no direct evidence that a Mars-sized or even an Earth-sized exomoon could not remain habitable given the same internal heating rate. This is especially true considering the uncertainty in the exact mechanisms of tidal dissipation and the efficiency of plate tectonics in terrestrial bodies. It is possible that a higher heating rate for a water-covered world located near the outer region of the HZ could simply act to warm surface water that would otherwise freeze. For these reasons, h_{max} was used more as a unit of comparison than a hard cutoff for habitable exomoons. With this consideration and treating the HZ as a whole, perturbations from a central star may continue to have deleterious effect on exomoon habitability up to $\approx 0.5\ M_{\odot}$.

In contrast to the possibility of intense tidal heating, perturbations from the star may actually have a positive influence on the habitability of exomoons. Figure 6.19 shows many surface heating rates below h_{max}, yet above the proposed minimum for habitability ($h_{min} = 0.04\ W/m^2$). These results suggest that satellite systems around stars in this mass range would need to be considered on a case-by-case basis depending on the planet mass and the specific location in the HZ.

• **Considerations of global energy flux do not restrict exomoon habitability for star masses above 0.2 $M_{\odot}$**

The bulleted conclusions thus far are in agreement with predictions made by Heller (2012) who followed considerations of energy flux and gravitational stability. This study,

which focused on tidal evolution, has verified those predictions using a tidal model that considered both N-body interaction and tidal evolution. Similar considerations for energy flux were incorporated within this study with the global averaged flux (F_{glob}) listed in Tables 6.4, 6.5, and 6.6. Compared to the critical flux of 269 W/m^2 for a runaway greenhouse on a Mars-mass satellite, the 3-body global flux results support the conclusion that star masses $\lesssim 0.2\ M_{\odot}$ are unlikely to host habitable exomoons. Above that mass, exomoon habitability was not constrained by global energy flux.

• Torques due to spin and tidal distortion between the planet and moon can result in rapid inward spiraling of a moon for orbital distances $\lesssim 6\ R_P$.

In specific simulations involving a Saturn-like host planet and Io-like ($a \sim 6\ R_p$) moon orbits, distortion torques resulted in the complete inward spiral of a moon in less than 10^7 years. The inward migration was connected to the assumption that the giant host planet was tidally locked to the star. While the orbital decay rate was slower for more massive Jupiter-like host planets, a conservative estimate for the maximum lifetime of Io-like moon orbits was only 200 million years. Compared to the geological age of the Earth, this is a short lifespan. Assuming a Mars-like moon with an Io-like orbit was habitable to begin with, implications for the development of life may be considerable.

• Stability constraints and tidal interactions make sustained orbital resonances between two massive moons unlikely in planetary systems around low-mass stars.

Considerations for gravitational stability suggest that multiple massive satellites around Jupiter-mass planets (or lesser mass) will not be found in star systems less than 0.3 $M_{\odot}$. Simulations involving a second outer moon were meant to explore long-term resonance effects between two massive moons. Since the only stable two-moon configurations involved short-orbit inner moons, migration from tidal torques negated the possibility of multimillion year resonances. Mutual interactions between the moons did lead to temporary periods of excited tidal heating for an inner moon. While these events were temporary, the excitation lasted, on average, about a million years. In some cases, the tidal heating reached levels above h_{max}. Since the occurrence of these events was inconsistent, their long-term effects on habitability were difficult to evaluate. Besides the inconsistent periods of increased heating, the presence of an outer moon had little effect on the overall tidal evolution of the inner moon.

8.3 Future Work

The work presented in this dissertation is an early attempt at exomoon modeling. As such, many extensions to this study are merited. An option for further consideration is a wider variation of orbital and physical parameters. A disadvantage to my method of directly integrating equations of motion is the potential for long processing times. In order to efficiently utilize limited computational resources, it was necessary to restrict orbital parameters such as inclination and obliquity, setting both values to zero for this study. The effects of non-zero values should be explored. Of specific interest in these parameters is the effects of retrograde satellite motion. Because retrograde satellites are expected to have an extended range of stability, it would be of interest to rerun the rapidly evolving, Io-like orbital simulations using retrograde motion. In addition, it was necessary to limit many physical parameters such as the moments of inertia, tidal dissipation factors (Q), and the tidal Love numbers (k_L). Since these parameters directly influence the tidal and spin evolutions, their various effects should also be explored. Utilizing the process described in this dissertation, these extended investigations could begin, limited only by the availability of computational resources and time.

Another topic for future study involves the simulation of known extrasolar planetary systems around red dwarf stars. A list of potential candidates is provided in Table 3.1. Extended support for specific assumptions regarding the physical properties of these planets may be a challenge since the minimum mass is the only measured physical quantity.

Modifications to the computer code would enable additional topics for future study. For example, my program was designed to consider only two extended bodies. It would be beneficial to repeat the 3-body simulations while treating the star as an additional extended body. The necessary modifications to the code are manageable; however, each additional extended body represents a significant increase in processing time.

One result from this study is the hypothetical existence of extremely tidally heated moons. Peters and Turner (2013) proposed the direct imaging of tidally heated exomoons. Closer examination is warranted to see if my computer model would be useful in providing orbital constraints on directly detectable exomoons. When considering extreme heating in a massive body, the issue of inflation may become important. Inflation is a physical response that was not incorporated into my model. Planetary inflation was considered by Mardling and Lin (2002) and future plans include the integration of this effect into my tidal evolution code.

Finally, a direct benefit of the simulation code is its independence from specific mass

ratios for the orbiting bodies. Therefore, it may be applied to a wide variety of astronomical systems.

BIBLIOGRAPHY

Bibliography

Adams, J. C. (1846, November). Explanation of the observed irregularities in the motion of Uranus, on the hypothesis of disturbance by a more distant planet; with a determination of the mass, orbit, and position of the disturbing body. *MNRAS 7*, 149–152.

Agnor, C. B. and D. P. Hamilton (2006, May). Neptune's capture of its moon Triton in a binary-planet gravitational encounter. *Nature 441*, 192–194.

Armstrong, J. C., R. Barnes, S. Domagal-Goldman, J. Breiner, T. R. Quinn, and V. S. Meadows (2014, April). Effects of Extreme Obliquity Variations on the Habitability of Exoplanets. *Astrobiology 14*, 277–291.

Barnes, J. W. and D. P. O'Brien (2002, August). Stability of Satellites around Close-in Extrasolar Giant Planets. *ApJ 575*, 1087–1093.

Barnes, R., B. Jackson, R. Greenberg, and S. N. Raymond (2009, July). Tidal Limits to Planetary Habitability. *ApJL 700*, L30–L33.

Batalha, N. M., J. F. Rowe, S. T. Bryson, T. Barclay, C. J. Burke, D. A. Caldwell, J. L. Christiansen, F. Mullally, S. E. Thompson, T. M. Brown, A. K. Dupree, D. C. Fabrycky, E. B. Ford, J. J. Fortney, R. L. Gilliland, H. Isaacson, D. W. Latham, G. W. Marcy, S. N. Quinn, D. Ragozzine, A. Shporer, W. J. Borucki, D. R. Ciardi, T. N. Gautier, III, M. R. Haas, J. M. Jenkins, D. G. Koch, J. J. Lissauer, W. Rapin, G. S. Basri, A. P. Boss, L. A. Buchhave, J. A. Carter, D. Charbonneau, J. Christensen-Dalsgaard, B. D. Clarke, W. D. Cochran, B.-O. Demory, J.-M. Desert, E. Devore, L. R. Doyle, G. A. Esquerdo, M. Everett, F. Fressin, J. C. Geary, F. R. Girouard, A. Gould, J. R. Hall, M. J. Holman, A. W. Howard, S. B. Howell, K. A. Ibrahim, K. Kinemuchi, H. Kjeldsen, T. C. Klaus, J. Li, P. W. Lucas, S. Meibom, R. L. Morris, A. Prša, E. Quintana, D. T. Sanderfer, D. Sasselov, S. E. Seader, J. C. Smith, J. H. Steffen, M. Still, M. C. Stumpe, J. C. Tarter, P. Tenenbaum, G. Torres, J. D. Twicken, K. Uddin, J. Van Cleve, L. Walkowicz, and W. F. Welsh (2013, February). Planetary Candidates Observed by Kepler. III. Analysis of the First 16 Months of Data. *ApJ Supplement Series 204*, 24.

Benner, S. A. (2010, December). Defining Life. *Astrobiology 10*, 1021–1030.

Bills, B. G., G. A. Neumann, D. E. Smith, and M. T. Zuber (2005, July). Improved estimate of tidal dissipation within Mars from MOLA observations of the shadow of Phobos. *Journal of Geophysical Research (Planets) 110*, 7004.

Blaney, D. L., T. V. Johnson, D. L. Matson, and G. J. Veeder (1995, January). Volcanic eruptions on Io: Heat flow, resurfacing, and lava composition. *Icarus 113*, 220–225.

Bonfils, X., X. Delfosse, S. Udry, T. Forveille, M. Mayor, C. Perrier, F. Bouchy, M. Gillon, C. Lovis, F. Pepe, D. Queloz, N. C. Santos, D. Ségransan, and J.-L. Bertaux (2013, January). The HARPS search for southern extra-solar planets. XXXI. The M-dwarf sample. *A&A 549*, A109.

Bonfils, X., G. Lo Curto, A. C. M. Correia, J. Laskar, S. Udry, X. Delfosse, T. Forveille, N. Astudillo-Defru, W. Benz, F. Bouchy, M. Gillon, G. Hébrard, C. Lovis, M. Mayor, C. Moutou, D. Naef, V. Neves, F. Pepe, C. Perrier, D. Queloz, N. C. Santos, and D. Ségransan (2013, August). The HARPS search for southern extra-solar planets. XXXIV. A planetary system around the nearby M dwarf GJ 163, with a super-Earth possibly in the habitable zone. *A&A 556*, A110.

Borucki, W., D. Koch, G. Basri, N. Batalha, T. Brown, D. Caldwell, J. Christensen-Dalsgaard, W. Cochran, E. Dunham, T. N. Gautier, J. Geary, R. Gilliland, J. Jenkins, Y. Kondo, D. Latham, J. J. Lissauer, and D. Monet (2008, May). Finding Earth-size planets in the habitable zone: the Kepler Mission. In Y.-S. Sun, S. Ferraz-Mello, and J.-L. Zhou (Eds.), *IAU Symposium*, Volume 249 of *IAU Symposium*, pp. 17–24.

Borucki, W. J., D. G. Koch, G. Basri, N. Batalha, T. M. Brown, S. T. Bryson, D. Caldwell, J. Christensen-Dalsgaard, W. D. Cochran, E. DeVore, E. W. Dunham, T. N. Gautier, III, J. C. Geary, R. Gilliland, A. Gould, S. B. Howell, J. M. Jenkins, D. W. Latham, J. J. Lissauer, G. W. Marcy, J. Rowe, D. Sasselov, A. Boss, D. Charbonneau, D. Ciardi, L. Doyle, A. K. Dupree, E. B. Ford, J. Fortney, M. J. Holman, S. Seager, J. H. Steffen, J. Tarter, W. F. Welsh, C. Allen, L. A. Buchhave, J. L. Christiansen, B. D. Clarke, S. Das, J.-M. Désert, M. Endl, D. Fabrycky, F. Fressin, M. Haas, E. Horch, A. Howard, H. Isaacson, H. Kjeldsen, J. Kolodziejczak, C. Kulesa, J. Li, P. W. Lucas, P. Machalek, D. McCarthy, P. MacQueen, S. Meibom, T. Miquel, A. Prsa, S. N. Quinn, E. V. Quintana, D. Ragozzine, W. Sherry, A. Shporer, P. Tenenbaum, G. Torres, J. D. Twicken, J. Van Cleve, L. Walkowicz, F. C. Witteborn, and M. Still (2011, July). Characteristics of Planetary Candidates Observed by Kepler. II. Analysis of the First Four Months of Data. *ApJ 736*, 19.

Bouquillon, S. and J. Souchay (1999, May). Precise modeling of the precession-nutation of Mars. *A&A 345*, 282–297.

Bouvard, A. (1821). *Tables astronomiques publiees par le Bureau des Longitudes de France.*

Burrows, A., M. Marley, W. B. Hubbard, J. I. Lunine, T. Guillot, D. Saumon, R. Freedman, D. Sudarsky, and C. Sharp (1997, December). A Nongray Theory of Extrasolar Giant Planets and Brown Dwarfs. *ApJ 491*, 856.

Butler, R. P. and G. W. Marcy (1996, June). A Planet Orbiting 47 Ursae Majoris. *ApJL 464*, L153.

Butler, R. P., G. W. Marcy, E. Williams, C. McCarthy, P. Dosanjh, and S. S. Vogt (1996, June). Attaining Doppler Precision of 3 M s-1. *PASP 108*, 500.

Butler, R. P., S. S. Vogt, G. W. Marcy, D. A. Fischer, J. T. Wright, G. W. Henry, G. Laughlin, and J. J. Lissauer (2004, December). A Neptune-Mass Planet Orbiting the Nearby M Dwarf GJ 436. *ApJ 617*, 580–588.

Canup, R. M. and W. R. Ward (2002, December). Formation of the Galilean Satellites: Conditions of Accretion. *ApJ 124*, 3404–3423.

Canup, R. M. and W. R. Ward (2006, June). A common mass scaling for satellite systems of gaseous planets. *Nature 441*, 834–839.

Caspar, M. (1962). *Kepler*. Collier Books BS. Collier Books.

Cassidy, T. A., R. Mendez, P. Arras, R. E. Johnson, and M. F. Skrutskie (2009, October). Massive Satellites of Close-In Gas Giant Exoplanets. *ApJ 704*, 1341–1348.

Chabrier, G. and I. Baraffe (2000). Theory of Low-Mass Stars and Substellar Objects. *ARA&A 38*, 337–377.

Chambers, J. E. and F. Migliorini (1997, July). Mercury - A New Software Package for Orbital Integrations. In *AAS/Division for Planetary Sciences Meeting Abstracts #29*, Volume 29 of *Bulletin of the American Astronomical Society*, pp. 1024.

Charbonneau, D., T. M. Brown, D. W. Latham, and M. Mayor (2000, January). Detection of Planetary Transits Across a Sun-like Star. *ApJL 529*, L45–L48.

Chatterjee, S., E. B. Ford, S. Matsumura, and F. A. Rasio (2008, October). Dynamical Outcomes of Planet-Planet Scattering. *ApJ 686*, 580–602.

Chauvin, G., A.-M. Lagrange, C. Dumas, B. Zuckerman, D. Mouillet, I. Song, J.-L. Beuzit, and P. Lowrance (2004, October). A giant planet candidate near a young brown dwarf. Direct VLT/NACO observations using IR wavefront sensing. *A&A 425*, L29–L32.

Conroy, C. and P. van Dokkum (2012, March). Counting Low-mass Stars in Integrated Light. *ApJ 747*, 69.

Consolmagno, G. J. (1983). Ice-rich moons and the physical properties of ice. *Journal of Physical Chemistry 87*, 4204–4208.

Cumming, A., R. P. Butler, G. W. Marcy, S. S. Vogt, J. T. Wright, and D. A. Fischer (2008, May). The Keck Planet Search: Detectability and the Minimum Mass and Orbital Period Distribution of Extrasolar Planets. *PASP 120*, 531–554.

Delfosse, X., T. Forveille, M. Mayor, C. Perrier, D. Naef, and D. Queloz (1998, October). The closest extrasolar planet. A giant planet around the M4 dwarf GL 876. *A&A 338*, L67–L70.

Dole, S. H. (1964). *Habitable planets for man.*

Domingos, R. C., O. C. Winter, and T. Yokoyama (2006, December). Stable satellites around extrasolar giant planets. *MNRAS 373*, 1227–1234.

Donnison, J. R. (2010, August). The Hill stability of inclined small mass binary systems in three-body systems with special application to triple star systems, extrasolar planetary systems and Binary Kuiper Belt systems. *Planetary & Space Science 58*, 1169–1179.

Doyle, L. R., J. A. Carter, D. C. Fabrycky, R. W. Slawson, S. B. Howell, J. N. Winn, J. A. Orosz, A. Prsa, W. F. Welsh, S. N. Quinn, D. Latham, G. Torres, L. A. Buchhave, G. W. Marcy, J. J. Fortney, A. Shporer, E. B. Ford, J. J. Lissauer, D. Ragozzine, M. Rucker, N. Batalha, J. M. Jenkins, W. J. Borucki, D. Koch, C. K. Middour, J. R. Hall, S. McCauliff, M. N. Fanelli, E. V. Quintana, M. J. Holman, D. A. Caldwell, M. Still, R. P. Stefanik, W. R. Brown, G. A. Esquerdo, S. Tang, G. Furesz, J. C. Geary, P. Berlind, M. L. Calkins, D. R. Short, J. H. Steffen, D. Sasselov, E. W. Dunham, W. D. Cochran, A. Boss, M. R. Haas, D. Buzasi, and D. Fischer (2011, September). Kepler-16: A Transiting Circumbinary Planet. *Science 333*, 1602–.

Dressing, C. D. and D. Charbonneau (2013, April). The Occurrence Rate of Small Planets around Small Stars. *ApJ 767*, 95.

Dressing, C. D., D. S. Spiegel, C. A. Scharf, K. Menou, and S. N. Raymond (2010, October). Habitable Climates: The Influence of Eccentricity. *Apj 721*, 1295–1307.

Dumusque, X., A. S. Bonomo, R. D. Haywood, L. Malavolta, D. Ségransan, L. A. Buchhave, A. Collier Cameron, D. W. Latham, E. Molinari, F. Pepe, S. Udry,

D. Charbonneau, R. Cosentino, C. D. Dressing, P. Figueira, A. F. M. Fiorenzano, S. Gettel, A. Harutyunyan, K. Horne, M. Lopez-Morales, C. Lovis, M. Mayor, G. Micela, F. Motalebi, V. Nascimbeni, D. F. Phillips, G. Piotto, D. Pollacco, D. Queloz, K. Rice, D. Sasselov, A. Sozzetti, A. Szentgyorgyi, and C. Watson (2014, July). The Kepler-10 Planetary System Revisited by HARPS-N: A Hot Rocky World and a Solid Neptune-Mass Planet. *ApJ 789*, 154.

Dumusque, X., F. Pepe, C. Lovis, D. Ségransan, J. Sahlmann, W. Benz, F. Bouchy, M. Mayor, D. Queloz, N. Santos, and S. Udry (2012, November). An Earth-mass planet orbiting α Centauri B. *Nature 491*, 207–211.

Dvorak, R., E. Pilat-Lohinger, E. Bois, R. Schwarz, B. Funk, C. Beichman, W. Danchi, C. Eiroa, M. Fridlund, T. Henning, T. Herbst, L. Kaltenegger, H. Lammer, A. Léger, R. Liseau, J. Lunine, F. Paresce, A. Penny, A. Quirrenbach, H. Röttgering, F. Selsis, J. Schneider, D. Stam, G. Tinetti, and G. J. White (2010, January). Dynamical Habitability of Planetary Systems. *Astrobiology 10*, 33–43.

Efroimsky, M. and V. Lainey (2007, December). Physics of bodily tides in terrestrial planets and the appropriate scales of dynamical evolution. *J. Geophys. Rev. 112*, 12003.

Efroimsky, M. and J. G. Williams (2009, July). Tidal torques: a critical review of some techniques. *Celestial Mechanics and Dynamical Astronomy 104*, 257–289.

Eggleton, P. P., L. G. Kiseleva, and P. Hut (1998, May). The Equilibrium Tide Model for Tidal Friction. *ApJ 499*, 853.

Endl, M., W. D. Cochran, M. Kürster, D. B. Paulson, R. A. Wittenmyer, P. J. MacQueen, and R. G. Tull (2006, September). Exploring the Frequency of Close-in Jovian Planets around M Dwarfs. *ApJ 649*, 436–443.

Fabrycky, D. C., J. J. Lissauer, D. Ragozzine, J. F. Rowe, E. Agol, T. Barclay, N. Batalha, W. Borucki, D. R. Ciardi, E. B. Ford, J. C. Geary, M. J. Holman, J. M. Jenkins, J. Li, R. C. Morehead, A. Shporer, J. C. Smith, J. H. Steffen, and M. Still (2012, February). Architecture of Kepler's Multi-transiting Systems: II. New investigations with twice as many candidates. *ArXiv e-prints*.

Ferraz-Mello, S., A. Rodríguez, and H. Hussmann (2008, May). Tidal friction in close-in satellites and exoplanets: The Darwin theory re-visited. *CeMDA 101*, 171–201.

Fortney, J. J., M. S. Marley, and J. W. Barnes (2007, April). Planetary Radii across Five Orders of Magnitude in Mass and Stellar Insolation: Application to Transits. *ApJ 659*, 1661–1672.

Forveille, T., X. Bonfils, X. Delfosse, R. Alonso, S. Udry, F. Bouchy, M. Gillon, C. Lovis, V. Neves, M. Mayor, F. Pepe, D. Queloz, N. C. Santos, D. Segransan, J. M. Almenara, H. Deeg, and M. Rabus (2011, September). The HARPS search for southern extra-solar planets XXXII. Only 4 planets in the Gl˜581 system. *ArXiv e-prints*.

France, K., C. S. Froning, J. L. Linsky, A. Roberge, J. T. Stocke, F. Tian, R. Bushinsky, J.-M. Désert, P. Mauas, M. Vieytes, and L. M. Walkowicz (2013, February). The Ultraviolet Radiation Environment around M dwarf Exoplanet Host Stars. *ApJ 763*, 149.

Fressin, F., G. Torres, D. Charbonneau, S. T. Bryson, J. Christiansen, C. D. Dressing, J. M. Jenkins, L. M. Walkowicz, and N. M. Batalha (2013, April). The False Positive Rate of Kepler and the Occurrence of Planets. *ApJ 766*, 81.

Galle, J. G. (1846, November). Account of the discovery of Le Verrier's planet Neptune, at Berlin, Sept. 23, 1846. *MNRAS 7*, 153.

Gavrilov, S. V. and V. N. Zharkov (1977, December). Love numbers of the giant planets. *Icarus 32*, 443–449.

Gong, Y.-X., J.-L. Zhou, J.-W. Xie, and X.-M. Wu (2013, May). The Effect of Planet-Planet Scattering on the Survival of Exomoons. *ApJL 769*, L14.

Gonzalez, G. (2005, December). Habitable Zones in the Universe. *Origins of Life and Evolution of the Biosphere 35*, 555–606.

Gorda, S. Y. and M. A. Svechnikov (1999, August). Empirical L-M, R-M, and M-T_{eff} relations for main-sequence stars: Components of close binary systems and low-mass stars. *Astronomy Reports 43*, 521–525.

Haberle, R. M., C. P. McKay, D. Tyler, and R. T. Reynolds (1996). Can Synchronously Rotating Planets Support An Atmosphere? In L. R. Doyle (Ed.), *Circumstellar Habitable Zones*, pp. 29.

Hanel, R., B. Conrath, L. Herath, V. Kunde, and J. Pirraglia (1981, September). Albedo, internal heat, and energy balance of Jupiter - Preliminary results of the Voyager infrared investigation. *Geophys. Res. 86*, 8705–8712.

Hanel, R. A., B. J. Conrath, V. G. Kunde, J. C. Pearl, and J. A. Pirraglia (1983, February). Albedo, internal heat flux, and energy balance of Saturn. *Icarus 53*, 262–285.

Hansen, B. M. S. (2010, November). Calibration of Equilibrium Tide Theory for Extrasolar Planet Systems. *ApJ 723*, 285–299.

Hart, M. H. (1978, January). The evolution of the atmosphere of the earth. *Icarus 33*, 23–39.

Helled, R. (2011, July). Constraining Saturn's Core Properties by a Measurement of Its Moment of Inertia – Implications to the Cassini Solstice Mission. *ApJL 735*, L16.

Helled, R., J. D. Anderson, G. Schubert, and D. J. Stevenson (2011, December). Jupiter's moment of inertia: A possible determination by Juno. *Icarus 216*, 440–448.

Heller, R. (2012, September). Exomoon habitability constrained by energy flux and orbital stability. *A&A Letters 545*, L8.

Heller, R. and R. Barnes (2012, October). Constraints on the habitability of extrasolar moons. *ArXiv e-prints*.

Heller, R. and R. Barnes (2013, January). Exomoon Habitability Constrained by Illumination and Tidal Heating. *Astrobiology 13*, 18–46.

Heller, R., B. Jackson, R. Barnes, R. Greenberg, and D. Homeier (2010, May). Tidal effects on brown dwarfs: application to the eclipsing binary 2MASS J05352184-0546085. The anomalous temperature reversal in the context of tidal heating. *A&A 514*, A22.

Heller, R., J. Leconte, and R. Barnes (2011, April). Tidal obliquity evolution of potentially habitable planets. *A&A 528*, A27.

Heller, R., D. Williams, D. Kipping, and M. A. Peters (2014). Formation, Habitability, and Detection of Extrasolar Moons. *Astrobiology Issue 8 (in press)*.

Heller, R. and J. I. Zuluaga (2013, October). Magnetic Shielding of Exomoons beyond the Circumplanetary Habitable Edge. *ApJL 776*, L33.

Henning, W. G., R. J. O'Connell, and D. D. Sasselov (2009, December). Tidally Heated Terrestrial Exoplanets: Viscoelastic Response Models. *ApJ 707*, 1000–1015.

Henry, G. W., G. W. Marcy, R. P. Butler, and S. S. Vogt (2000, January). A Transiting "51 Peg-like" Planet. *ApJL 529*, L41–L44.

Henry, T. J., W.-C. Jao, J. P. Subasavage, T. D. Beaulieu, P. A. Ianna, E. Costa, and R. A. Méndez (2006, December). The Solar Neighborhood. XVII. Parallax Results from the CTIOPI 0.9 m Program: 20 New Members of the RECONS 10 Parsec Sample. *AJ 132*, 2360–2371.

Herschel, M. (1781). Account of a Comet. By Mr. Herschel, F. R. S.; Communicated by Dr. Watson, Jun. of Bath, F. R. S. *Royal Society of London Philosophical Transactions Series I 71*, 492–501.

Holman, M. J. and P. A. Wiegert (1999, January). Long-Term Stability of Planets in Binary Systems. *AJ 117*, 621–628.

Howard, A. W., G. W. Marcy, J. A. Johnson, D. A. Fischer, J. T. Wright, H. Isaacson, J. A. Valenti, J. Anderson, D. N. C. Lin, and S. Ida (2010, October). The Occurrence and Mass Distribution of Close-in Super-Earths, Neptunes, and Jupiters. *Science 330*, 653.

Huang, S. S. (1959). Occurrence of life outside the solar system. *Am. Sci. 47*, 397.

Hut, P. (1981, June). Tidal evolution in close binary systems. *A&A 99*, 126–140.

Jackson, B., R. Greenberg, and R. Barnes (2008a, July). Tidal Heating of Extrasolar Planets. *ApJ 681*, 1631–1638.

Jackson, B., R. Greenberg, and R. Barnes (2008b, November). Tidal heating of terrestrial extrasolar planets and implications for their habitability. *MNRAS 391*, 237–245.

Jewitt, D. and N. Haghighipour (2007, September). Irregular Satellites of the Planets: Products of Capture in the Early Solar System. *A&A 45*, 261–295.

Johnson, J. A., R. P. Butler, G. W. Marcy, D. A. Fischer, S. S. Vogt, J. T. Wright, and K. M. G. Peek (2007, November). A New Planet around an M Dwarf: Revealing a Correlation between Exoplanets and Stellar Mass. *ApJ 670*, 833–840.

Joshi, M. (2003, June). Climate Model Studies of Synchronously Rotating Planets. *Astrobiology 3*, 415–427.

Joshi, M. M., R. M. Haberle, and R. T. Reynolds (1997, October). Simulations of the Atmospheres of Synchronously Rotating Terrestrial Planets Orbiting M Dwarfs: Conditions for Atmospheric Collapse and the Implications for Habitability. *Icarus 129*, 450–465.

Kaltenegger, L. (2000, September). What does it take for a Moon to Support Life? In B. H. Foing and M. Perry (Eds.), *Exploration and Utilisation of the Moon*, Volume 462 of *ESA Special Publication*, pp. 199.

Kaltenegger, L. (2010, April). Characterizing Habitable Exomoons. *ApJL 712*, L125–L130.

Kaltenegger, L. and D. Sasselov (2011, August). Exploring the Habitable Zone for Kepler Planetary Candidates. *ApJL 736*, L25.

Kane, S. R., J. Horner, and K. von Braun (2012, September). Cyclic Transit Probabilities of Long-period Eccentric Planets due to Periastron Precession. *ApJ 757*, 105.

Kasting, J. F., D. P. Whitmire, and R. T. Reynolds (1993, January). Habitable Zones around Main Sequence Stars. *Icarus 101*, 108–128.

Kidder, L. E. (1995, July). Coalescing binary systems of compact objects to (post)$^{5/2}$-Newtonian order. V. Spin effects. *Phys. Rev. D 52*, 821–847.

Kipping, D. M. (2009a, January). Transit timing effects due to an exomoon. *MNRAS 392*, 181–189.

Kipping, D. M. (2009b, July). Transit timing effects due to an exomoon - II. *MNRAS 396*, 1797–1804.

Kipping, D. M. (2010, November). How to weigh a star using a moon. *MNRAS 409*, L119–L123.

Kipping, D. M., G. Á. Bakos, L. Buchhave, D. Nesvorný, and A. Schmitt (2012, May). The Hunt for Exomoons with Kepler (HEK). I. Description of a New Observational project. *ApJ 750*, 115.

Kipping, D. M., S. J. Fossey, and G. Campanella (2009, November). On the detectability of habitable exomoons with Kepler-class photometry. *MNRAS 400*, 398–405.

Konopliv, A. S., S. W. Asmar, W. M. Folkner, Ö. Karatekin, D. C. Nunes, S. E. Smrekar, C. F. Yoder, and M. T. Zuber (2011, January). Mars high resolution gravity fields from MRO, Mars seasonal gravity, and other dynamical parameters. *Icarus 211*, 401–428.

Kopparapu, R. K. (2013, April). A Revised Estimate of the Occurrence Rate of Terrestrial Planets in the Habitable Zones around Kepler M-dwarfs. *ApJL 767*, L8.

Kopparapu, R. K., R. Ramirez, J. F. Kasting, V. Eymet, T. D. Robinson, S. Mahadevan, R. C. Terrien, S. Domagal-Goldman, V. Meadows, and R. Deshpande (2013a, June). Erratum: "Habitable Zones around Main-sequence Stars: New Estimates". *ApJ 770*, 82.

Kopparapu, R. K., R. Ramirez, J. F. Kasting, V. Eymet, T. D. Robinson, S. Mahadevan, R. C. Terrien, S. Domagal-Goldman, V. Meadows, and R. Deshpande (2013b, March). Habitable Zones around Main-sequence Stars: New Estimates. *ApJ 765*, 131.

Lai, D. (2012, June). Tidal dissipation in planet-hosting stars: damping of spin-orbit misalignment and survival of hot Jupiters. *MNRAS 423*, 486–492.

Lainey, V., J.-E. Arlot, Ö. Karatekin, and T. van Hoolst (2009, June). Strong tidal dissipation in Io and Jupiter from astrometric observations. *Nature 459*, 957–959.

Lainey, V., V. Dehant, and M. Pätzold (2007, April). First numerical ephemerides of the Martian moons. *A&A 465*, 1075–1084.

Laughlin, G., P. Bodenheimer, and F. C. Adams (1997, June). The End of the Main Sequence. *ApJ 482*, 420.

Lewis, K. (2011, February). Effect of realistic and filtered stellar photometric noise on the detection of moons using photometric transit timing. In *European Physical Journal Web of Conferences*, Volume 11 of *European Physical Journal Web of Conferences*, pp. 1009.

Lewis, K. M., P. D. Sackett, and R. A. Mardling (2008, October). Possibility of Detecting Moons of Pulsar Planets through Time-of-Arrival Analysis. *ApJL 685*, L153–L156.

Liebig, C. and J. Wambsganss (2010, September). Detectability of extrasolar moons as gravitational microlenses. *A&A 520*, A68.

Lin, D. N. C., P. Bodenheimer, and D. C. Richardson (1996, April). Orbital migration of the planetary companion of 51 Pegasi to its present location. *Nature 380*, 606–607.

Lissauer, J. J. (2007, May). Planets Formed in Habitable Zones of M Dwarf Stars Probably Are Deficient in Volatiles. *ApJL 660*, L149–L152.

Lissauer, J. J., D. Jontof-Hutter, J. F. Rowe, D. C. Fabrycky, E. D. Lopez, E. Agol, G. W. Marcy, K. M. Deck, D. A. Fischer, J. J. Fortney, S. B. Howell, H. Isaacson, J. M. Jenkins, R. Kolbl, D. Sasselov, D. R. Short, and W. F. Welsh (2013, June). All Six Planets Known to Orbit Kepler-11 Have Low Densities. *ApJ 770*, 131.

Lissauer, J. J., G. W. Marcy, J. F. Rowe, S. T. Bryson, E. Adams, L. A. Buchhave, D. R. Ciardi, W. D. Cochran, D. C. Fabrycky, E. B. Ford, F. Fressin, J. Geary, R. L. Gilliland, M. J. Holman, S. B. Howell, J. M. Jenkins, K. Kinemuchi, D. G. Koch, R. C. Morehead, D. Ragozzine, S. E. Seader, P. G. Tanenbaum, G. Torres, and J. D. Twicken (2012, May). Almost All of Kepler's Multiple-planet Candidates Are Planets. *ApJ 750*, 112.

Lopez, E. D., J. J. Fortney, and N. Miller (2012, December). How Thermal Evolution and Mass-loss Sculpt Populations of Super-Earths and Sub-Neptunes: Application to the Kepler-11 System and Beyond. *ApJ 761*, 59.

Marcy, G. W. and R. P. Butler (1996, June). A Planetary Companion to 70 Virginis. *ApJL 464*, L147.

Marcy, G. W., R. P. Butler, S. S. Vogt, D. Fischer, and J. J. Lissauer (1998, October). A Planetary Companion to a Nearby M4 Dwarf, Gliese 876. *ApJL 505*, L147–L149.

Marcy, G. W., H. Isaacson, A. W. Howard, J. F. Rowe, J. M. Jenkins, S. T. Bryson, D. W. Latham, S. B. Howell, T. N. Gautier, III, N. M. Batalha, L. Rogers, D. Ciardi, D. A. Fischer, R. L. Gilliland, H. Kjeldsen, J. Christensen-Dalsgaard, D. Huber, W. J. Chaplin, S. Basu, L. A. Buchhave, S. N. Quinn, W. J. Borucki, D. G. Koch, R. Hunter, D. A. Caldwell, J. Van Cleve, R. Kolbl, L. M. Weiss, E. Petigura, S. Seager, T. Morton, J. A. Johnson, S. Ballard, C. Burke, W. D. Cochran, M. Endl, P. MacQueen, M. E. Everett, J. J. Lissauer, E. B. Ford, G. Torres, F. Fressin, T. M. Brown, J. H. Steffen, D. Charbonneau, G. S. Basri, D. D. Sasselov, J. Winn, R. Sanchis-Ojeda, J. Christiansen, E. Adams, C. Henze, A. Dupree, D. C. Fabrycky, J. J. Fortney, J. Tarter, M. J. Holman, P. Tenenbaum, A. Shporer, P. W. Lucas, W. F. Welsh, J. A. Orosz, T. R. Bedding, T. L. Campante, G. R. Davies, Y. Elsworth, R. Handberg, S. Hekker, C. Karoff, S. D. Kawaler, M. N. Lund, M. Lundkvist, T. S. Metcalfe, A. Miglio, V. Silva Aguirre, D. Stello, T. R. White, A. Boss, E. Devore, A. Gould, A. Prsa, E. Agol, T. Barclay, J. Coughlin, E. Brugamyer, F. Mullally, E. V. Quintana, M. Still, S. E. Thompson, D. Morrison, J. D. Twicken, J.-M. Désert, J. Carter, J. R. Crepp, G. Hébrard, A. Santerne, C. Moutou, C. Sobeck, D. Hudgins, M. R. Haas, P. Robertson, J. Lillo-Box, and D. Barrado (2014, February). Masses, Radii, and Orbits of Small Kepler Planets: The Transition from Gaseous to Rocky Planets. *ApJS 210*, 20.

Mardling, R. A. and D. N. C. Lin (2002, July). Calculating the Tidal, Spin, and Dynamical Evolution of Extrasolar Planetary Systems. *ApJ 573*, 829–844.

Marois, C., B. Zuckerman, Q. M. Konopacky, B. Macintosh, and T. Barman (2010, December). Images of a fourth planet orbiting HR 8799. *Nature 468*, 1080–1083.

Mayor, M., M. Marmier, C. Lovis, S. Udry, D. Ségransan, F. Pepe, W. Benz, J. . Bertaux, F. Bouchy, X. Dumusque, G. Lo Curto, C. Mordasini, D. Queloz, and N. C. Santos (2011, September). The HARPS search for southern extra-solar planets

XXXIV. Occurrence, mass distribution and orbital properties of super-Earths and Neptune-mass planets. *ArXiv e-prints*.

Mayor, M. and D. Queloz (1995, November). A Jupiter-mass companion to a solar-type star. *Nature 378*, 355–359.

McEwen, A. S., L. P. Keszthelyi, R. Lopes, P. M. Schenk, and J. R. Spencer (2004). *The lithosphere and surface of Io*, pp. 307–328.

Menou, K. and S. Tabachnik (2003, January). Dynamical Habitability of Known Extra-solar Planetary Systems. *ApJ 583*, 473–488.

Messina, S., N. Pizzolato, E. F. Guinan, and M. Rodonò (2003, November). Dependence of coronal X-ray emission on spot-induced brightness variations in cool main sequence stars. *A&A 410*, 671–684.

Meyer, J. and J. Wisdom (2007, June). Tidal heating in Enceladus. *Icarus 188*, 535–539.

Morais, M. H. M. and A. C. M. Correia (2008, December). Stellar wobble caused by a binary system: Can it really be mistaken as an extra-solar planet? *A&A 491*, 899–906.

Morton, T. D. and J. A. Johnson (2011, September). On the Low False Positive Probabilities of Kepler Planet Candidates. *ApJ 738*, 170.

Morton, T. D. and J. J. Swift (2013, March). The Radius Distribution of Small Planets Around Cool Stars. *ArXiv e-prints*.

Murray, C. D. and S. F. Dermott (1999). *Solar system dynamics*.

Namouni, F. (2010, August). The Fate of Moons of Close-in Giant Exoplanets. *ApJL 719*, L145–L147.

Nimmo, F. and U. H. Faul (2013, December). Dissipation at tidal and seismic frequencies in a melt-free, anhydrous Mars. *Journal of Geophysical Research (Planets) 118*, 2558–2569.

Orosz, J. A., W. F. Welsh, J. A. Carter, D. C. Fabrycky, W. D. Cochran, M. Endl, E. B. Ford, N. Haghighipour, P. J. MacQueen, T. Mazeh, R. Sanchis-Ojeda, D. R. Short, G. Torres, E. Agol, L. A. Buchhave, L. R. Doyle, H. Isaacson, J. J. Lissauer, G. W. Marcy, A. Shporer, G. Windmiller, T. Barclay, A. P. Boss, B. D. Clarke, J. Fortney, J. C. Geary, M. J. Holman, D. Huber, J. M. Jenkins, K. Kinemuchi, E. Kruse, D. Ragozzine, D. Sasselov, M. Still, P. Tenenbaum, K. Uddin, J. N. Winn, D. G. Koch, and W. J. Borucki (2012, September). Kepler-47: A Transiting Circumbinary Multiplanet System. *Science 337*, 1511–.

Payne, M. J., K. M. Deck, M. J. Holman, and H. B. Perets (2013, October). Stability of Satellites in Closely Packed Planetary Systems. *ApJL 775*, L44.

Peale, S. J., P. Cassen, and R. T. Reynolds (1979, March). Melting of Io by tidal dissipation. *Science 203*, 892–894.

Pepe, F., C. Lovis, D. Ségransan, W. Benz, F. Bouchy, X. Dumusque, M. Mayor, D. Queloz, N. C. Santos, and S. Udry (2011, October). The HARPS search for Earth-like planets in the habitable zone. I. Very low-mass planets around HD 20794, HD 85512, and HD 192310. *A&A 534*, A58.

Pepe, F. A. and C. Lovis (2008, August). From HARPS to CODEX: exploring the limits of Doppler measurements. *Physica Scripta Volume T 130*(1), 014007.

Perryman, M. (2011, May). *The Exoplanet Handbook*.

Peters, M. A. and E. L. Turner (2013, June). On the Direct Imaging of Tidally Heated Exomoons. *ApJ 769*, 98.

Pierrehumbert, R. T. (2010, December). *Principles of Planetary Climate*.

Pilat-Lohinger, E., P. Robutel, Á. Süli, and F. Freistetter (2008, September). On the stability of Earth-like planets in multi-planet systems. *Celestial Mechanics and Dynamical Astronomy 102*, 83–95.

Pollack, J. B., O. Hubickyj, P. Bodenheimer, J. J. Lissauer, M. Podolak, and Y. Greenzweig (1996, November). Formation of the Giant Planets by Concurrent Accretion of Solids and Gas. *Icarus 124*, 62–85.

Porter, S. B. and W. M. Grundy (2011, July). Post-capture Evolution of Potentially Habitable Exomoons. *ApJ 736*, L14.

Press, W. H., S. A. Teukolsky, W. T. Vetterling, and B. P. Flannery (2002). *Numerical recipes in C++ : the art of scientific computing*.

Rabus, M., R. Alonso, J. A. Belmonte, H. J. Deeg, R. L. Gilliland, J. M. Almenara, T. M. Brown, D. Charbonneau, and G. Mandushev (2009, January). A cool starspot or a second transiting planet in the TrES-1 system? *A&A 494*, 391–397.

Rauch, K. P. and D. P. Hamilton (2002, September). The HNBody Package for Symplectic Integration of Nearly-Keplerian Systems. In *AAS/Division of Dynamical Astronomy Meeting #33*, Volume 34 of *Bulletin of the American Astronomical Society*, pp. 938.

Regenauer-Lieb, K., D. A. Yuen, and J. Branlund (2001, October). The Initiation of Subduction: Criticality by Addition of Water? *Science 294*, 578–581.

Reiners, A., J. L. Bean, K. F. Huber, S. Dreizler, A. Seifahrt, and S. Czesla (2010, February). Detecting Planets Around Very Low Mass Stars with the Radial Velocity Method. *ApJ 710*, 432–443.

Reynolds, R. T., C. P. McKay, and J. F. Kasting (1987). Europa, tidally heated oceans, and habitable zones around giant planets. *Advances in Space Research 7*, 125–132.

Rogers, L. A., P. Bodenheimer, J. J. Lissauer, and S. Seager (2011, September). Formation and Structure of Low-density exo-Neptunes. *ApJ 738*, 59.

Sartoretti, P. and J. Schneider (1999, February). On the detection of satellites of extrasolar planets with the method of transits. *A&A Suppliment 134*, 553–560.

Sasaki, T., G. R. Stewart, and S. Ida (2010, May). Origin of the Different Architectures of the Jovian and Saturnian Satellite Systems. *ApJ 714*, 1052–1064.

Scalo, J., L. Kaltenegger, A. G. Segura, M. Fridlund, I. Ribas, Y. N. Kulikov, J. L. Grenfell, H. Rauer, P. Odert, M. Leitzinger, F. Selsis, M. L. Khodachenko, C. Eiroa, J. Kasting, and H. Lammer (2007, February). M Stars as Targets for Terrestrial Exoplanet Searches And Biosignature Detection. *Astrobiology 7*, 85–166.

Scharf, C. A. (2006, September). The Potential for Tidally Heated Icy and Temperate Moons around Exoplanets. *ApJ 648*, 1196–1205.

Seager, S., M. Kuchner, C. A. Hier-Majumder, and B. Militzer (2007, November). Mass-Radius Relationships for Solid Exoplanets. *ApJ 669*, 1279–1297.

Segura, A., L. M. Walkowicz, V. Meadows, J. Kasting, and S. Hawley (2010, September). The Effect of a Strong Stellar Flare on the Atmospheric Chemistry of an Earth-like Planet Orbiting an M Dwarf. *Astrobiology 10*, 751–771.

Selsis, F., J. F. Kasting, B. Levrard, J. Paillet, I. Ribas, and X. Delfosse (2007, December). Habitable planets around the star Gliese 581? *A&A 476*, 1373–1387.

Spencer, J. R., J. A. Rathbun, L. D. Travis, L. K. Tamppari, L. Barnard, T. Z. Martin, and A. S. McEwen (2000, May). Io's Thermal Emission from the Galileo Photopolarimeter- Radiometer. *Science 288*, 1198–1201.

Szabó, G. M., K. Szatmáry, Z. Divéki, and A. Simon (2006, April). Possibility of a photometric detection of "exomoons". *A&A 450*, 395–398.

Tachinami, C., H. Senshu, and S. Ida (2011, January). Thermal Evolution and Lifetime of Intrinsic Magnetic Fields of Super-Earths in Habitable Zones. *ApJ 726*, 70.

Tarter, J. C., P. R. Backus, R. L. Mancinelli, J. M. Aurnou, D. E. Backman, G. S. Basri, A. P. Boss, A. Clarke, D. Deming, L. R. Doyle, E. D. Feigelson, F. Freund, D. H. Grinspoon, R. M. Haberle, S. A. Hauck, II, M. J. Heath, T. J. Henry, J. L. Hollingsworth, M. M. Joshi, S. Kilston, M. C. Liu, E. Meikle, I. N. Reid, L. J. Rothschild, J. Scalo, A. Segura, C. M. Tang, J. M. Tiedje, M. C. Turnbull, L. M. Walkowicz, A. L. Weber, and R. E. Young (2007, March). A Reappraisal of The Habitability of Planets around M Dwarf Stars. *Astrobiology 7*, 30–65.

Taylor, S. R. (1992). *Solar system evolution: a new perspective. an inquiry into the chemical composition, origin, and evolution of the solar system.*

Tuomi, M., G. Anglada-Escudé, E. Gerlach, H. R. A. Jones, A. Reiners, E. J. Rivera, S. S. Vogt, and R. P. Butler (2013, January). Habitable-zone super-Earth candidate in a six-planet system around the K2.5V star HD 40307. *A&A 549*, A48.

Tuomi, M., H. R. A. Jones, J. R. Barnes, G. Anglada-Escudé, and J. S. Jenkins (2014, March). Bayesian search for low-mass planets around nearby M dwarfs. Estimates for occurrence rate based on global detectability statistics. *ArXiv e-prints*.

Udry, S., X. Bonfils, X. Delfosse, T. Forveille, M. Mayor, C. Perrier, F. Bouchy, C. Lovis, F. Pepe, D. Queloz, and J.-L. Bertaux (2007, July). The HARPS search for southern extra-solar planets. XI. Super-Earths (5 and 8 $M_{\oplus}$) in a 3-planet system. *A&A 469*, L43–L47.

Underwood, D. R., B. W. Jones, and P. N. Sleep (2003, October). The evolution of habitable zones during stellar lifetimes and its implications on the search for extraterrestrial life. *IJAsB 2*, 289–299.

Valencia, D., R. J. O'Connell, and D. Sasselov (2006, April). Internal structure of massive terrestrial planets. *Icarus 181*, 545–554.

Vogt, S. S., R. P. Butler, and N. Haghighipour (2012, August). GJ 581 update: Additional evidence for a Super-Earth in the habitable zone. *AN 333*, 561.

von Bloh, W., C. Bounama, M. Cuntz, and S. Franck (2007, December). The habitability of super-Earths in Gliese 581. *A&A 476*, 1365–1371.

Walker, J. C. G., P. B. Hays, and J. F. Kasting (1981, October). A negative feedback mechanism for the long-term stabilization of the earth's surface temperature. *J. Geophys. Res. 86*, 9776–9782.

Weiss, L. M. and G. W. Marcy (2014, March). The Mass-Radius Relation for 65 Exoplanets Smaller than 4 Earth Radii. *ApJL 783*, L6.

Weiss, L. M., G. W. Marcy, J. F. Rowe, A. W. Howard, H. Isaacson, J. J. Fortney, N. Miller, B.-O. Demory, D. A. Fischer, E. R. Adams, A. K. Dupree, S. B. Howell, R. Kolbl, J. A. Johnson, E. P. Horch, M. E. Everett, D. C. Fabrycky, and S. Seager

(2013, May). The Mass of KOI-94d and a Relation for Planet Radius, Mass, and Incident Flux. *ApJ 768*, 14.

Welsh, W. F., J. A. Orosz, J. A. Carter, and D. C. Fabrycky (2013, August). Recent Kepler Results On Circumbinary Planets. *ArXiv e-prints*.

Williams, D. M. (2013, April). Capture of Terrestrial-Sized Moons by Gas Giant Planets. *Astrobiology 13*, 315–323.

Williams, D. M., J. F. Kasting, and R. A. Wade (1997, January). Habitable moons around extrasolar giant planets. *Nature 385*, 234–236.

Williams, D. M. and D. Pollard (2002, January). Earth-like worlds on eccentric orbits: excursions beyond the habitable zone. *IJAsB 1*, 61–69.

Wolszczan, A. and D. A. Frail (1992, January). A planetary system around the millisecond pulsar PSR1257 + 12. *Nature 355*, 145–147.

Wright, J. T., O. Fakhouri, G. W. Marcy, E. Han, Y. Feng, J. A. Johnson, A. W. Howard, D. A. Fischer, J. A. Valenti, J. Anderson, and N. Piskunov (2011, April). The Exoplanet Orbit Database. *PASP 123*, 412–422.

Yoder, C. F., A. S. Konopliv, D. N. Yuan, E. M. Standish, and W. M. Folkner (2003, April). Fluid Core Size of Mars from Detection of the Solar Tide. *Science 300*, 299–303.

Zahnle, K., N. Arndt, C. Cockell, A. Halliday, E. Nisbet, F. Selsis, and N. H. Sleep (2007, March). Emergence of a Habitable Planet. *Space Science Reviews 129*, 35–78.

Zeng, L. and D. Sasselov (2013, March). A Detailed Model Grid for Solid Planets from 0.1 through 100 Earth Masses. *PASP 125*, 227–239.

Zeng, L. and S. Seager (2008, September). A Computational Tool to Interpret the Bulk Composition of Solid Exoplanets based on Mass and Radius Measurements. *PASP 120*, 983–991.